Microwave Spectroscopy and Transport Measurements of Andreev Bound States in Superconductor – Semiconductor Josephson Junctions

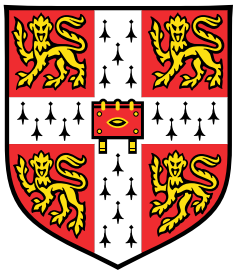

Vivekananth Chidambaram

Department of Physics
University of Cambridge

This thesis is submitted for the degree of
Doctor of Philosophy

Churchill College October 2019

Declaration

This thesis is the result of my own work and includes nothing which is the outcome of work done in collaboration except as declared in the Preface and specified in the text. It is not substantially the same as any that I have submitted, or, is being concurrently submitted for a degree or diploma or other qualification at the University of Cambridge or any other University or similar institution except as declared in the Preface and specified in the text. I further state that no substantial part of my thesis has already been submitted, or, is being concurrently submitted for any such degree, diploma or other qualification at the University of Cambridge or any other University or similar institution except as declared in the Preface and specified in the text. This thesis does not exceed the prescribed limit of 60,000 words.

Contributions to the Experimental Work

The device measured in chapter 4 was fabricated and provided to me by Adam Esmail from the Microelectronics Group. Experimental measurements were performed by myself.

The graphene used in chapter 5 was provided by Jack Alexander-Webber and Abhay Sagade from the Centre for Advanced Photonics and Electronics. The design and fabrication of devices was carried out by myself, with assistance from Jack and Abhay for the graphene etch and ALD dielectric growth. The measurements were carried out by myself.

The InAs 2DEG with epitaxial Al used in chapters 5 and 6 was grown by the Manfra group, Purdue University. Device design, fabrication and measurements were performed by myself at the Center for Quantum Devices, University of Copenhagen.

All of the work was done under the supervision of Malcolm Connolly and Charles Smith.

Vivekananth Chidambaram
October 2019

Microwave Spectroscopy and Transport Measurements of Andreev Bound States in Superconductor – Semiconductor Josephson Junctions

Vivekananth Chidambaram

The physics of superconductor-semiconductor hybrid junctions is governed by a combination of the macroscopic quantum coherence of superconducting systems and the mesoscopic physics inherent to semiconducting devices and Andreev bound states are the microscopic states which mediate transport through these junctions. In this thesis a series of experiments aimed at understanding Andreev bound states in Josephson junction devices are presented.

RF reflectometry measurements of a superconducting tunnel junction are made sensitive near the high tunnel resistance by an impedance transforming tank circuit which can be adapted for different device resistances. The reflectometry measurement corresponds well with DC transport data meaning this technique can measure Josephson junction dynamics at high frequency.

Progress is made towards more transparent superconducting contacts to CVD graphene for graphene Josephson junctions however switching to an epitaxial Al / InAs 2DEG material bypasses the contact transparency issue. Signatures of transport mediated by Andreev bound states in the few mode regime are observed in quantum point contact devices made from this material allowing the possibility of controlling and measuring single Andreev bound states.

Josephson junctions coupled to superconducting resonators are measured using microwave frequency detection and DC transport. Andreev bound states in the few mode regime are observed via their effect on the resonator frequency suggesting that Andreev bound states in this material can be coupled to a resonator allowing measurement and control.

Acknowledgements

There are many people who have helped me or been a part of my life throughout my PhD that I would like to thank here. Firstly are my supervisors Malcolm and Charles who have supported and guided me on the path to ultimately become the researcher that I am now. Malcolm in particular often worked with me at the ground level allowing me to learn directly from him and leading to many useful and interesting discussions. When I first started in the Semiconductor Physics Group I had little research experience save for a short project during my primarily taught Master's and found myself in an experimental PhD project despite many years assuming I would only want to do theory. During this time the more advanced PhD students Carly and Cassandra as well as Joanna later on took the time out of what must have been their own stressful final years to teach me what they knew about every aspect of device physics from design and fabrication to cryogenics and measurement and I thank them along with others from the group who helped me for that.

I worked closely with fellow PhD students Jinggao and Shu-Wei who had related projects meaning we were able to help each other and progress through our PhDs together. I thank them for their help and support along with Gulzat for the diversions and deep reflections on life at coffee time which I think kept us all sociable and sane towards the end of our PhDs. Outside of SP our Mott building lunch group had a strict day-by-day schedule based on years of PhD student experience of where to get the best lunch each day to make the most of the rather limited choice around West Cambridge. This group had many different types of people from different research groups which made for discussions ranging from whimsical to intensely political which was a nice change from the rest of the day spent mostly on physics.

Coming from a group primarily focused on transport, both Malcolm and I were relative strangers to the world of high frequency measurements. Working with Andrew Ferguson and others at the Microelectronics group allowed us to get started far quicker than if we had tried on our own. In particular I would like to thank Adam Esmail and Nick Lambert for their

help in getting my understanding and skills to the level of fabricating and measuring devices using high frequency techniques.

I spent one year at QDev in Copenhagen thanks to the opportunity provided by Charles Marcus. Working in a new lab employing different techniques and approaches to problems provided a refreshing challenge so that despite being far into my PhD I learnt a great deal about experimental research during this time. When starting in the Transmon group I learnt all about qubits and microwave measurements from Karl, Lucas, Natalie and Anders and later worked closely with Albert meaning I wasn't completely lost with these new techniques. I especially enjoyed the interesting and relaxed journal clubs powered by breakfast pastries which I'll definitely encourage wherever I go. I would like to thank Shiv for his help with fabrication enabling me to get my devices working as well as answering my long and multi-part questions which sometimes lead us to the conclusion that some rituals people adhere to in the cleanroom are more superstition than science. I am grateful for my fridge neighbours Fabio and Anasua and fellow perpetual lab inhabitants Antonio and Alexander for the company and conversation during long days and nights measuring. They as well as too many others to list from around the lab all made QDev a welcoming and interesting place to be and ensured that going out for Friday drinks was sure to lead to a memorable evening.

I would also like to thank all my friends from Churchill College, both my old friends from undergraduate and new friends made in the MCR, who made life outside of the lab so enjoyable and continue to be some of my closest friends. Finally I thank my parents who have helped me stay positive and motivated throughout and supported me through everything.

Table of contents

List of figures

Chapter 1

Introduction

1.1 Superconducting Quantum Devices

Superconductors are inherently quantum mechanical at the macro-scale allowing access to quantum coherence effects in larger samples than typically possible in other materials. At the same time advances in device physics mean smaller and more intricate structures can be fabricated with high accuracy and reliability. The meeting of these two building blocks in superconducting devices allows the production of complicated superconducting networks which prove interesting from both fundamental and technological standpoints.

Since the discovery of superconductivity itself, as well as related phenomena such as the Josephson and proximity effects, the unusual properties of superconducting systems and their underlying theoretical explanations attract great interest across the physical sciences. The prospect of unconventional superconductors which could operate at high temperatures or fields drives the search for new superconducting materials while theoretical proposals for new phases of matter hosting exotic quasiparticles such as Majorana bound states call for incorporating superconductors with various materials and device structures.

Superconducting devices with specifically designed functions offer the possibility of on-chip quantum circuits built up of zero-resistance elements. The quantum nature of such circuits also open up new technologies previously impossible with classical circuits. The most prominent of these are qubits (quantum bits) and their application in quantum computing which is discussed below, however other technologies based on superconducting quantum

devices are already in use such as superconducting quantum interference devices (SQUIDs) for magnetic field sensing [1], kinetic inductance detectors (KIDs) for single-photon detection [2] and Josephson parametric amplifiers (JPAs) which amplify signals while adding only the minimum level of noise dictated by quantum mechanics [3, 4].

1.1.1 Quantum Computing with Superconducting Qubits

Quantum computing seeks to use the quantum version of the standard computer 'bit' that all current computers operate with. The basic form of a qubit is a pair of quantum mechanical energy levels with a transition which can be driven and controlled externally. The system has two stationary states and being in either of these states can be identified with the 1 and 0 states of the classical bit, however the similarities only extend this far. While the state of a bit typically corresponds to a voltage being above or below some threshold value, the two-level system of a qubit can take any quantum superposition of the two states meaning the possible states of and operations on a qubit have no classical analogue. The other key aspect of quantum computing is that when multiple qubits are coupled together, their combined state can take forms which cannot be separated into distinct parts for each qubit. In this situation the qubits are entangled and operations on one part of an entangled system of qubits will have an affect on the other parts. The superposition and entanglement properties of qubits can be applied in quantum algorithms to compute solutions to certain difficult problems faster than theoretically possible on a classical computer. Some examples include Shor's algorithm [5] for factorisation which has potential applications in cryptography and Grover's algorithm [6] for searching an unsorted database.

There are many different systems which can function as qubits such as the energy levels of ions trapped in a laser field or the spin states of single impurities in silicon and each type has various advantages and drawbacks. Qubits based on superconducting circuits have two major benefits: (1) They are on-chip devices which makes scaling up fabrication to larger and larger arrays of qubits feasible using the well established techniques for fabricating metal and semiconductor on-chip electronics. (2) Since they are essentially electrical circuits the interface with classical electronics is relatively simple which currently helps for performing experiments and in the future will enable connecting such circuits to each other as well as peripheral quantum and classical devices to make more complex networks.

Superconducting qubits are all based on Josephson junctions however they come in various forms. Two main energy scales governing them are the Josephson energy E_J relating

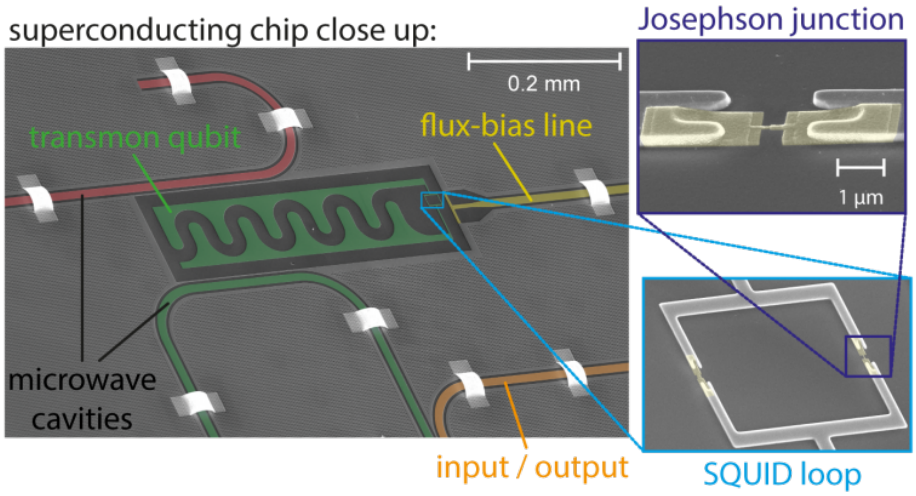

Fig. 1.1 Typical transmon device. From [7]

to Cooper pair tunnelling across junctions and the charging energy E_C required to move charged particles onto a superconducting island isolated by junctions. Different types of superconducting qubits generally differ by what regime of E_J/E_C they operate in and what parameter is used as the control variable. The most well-known superconducting qubit is the transmon (transmission line shunted plasma oscillation) qubit shown in figure 1.1 which is a Josephson junction shunted by a large parallel capacitance and has its origins in one of the early qubit implementations, the Cooper pair box charge qubit [8, 9]. In a Cooper pair box an island is formed between a single Josephson junction and a gate capacitance and if the island's charging energy dominates over thermal effects ($E_C \gg k_B T$) then the energy levels can be described in terms of the number of Cooper pairs on the island leading to parabolic energy bands with respect to offset charge n_g. The Josephson junction allows Cooper pairs to tunnel on and off the island which opens up gaps between the parabola for different island charge numbers, producing bands as shown in figure 1.2(a). The transition energy between the first two bands E_{01} is first-order insensitive to charge noise at half-integer n_g and is sufficiently different to E_{12} (sufficiently anharmonic) that these two levels can be used as a qubit. Increasing the capacitance shunting the Josephson junction decreases E_C thereby increasing the ratio of E_J/E_C. This has two main effects, one is to flatten out the bands in energy meaning that the transition frequencies are stable for a wider range of n_g and not just at certain sweet spots, the other is that the anharmonicity decreases slightly, however a point can be found where the system is still anharmonic enough to operate as a qubit but charge insensitive enough to have an increased qubit lifetime. Typically this is around $E_J/E_C = 50$ as shown in figure 1.2(d) and such a device is in the transmon regime.

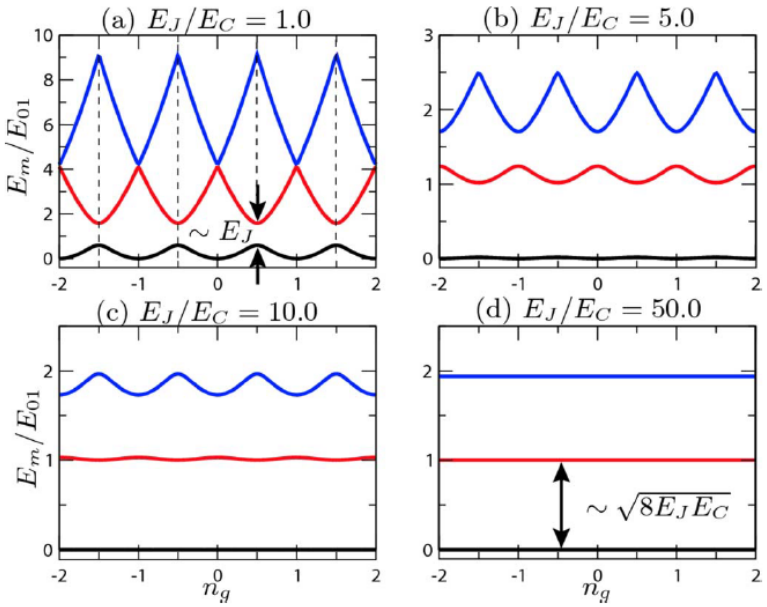

Fig. 1.2 Energy spectrum of a Cooper pair box for different E_J/E_C ratios. The bandwidth and anharmonicity decrease as this ratio is increased and the system crosses over to the transmon regime. From Koch *et al.* [10].

1.2 Superconductor - Semiconductor Hybrid Devices

When a superconductor and semiconductor are brought into contact a proximity effect occurs causing the semiconductor to acquire superconducting phase correlations. Advances in heterostructure growth have lead to semiconductor-superconductor hybrid materials with a highly transparent interface which increases the strength of the proximity effect. Transport modes in standard metal-oxide Josephson junctions have low transmission across the insulating junction and always operate in the tunnelling regime. In contrast strongly proximitised semiconductors can be used to make Josephson junctions containing a large number of highly transmitting modes and so transport across the junction is ballistic.

One advantage of super - semi hybrid junctions is the ability to tune the overall semiconductor carrier density and so conductance and critical current of the junction using a gate voltage. Regions of the semiconductor can also be selectively depleted using split-gates to reduce the number of modes in the conduction channel drastically while preserving their high transmission. This tuneability is useful for producing devices which operate in different regimes of Josephson energy and tuning them during operation.

1.2.1 Andreev Bound States

The proximity effect can be understood in terms of Andreev reflection, a special type of particle reflection possible at super - semi interfaces where an electron (hole) in the semiconductor within the superconducting gap can be reflected as a hole (electron) with a net transfer of charge across the interface and the reflected particle carries phase correlations into the semiconductor (figure 1.3). If there are superconductors on both sides of the semiconductor then particles can repeatedly Andreev reflect from the two interfaces. If the interfaces are close enough together that particles remains phase coherent while traversing the semiconductor they can form bound states consisting of counter-propagating electron- and hole-like quasiparticles. These Andreev bound states (ABS) reside below the superconducting gap in energy and are the microscopic states responsible for current flow across a superconductor - semiconductor junction.

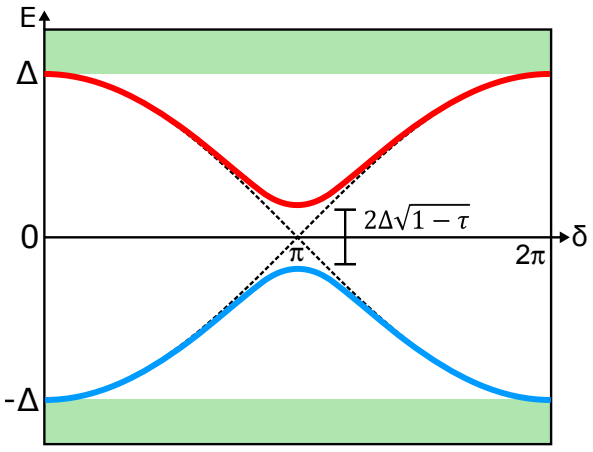

Fig. 1.3 Andreev Bound State Energy

Andreev bound states come in pairs with energies $\pm E_A$ where the Andreev energy E_A is given by:

$$E_A = \Delta\sqrt{1 - \tau \sin^2(\delta/2)} \tag{1.1}$$

with induced superconducting gap Δ, mode transmission τ and phase difference δ across the junction.

This spectrum leads to a non-sinusoidal current-phase relation for ABS which modifies the transport properties of semiconductor Josephson junctions when compared to standard superconducting tunnel junctions. The properties of Andreev bound states are discussed further in section 2.2.2.

1.2.2 Majorana Bound States

Standard Dirac fermions have distinct particles and antiparticles and all free fermions observed so far have this property. Majorana fermions were proposed when considering whether fermions which are their own antiparticle could be consistent with quantum mechanics and special relativity [11]. Although Majorana fermions have not been observed as free particles there is great interest in whether certain quasiparticle excitations in condensed matter systems could exhibit similar properties. Superconductors have an inherent particle-hole symmetry imposing $\hat{\gamma}^{\dagger}(E) = \hat{\gamma}(-E)$ on the creation operator for electron-like quasiparticles at energy E, $\hat{\gamma}^{\dagger}(E)$, and the corresponding annihilation operator (or equivalently the creation operator for hole-like quasiparticles) at energy -E, $\hat{\gamma}(-E)$. At zero energy (or the Fermi energy in materials) this particle-hole symmetry is $\hat{\gamma}^{\dagger} = \hat{\gamma}$, the defining property of Majorana fermions. Therefore it seems superconductivity combined with the existence of a state fixed at zero energy could produce these Majorana quasiparticles which are also known as Majorana zero modes (MZM) or Majorana bound states (MBS) [12, 13, 14].

When confined to two-dimensions, these quasiparticles are predicted to have non-Abelian exchange properties so that when they are moved spatially around each other the final state depends on the specific order of particle exchanges. This braiding of Majorana quasiparticles around each other produces quantum states that are dependent on the history of operations and are spread across disconnected quasiparticles. The non-local nature of these states make them robust to local environmental perturbations and suitable for topological quantum computing - a form of quantum computing where the topological protection from the environment ensures long qubit coherence times and a built-in fault tolerance.

Proposals of how to produce and detect Majorana bound states include magnetic vortex cores of p-wave superconductors such as Sr_2RuO_4 [15, 16], proximitised topological insulators or graphene [17, 18, 19, 20], and proximitised semiconductors with spin-orbit coupling [21, 22]. Although a number of experimental signatures of MBS have been observed in these systems [23, 24, 25, 26] these are not sufficient to rule out other explanations, so the search for definitive proof continues.

1.3 Motivation and Outline

The physical phenomena and technological applications described above motivate studying superconductor - semiconductor hybrid systems in detail. Understanding the underlying Andreev bound state (ABS) physics and developing fabrication and measurement techniques for doing so will assist both in the search for Majorana bound states (MBS) and efforts to incorporate super - semi elements into superconducting quantum circuits.

The physics of Josephson junctions is generally understood by connecting them to electrical leads to obtain their current - voltage characteristics from transport measurements. However, qubit experiments use microwave frequency techniques for measurement and control, so power losses caused by elements such as current leads and semiconducting material must be minimised. Efforts to use ABS and MBS in novel qubit architectures may progress using a combination of these different techniques, such as identifying transport signatures that mark transitions between physical states (e.g. topologically trivial/non-trivial) while measuring the corresponding microwave frequency response.

These points are the main drivers of the work presented in this thesis to better understand superconductor - semiconductor Josephson junction devices, with the specific goal of creating devices which can be measured using both transport and high frequency spectroscopy.

Experiments on Super - Semi Josephson Junctions

The relevant background theory of Andreev bound states in super - semi junctions is described in chapter 2 as well as how they can be coupled to microwave resonators. Device design and fabrication considerations are discussed in chapter 3 followed by an outline of the transport and high frequency measurement techniques and experimental setups used.

The first measurements are shown in chapter 4 on an Al superconducting tunnel junction. Transport and radio-frequency (RF) reflectometry are performed simultaneously by embedding the junction in an RF tank circuit with a bias-T connection for current transport.

In chapter 5, section 5.1 focuses on fabrication and characterisation of superconductor - graphene Josephson junctions and some of the challenges of making a clean super - semi interface are described. A low metal - graphene contact resistance improves the strength

of the superconducting proximity effect so different metal combinations and fabrication methods are tried to improve this.

Section 5.2 introduces a different super - semi material consisting of Al grown epitaxially on an InAs 2DEG (epi-Al/InAs 2DEG), ensuring a clean super - semi interface and a full proximity effect in junctions fabricated using it. Junctions with a split gate are fabricated to form a quantum point contact (QPC). Transport measurements are performed on these 'Andreev QPC' devices in the few mode regime where a few ABS contribute to transport.

In chapter 6 the same epi-Al/InAs 2DEG material and Andreev QPC structure from section 5.2 are placed in a superconducting loop allowing coupling to microwaves via a superconducting resonator. Transport and microwave spectroscopy measurements are performed on the same device and compared. Signatures of the ABS few mode regime are seen in microwave spectroscopy and used to estimate the ABS - resonator coupling.

Finally, I summarise these experiments and provide some concluding remarks in chapter 7.

Chapter 2

Theory

2.1 Two-Dimensional Semiconductors

2.1.1 2DEG Basics

Two dimensional semiconductors are typically produced by growing layers of different semiconductors to produce a stacked heterostructure. The layer structure is designed such that the differing bandgaps form a quantum well where the chemical potential is in the conduction band while being within the bandgap elsewhere. This confines electron wavefunctions in the well which is typically several nanometres thick and leads to quantisation of momentum in the stack direction forming separated bands. The other two spatial directions in the material plane remain unconstrained leaving the electrons with a parabolic free particle energy spectrum in those directions and so such a material is commonly referred to as a 2-dimensional electron gas (2DEG). A different example of a 2DEG is graphene (see section 2.4) which is an inherently two dimensional material with an atypical energy spectrum, however the above is more often the way a 2DEG is achieved.

In a typical 2DEG, electrons behave as free particles with the dispersion relation $E(k) = \frac{\hbar^2 k^2}{2m}$ where m is the effective electron mass and k is the in-plane wavevector. The electrons will fill available energy states up to the Fermi energy E_F. The density of states gives a measure of the number of states that exist in a given energy interval and for a 2DEG is given by

$$D(E) = \frac{m}{\pi\hbar^2} \tag{2.1}$$

which notably does not depend on energy, a result of having a quadratic dispersion relation in a two-dimensional system. The density of states connects the electron density n with the Fermi energy

$$n = \int_0^{E_F} D(E)dE = \frac{m}{\pi\hbar^2}E_F \tag{2.2}$$

This can also be expressed in terms of the Fermi wavevector k_F up to which states in k-space are filled via the dispersion relation $E_F = \frac{\hbar^2 k_F^2}{2m}$ resulting in

$$k_F = \sqrt{2\pi n} \tag{2.3}$$

The Fermi wavevector and related quantities govern the behaviour of charge carriers in the 2DEG and equation 2.3 shows how it varies with the density of those carriers. One of the most useful properties of 2DEGs is that the carrier density can be controlled or the carriers completely depleted using electrostatic gates. A combination of global top/back gates and local gates allows control over the shape and size of the conducting region in semiconductor devices.

2.1.2 Ballistic and Diffusive Transport

Devices can with specific geometries can be made from a 2DEG by a combination of etching and gate definition. In mesoscopic systems transport through devices can be ballistic or diffusive depending on the size of scattering and dephasing length scales relative to the device dimensions.

The main length scale distinguishing different transport regimes is the mean free path l_e. A particle travelling through a 2DEG will experience elastic scattering events due to impurities in the sample on an average timescale τ_e. The average distance between scattering events is the mean free path

$$l_e = v_F \tau_e \tag{2.4}$$

which includes the Fermi velocity $v_F = \frac{\hbar k_F}{m}$. This is because the typically small electric fields in transport experiments slightly shift states in k-space, causing the most change near the Fermi level where there are nearby empty states available and so transport generally involves a Fermi level property, in this case the Fermi velocity. The scattering time is related to the carrier mobility μ by $\tau_e = \frac{\mu m}{e}$ and so the mean free path can be inferred from the carrier mobility μ and carrier density n (see equation 2.3).

If a conducting region has width W and length L along the current direction then two main transport regimes can be distinguished [27]:

$$\begin{array}{rl} \text{Diffusive} & W, L > l_e \\ \text{Ballistic} & W, L < l_e \end{array}$$

In a ballistic system carriers travel from end to end without scattering from impurities and so the transmission probability for modes contributing to transport is close to unity, and any resistance is due to back-scattering at contacts or boundaries where the 2DEG is confined into a channel. Conversely in a diffusive system carriers scatter many times in traversing the device and each scattering event will randomise the direction of travel lowering the overall conductance. In some cases an intermediate regime called quasi-ballistic can be defined as one of: (1) $W < l_e < L$, (2) $L < l_e < W$, (3) $W,\ L \sim l_e$. The first can apply in for example a quantum point contact where the 2DEG is laterally confined into a narrow but long channel.

2.1.3 Quantum Point Contact

Constricting the carriers in a 2DEG in one direction at a quantum point contact (QPC) forms a narrow transport channel. Figure 2.1 shows a split-gate QPC separated from the 2DEG by a dielectric layer which allows carriers below the gates to be depleted. Initially there are carriers everywhere in the 2DEG, but once the gates are energised the regions directly below the gate are first depleted, defining the channel. As the gate voltage is increased[1] the width of the channel is reduced until it is completely pinched off preventing any transport through the channel.

[1] For electrons/holes a more negative/positive gate voltage reduces carrier density. Both situations will be referred to as "increasing" gate voltage for simplicity.

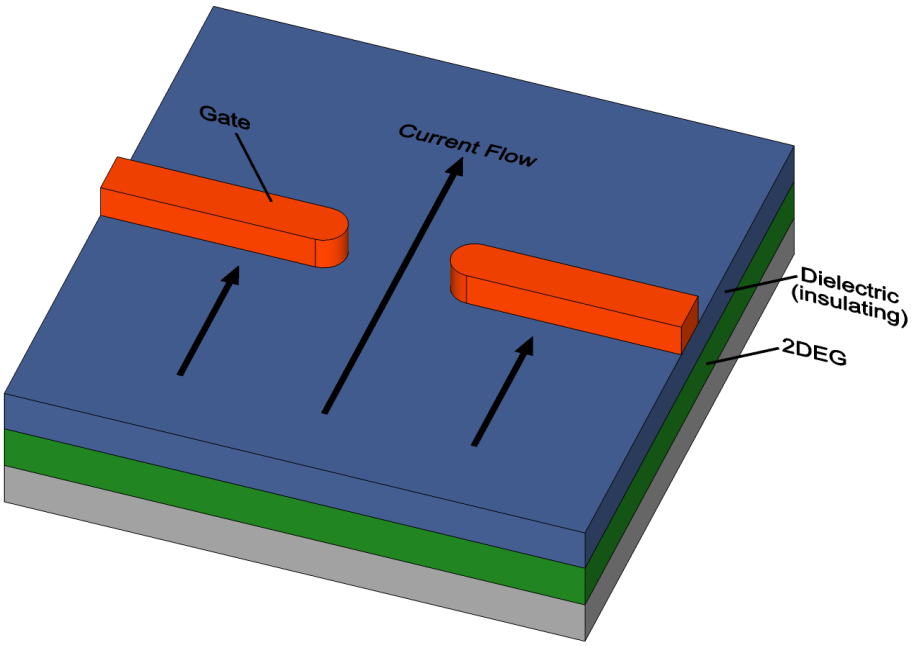

Fig. 2.1 Diagram of a typical quantum point contact. When the split gates are energised to define the QPC, transport in the 2DEG is only possible in the channel between them. When the channel width is comparable to λ_F the conductance becomes quantised signifying 1D transport.

Of interest is the regime between definition and pinch-off where the channel is narrow enough that it is effectively one-dimensional and the conductance through the channel becomes quantised in units of the conductance quantum $G_0 = \frac{2e^2}{h}$. The length scale relevant to this crossover is the Fermi wavelength

$$\lambda_F = \frac{2\pi}{k_F} \tag{2.5}$$

and when the channel width W becomes comparable to this wavelength, electron wavefunctions become quantised in the confinement direction, leaving just one dimension for transport to occur in. The number of transport modes N in the channel is given by the integer number of half Fermi wavelengths which fit in the channel width

$$N = \left\lfloor \frac{2W}{\lambda_F} \right\rfloor \tag{2.6}$$

meaning that in the 1-D regime, the number of modes contributing to transport through the channel can be varied by tuning W which is in turn controlled by the QPC gate voltage. The total conductance through the QPC is the sum of contributions from each mode

$$G = \frac{2e^2}{h} \sum_i \tau_i \tag{2.7}$$

and in the ballistic regime all transmitting modes have $\tau_i = 1$ so this becomes the quantised conductance $G = \frac{2e^2}{h} N$ with conductance steps at integer multiples of the conductance quantum.

2.2 Superconducting Junctions

2.2.1 Superconductivity

Superconducting materials exhibit zero electrical resistance and expulsion of magnetic fields when cooled below a critical temperature T_c. The superconducting state is the result of macroscopic quantum coherence, where a significant fraction of particles in a system occupy the same quantum state. In superconductors electron-electron interactions mediated by lattice phonons are attractive near the Fermi level which favours the formation of Cooper pairs [28] - composite Bosons which can be thought of as pairs of electrons. This opens a gap in the excitation spectrum around the Fermi level proportional to the attractive interaction strength called the superconducting gap Δ.

In the BCS description of superconductivity [29, 30] the ground state of the system is a condensate of Cooper pairs described by the single order parameter $\Delta = |\Delta| e^{i\phi}$. In a uniform superconductor at zero magnetic field this order parameter is the same everywhere, however forming a weak link by interrupting the superconductor with a normal material allows the order parameter's phase to differ either side of the link. In the context of superconductors, "normal" materials are insulators, metals, semiconductors or a constriction of the superconductor forming an atomic point contact and the weak link properties depend on the material used. Also relevant is the strength of the superconducting proximity effect which depends on the dimensions relative to the superconducting coherence length ξ, the distance over which superconducting correlations decay away from the bulk superconductor.

2.2.2 Andreev Bound States

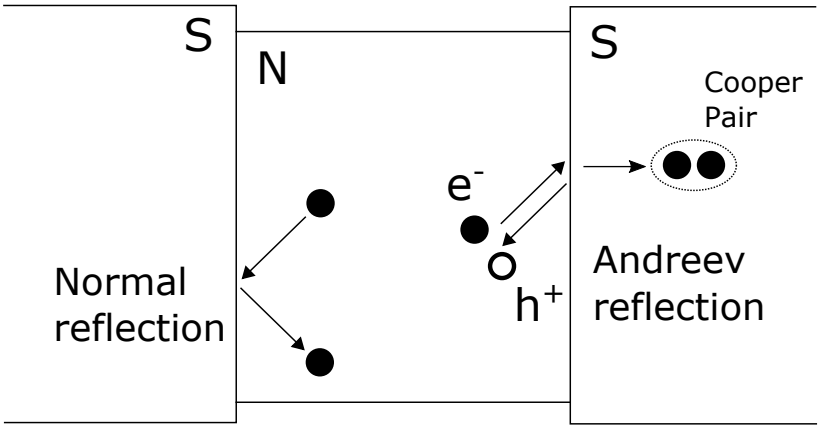

Fig. 2.2 Andreev Reflection on the right in contrast to normal reflection on the left. Andreev reflection results in the transfer of a Cooper pair across the interface and the incident electron reflects back as a hole travelling along a time-reversed path.

The superconducting proximity effect at a superconductor (S) - normal (N) interface is currently understood starting from the idea of Andreev reflection [31] shown in figure 2.2. where an electron in the normal material incident on the interface can reflect back as a hole, or vice versa for an initial hole. This process transfers a charge of $2e$ across the interface, injecting or removing a Cooper pair from the superconductor, and the reflected particle gains an additional phase equal to the superconducting condensate phase ϕ. A Josephson junction is formed of superconductors connected by a section of normal material. The superconductors either side of the junction can have different values of the order parameter phase and this phase difference $\delta = \phi_2 - \phi_1$ drives a dissipationless supercurrent across the junction. Particles in the junction undergo Andreev reflection at both interfaces while remaining phase coherent in between resulting in the formation of Andreev bound states, counter-propagating electron-hole pairs confined to the junction by the superconducting gap either side (figure 2.3). Each conduction mode in the junction produces a pair of ABS corresponding to the two propagation directions with energies $\pm E_A$ where the Andreev energy is

$$E_A = \Delta\sqrt{1 - \tau \sin^2(\delta/2)} \tag{2.8}$$

The mode transmission τ ranges from 0 to 1 where $\tau \approx 0$ is the tunnelling regime and $\tau = 1$ is ballistic transport. The presence of scattering ($\tau < 1$) in the junction means that e.g. left-moving electrons can be scattered into right-moving electrons, coupling the two ABS

and opening a gap at the crossing point $\delta = \pi$ of size $2\Delta\sqrt{1-\tau}$. This coupling makes the ABS spectrum a two-level system with an excitation energy tuned by the phase difference which is a minimum at $\delta = \pi$.

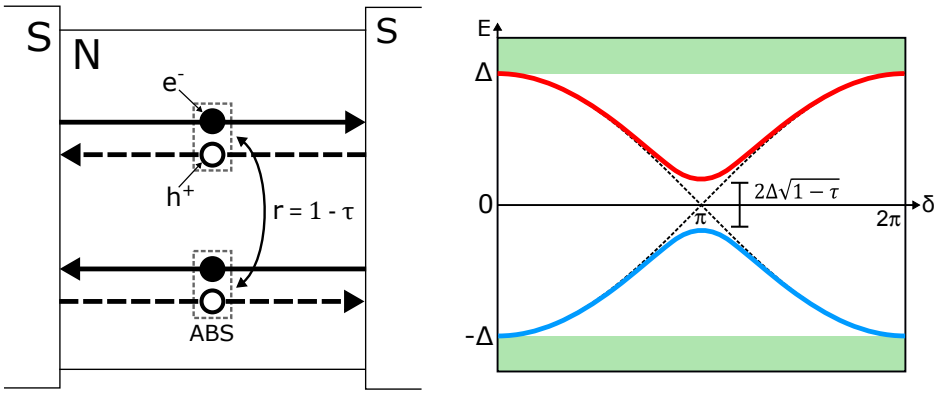

Fig. 2.3 A pair of Andreev bound states in a junction (left) with their corresponding energy spectrum $\pm E_A$ against phase δ (right). The ABS spectrum is separate from continuum states (shaded regions) and exists below the superconducting gap Δ. Dashed lines show the spectrum without scattering (transmission $\tau = 1$) while for $\tau < 1$ scattering in the junction couples the two states together and opens a gap $2\Delta\sqrt{1-\tau}$.

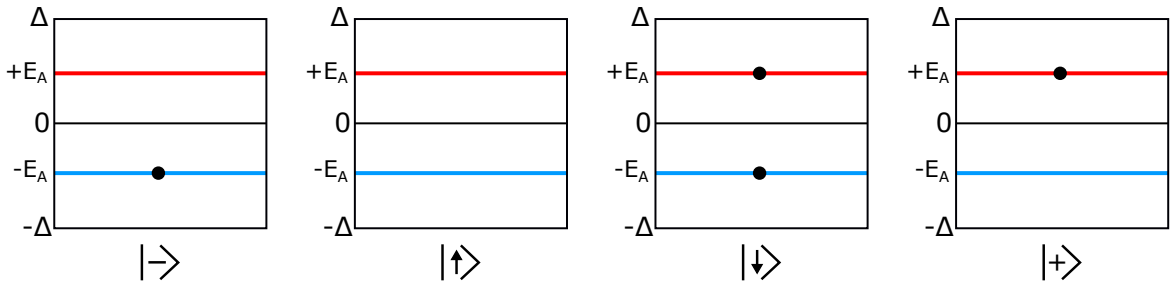

Fig. 2.4 Andreev basis states. States $|-\rangle$ and $|+\rangle$ have even electron parity and total energy $-E_A$ and $+E_A$ respectively. The other states $|\uparrow\rangle, |\downarrow\rangle$ have odd parity and total energy 0.

If the normal section is short compared to the coherence length ξ then the short junction regime applies and continuum states above the gap do not contribute significantly to transport compared to subgap Andreev states [32]. In this situation we can restrict the focus to just the different configurations of the subgap Andreev states shown in figure 2.4. The ground state is $|-\rangle$ with only the lower Andreev state filled and energy $-E_A$ while $|+\rangle$ at energy $+E_A$ is reached by exciting the quasiparticle from the lower to the upper Andreev state and these two states have total even electron parity. The other states $\{|\uparrow\rangle, |\downarrow\rangle\}$ are reached by adding or removing a quasiparticle which changes the parity to odd. The odd states do not contribute to current transport and have no energy difference (both are total energy 0) so are 'dark' in

microwave spectroscopy. It is therefore useful to write the Andreev Hamiltonian for just the even states as a spin-like two level system [33]

$$\hat{H}_A = -E_A \hat{\sigma}_z \tag{2.9}$$

where $\hat{\sigma}_i$ for i = x,y,z are the Pauli matrices. The corresponding current operator is

$$\hat{I}_A = I_A \left[\hat{\sigma}_z + \sqrt{1-\tau} \tan(\delta/2) \hat{\sigma}_x \right] \tag{2.10}$$

This operator is not diagonal in the Andreev basis of energy eigenstates which allows transitions between the even states by coupling to the current (see section 2.3). The diagonal part shows that the even states $\{|+\rangle, |-\rangle\}$ carry currents $I_\pm = \mp I_A$ where

$$I_A = -\frac{2e}{\hbar} \frac{\partial E_A}{\partial \delta} = \frac{e\Delta}{2\hbar} \frac{\tau \sin(\delta)}{\sqrt{1-\tau \sin^2(\delta/2)}}. \tag{2.11}$$

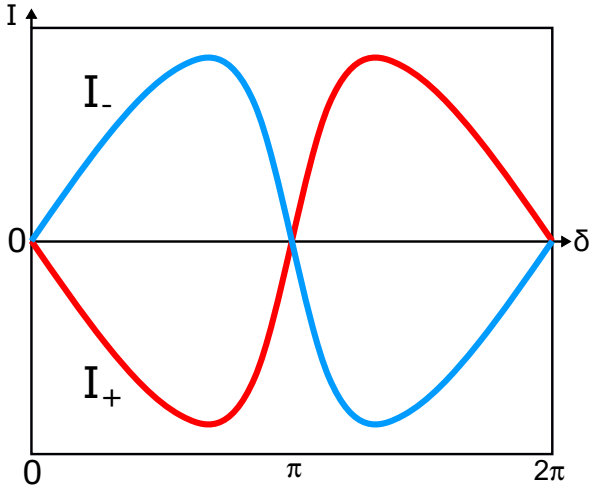

Fig. 2.5 ABS Currents $I_\pm = \mp I_A$ against phase δ corresponding to the two ABS states at $\pm E_A$ in figures 2.3 and 2.4. Each ABS in the pair carries equal and opposite current so a population imbalance is required for a net current to flow. The current-phase relation is non-sinusoidal and the maximum current carried by each ABS is $\frac{e\Delta}{\hbar}$ for $\tau = 1$.

The ABS current is shown in figure 2.5 in which the non-sinusoidal nature of the ABS current-phase relation is clear. Each ABS of a pair carries an equal and opposite current

so a net current can only flow when one of the states is populated and the other empty, for example at zero temperature only the lower ABS will be filled.

2.2.3 SIS Junctions

If the normal section in a junction is an insulator, the dynamics of the current I through the junction and the voltage V across it are governed by the Josephson relations [34]

$$V = \varphi_0 \frac{\mathrm{d}\phi}{\mathrm{d}t} \tag{2.12}$$

$$I = I_c \sin(\phi) \tag{2.13}$$

where the reduced magnetic flux quantum $\varphi_0 = \frac{\hbar}{2e}$.

This sinusoidal current - phase relation is characteristic of tunnelling Josephson junctions and leads to a non-linear inductance with respect to phase. Using $V = L\frac{\mathrm{d}I}{\mathrm{d}t}$ the Josephson inductance L_J is given by:

$$L_J(\phi) = \frac{\varphi_0}{I_c \cos\phi} \tag{2.14}$$

The current-phase relation for SIS junctions can be seen as a special case of the equation (2.11) in the limit of low transmission modes.

2.2.4 Multiple Andreev Reflections

When a finite voltage bias $V \leq 2\Delta/e$ is applied across a junction, it appears that quasiparticles at the gap energy on one side of the junction cannot travel across and no current is expected. However since particles can be Andreev reflected at the interfaces, changing them from electrons/holes to holes/electrons as well as reversing their travel direction, they can traverse the junction multiple times. With each traversal they gain an energy eV and this Andreev reflection process repeats until they have gained a total energy 2Δ which allows them to

escape the junction [35]. This process allows current transfer across the junction at sub-gap voltage bias and predicts sub-gap structure in the I-V curves of superconducting junctions.

A particular multiple Andreev reflection (MAR) process has order n given by the number of junction traversals and all orders with $neV \geq 2\Delta$ can occur. Each order begins to contribute when the bias V crosses through values

$$V = \frac{2\Delta}{en} \tag{2.15}$$

and so peaks in conductance and non-linearities in the I-V characteristic are expected at these values of V for integer n.

Since the n^{th} process requires the particle to traverse the junction n times, its contribution to the current is expected to scale as τ^n meaning that the largest contribution to transport at a voltage V will be from the lowest allowed MAR process with order $n = \lceil 2\Delta/eV \rceil$. Sub-gap structure at low V (for which only high order processes can occur) will therefore not be visible in low transmission systems while ballistic systems will exhibit structure down to very low V.

This qualitative description suffices for a simple understanding of the sub-gap structure seen in Josephson junction devices later but for a more complete description I refer to the first theoretical studies [36, 37, 38] and later full quantum description of the MAR mechanism [39, 40, 41].

2.2.5 Asymmetric SQUID

In chapter 6, a superconducting loop is used to couple a junction to microwaves via a resonator. The loop has one small junction, where the ABS of interest will exist, and another larger junction for control. When the large junction is fully pinched off or fully conducting, the small junction can be measured by transport or microwave spectroscopy respectively with minimal interference from the large junction. However if the large junction is held at an intermediate conductance, its presence must be accounted for and the device must be treated as an asymmetric SQUID - a superconducting quantum interference device consisting of non-identical Josephson junctions. Some measurements are performed in this intermediate situation so a brief overview of asymmetric SQUID physics is given here.

SIS SQUID

SQUIDs are typically made of two Josephson junctions connected to form a complete loop through which an external magnetic flux Φ can be threaded. In many applications a symmetric SQUID where each junction has identical properties is desirable as it provides the largest critical current tuneability, however real devices will generally have some asymmetry and some devices may be asymmetric by design so it is useful to understand the general case. Consider an asymmetric SQUID consisting of two SIS junctions with differing critical currents I_{c1} and I_{c2}. The total current is the sum of the individual currents (2.13) through each junction:

$$I_{SQ,SIS} = I_{c1}\sin\phi_1 + I_{c2}\sin\phi_2 \tag{2.16}$$

Assuming the geometric inductance of each section of the loop is negligible compared to the junction inductances, the phases $\phi_{1,2}$ through each junction are related to the external flux Φ via $\phi_2 - \phi_1 - 2\pi\Phi/\Phi_0 = 2\pi n$ for integer n. This relation allows the total SQUID critical current to be found as [42]:

$$I_{c,SQ,SIS}(\Phi) = \left[I_{c1}^2 + I_{c2}^2 + 2I_{c1}I_{c2}\cos\left(\frac{2\pi\Phi}{\Phi_0}\right)\right]^{\frac{1}{2}} \tag{2.17}$$

The SQUID critical current oscillates between $|I_{c1}+I_{c2}|$ and $|I_{c1}-I_{c2}|$ with external flux so it has an externally tuneable critical current and Josephson inductance. Such relations may also be written using $\phi = 2\pi\Phi/\Phi_0$, the phase difference caused by the external flux.

SNS SQUID

For a SQUID made of normal metal or semiconductor Josephson junctions the current contribution from each junction is modified from equation (2.13) to (2.11) for each transmitting mode. The total current is

$$I_{SQ,SNS} = \frac{e\Delta}{2\hbar}\sum_i \frac{\tau_{1,i}\sin(\phi_1)}{\sqrt{1-\tau_{1,i}\sin^2(\phi_1/2)}} + \frac{e\Delta}{2\hbar}\sum_j \frac{\tau_{2,j}\sin(\phi_2)}{\sqrt{1-\tau_{2,j}\sin^2(\phi_2/2)}} \tag{2.18}$$

where the subscripts 1 and 2 refer to the two junctions as before while the sums over i and j go up to however many transmitting modes contribute to current transport in each junction.

This expression is much more complicated than the SIS SQUID and cannot be simply factored into a phase dependent part and critical current pre-factor as before, so the critical current must be found numerically. This is done by introducing variables for the phase difference $\phi = \phi_2 - \phi_1$, and the average phase $\chi = \frac{\phi_1+\phi_2}{2}$. For each given value of ϕ from 0 to 2π, the current against χ is calculated for $[0, 2\pi]$ and the maximum positive (I_{c+}) and maximum negative (I_{c-}) currents found. Since ϕ is controlled by external flux and is therefore of more interest experimentally, the χ values at which the maxima occur are not shown and the resulting critical currents are plotted against ϕ only.

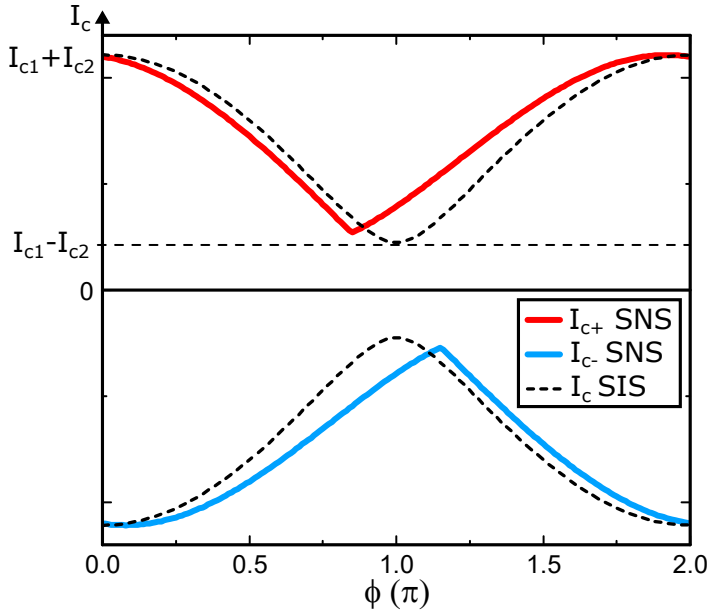

Fig. 2.6 SQUID critical current. Numerically calculated I_c from equation (2.18) against phase ϕ for an SNS SQUID using one mode in each junction. The critical current for an SIS SQUID (equation (2.17)) is also plotted for comparison (dashed lines). The SNS critical currents I_{c+} and I_{c-} are asymmetric about both zero current and $\phi = \pi$ and the minimum value differs from the SIS case.

The critical current for an example SNS SQUID is calculated and plotted in figure 2.6. Comparing to the result for an SIS junction (dashed lines) the strong asymmetry is visible, arising from the non-sinusoidal current-phase relations of the constituent junctions. The phase for minimum critical current is shifted away from $\phi = \pi$ and the minimum value is slightly above $I_{c1} - I_{c2}$. The positive (I_{c+}) and negative (I_{c-}) critical currents are not direct mirror images and are instead related by two reflections about both $I = 0$ and $\phi = \pi$ [33].

2.3 Circuit QED

The coupling of matter and light described by quantum electrodynamics (QED) was initially put into practice in cavity QED, where atoms interact with photonic modes present in a cavity. The anharmonic energy spectrum of atoms means the atom-light system's first energy transition can be addressed separately to others and operated as a qubit. Circuit QED (cQED) applies the same principles to electronic circuits where electromagnetic fields are confined and altered by device geometry and material properties. Superconductors are a natural choice of material to realise the ideal of dissipationless circuits for qubits and other quantum devices.

The Hamiltonian for modelling the devices in chapter 6 can be built up of blocks from each of the main elements: a superconducting transmission line resonator, the Andreev bound state two level system and the coupling between them via the Andreev bound state current. Here I briefly describe how each term comes about.

2.3.1 LC Oscillator

Typically cQED is implemented using 1D transmission lines from which resonators and coupling elements can be formed [43]. An isolated transmission line has a distributed inductance and capacitance which can be treated as many LC circuits coupled together so it is useful to first look at a single LC circuit.

An LC circuit is simply a capacitance C connected to an inductance L forming a complete circuit. The quantum LC oscillator has dynamical variables $\hat{q}$ for the charge on the capacitor and $\hat{\phi}$ the flux in the inductor obeying the commutation relation $[\hat{\phi}, \hat{q}] = i\hbar$. The Hamiltonian is given by

$$\hat{H} = \frac{\hat{q}^2}{2C} + \frac{\hat{\phi}^2}{2L} \tag{2.19}$$

which is recognisable as a harmonic oscillator. It can be solved in the standard way by introducing ladder operators $\hat{a}$ and $\hat{a}^\dagger$ which have $[\hat{a}, \hat{a}^\dagger] = 1$,

$$\begin{aligned}\hat{q} &= -i\sqrt{\frac{\hbar}{2Z}}(\hat{a}-\hat{a}^{\dagger}) \\ \hat{\phi} &= \sqrt{\frac{\hbar Z}{2}}(\hat{a}+\hat{a}^{\dagger})\end{aligned} \tag{2.20}$$

which yields the diagonal Hamiltonian

$$\hat{H}_R = \hbar\omega\left(\hat{a}^{\dagger}\hat{a}+\frac{1}{2}\right) \tag{2.21}$$

where the resonance frequency ω and characteristic impedance Z are given by

$$\omega = \sqrt{\frac{1}{LC}} \tag{2.22}$$

$$Z = \sqrt{\frac{L}{C}} \tag{2.23}$$

Equation (2.21) represents a ladder of energy states each separated by the energy difference $\hbar\omega$. The equal energy difference between all adjacent states is a consequence of the initial Hamiltonian being quadratic in both variables and such a system is called harmonic.

2.3.2 Transmission Line Resonator

Transmission lines are waveguides for electromagnetic waves where the electric and magnetic fields are confined by parallel conductors which have capacitance C' and inductance L' per unit length. Introducing boundaries to a transmission line which further confine waves along the line direction forms a resonator.

Due to their distributed inductance and capacitance, transmission line resonators do not behave like a simple lumped element LC circuit. They can however be modelled classically by treating each small length increment along the line as a lumped element LC network connected to similar networks either side which repeat for the full length of the resonator. Taking the continuum limit and imposing appropriate boundary conditions, depending on how each end is terminated, allows the normal modes of the resonator to be found [44, 45].

Quantisation then gives the quantum Hamiltonian of the transmission line resonator which looks like a sum of LC oscillator Hamiltonians (equation (2.21)) for each mode n:

$$\hat{H}_R = \sum_n \hbar\omega_n \left(\hat{a}_n^\dagger \hat{a}_n + \frac{1}{2}\right) \tag{2.24}$$

A resonator of length L with one end electrically open and the other closed impose opposite boundary conditions on each end and is often called a quarter-wave resonator since in the lowest frequency mode the resonator length is one quarter the wavelength λ. In general $\lambda_n = 4L/(2n+1)$ for integer $n \geq 0$ and the mode frequencies are $\omega_n/2\pi = v/\lambda_n = (2n+1)v/4L$. The phase velocity $v = 1/\sqrt{L'C'}$ depends on the specific geometry and material of the transmission line (see section 3.3.2). If instead both ends have the same boundary condition this forms a half-wave resonator with $\lambda_n = 2L/(n+1)$ and $\omega_n/2\pi = (n+1)v/2L$.

In either case the first harmonic ($n = 1$) frequency is much higher than the fundamental ($n = 0$) so when considering the response of a transmission line resonator to signals near the fundamental frequency, all other modes can be ignored and the resonator treated as a single harmonic oscillator at the fundamental frequency $\omega_R = \omega_0$:

$$\hat{H}_R = \hbar\omega_R \left(\hat{a}^\dagger \hat{a} + \frac{1}{2}\right) \tag{2.25}$$

2.3.3 Andreev Bound State

The Hamiltonian for a single Andreev bound state pair is given by equation (2.9):

$$\hat{H}_A = -\frac{\hbar\omega_A}{2}\hat{\sigma}_z \tag{2.26}$$

where the excitation energy $\hbar\omega_A = 2E_A = 2\Delta\sqrt{1-\tau\sin^2(\delta/2)}$. This is a two level system with energy splitting given by the energy difference between the Andreev bound states in a pair which are controlled by the phase δ and transmission τ.

2.3.4 Coupling Resonators and Andreev Bound States

To achieve readout and control of Andreev bound states they must be coupled to an external system and superconducting resonators which operate at microwave frequencies near the typical minimum ABS frequency $\omega_A(\delta = \pi)$ can be sensitive to ABS dynamics.

A junction containing ABS placed in a superconducting loop allows external flux to be threaded through the loop which applies a phase bias across the junction and so interacts with ABS currents flowing around the loop. If the loop itself is placed near the grounded end of a quarter wave resonator which is a current anti-node then currents flowing in the resonator will thread flux through the loop and so the two interact via a mutual inductance M (see e.g. figure 3.10). The coupling term $\hat{H}_g = M\hat{I}_R\hat{I}_A$ arises from this inductive coupling between the resonator and Andreev currents [46]. The resonator current operator $\hat{I}_R$ is

$$\hat{I}_R = \sqrt{\frac{\hbar\omega_R^2}{2Z_R}}(\hat{a}^\dagger + \hat{a}) \tag{2.27}$$

for resonator frequency ω_R and impedance Z_R [47]. The Andreev current operator $\hat{I}_A$ is given by equation (2.10) and notably does not commute with the Andreev Hamiltonian $\hat{H}_A$ in the presence of scattering ($\tau < 1$) meaning the state of the ABS system can be read out and transitions between states made by coupling to the current. Upon expanding out the current operators $\hat{I}_R$ and $\hat{I}_A$ the coupling terms takes the form

$$\hat{H}_g = g(\hat{a}^\dagger + \hat{a})\left[\frac{1}{\sqrt{1-\tau}\tan(\delta/2)}\hat{\sigma}_z + \hat{\sigma}_x\right] \tag{2.28}$$

$$\text{where } g(\delta,\tau) = \sqrt{z}\frac{E_A(\pi,\tau)}{2}\left[\frac{\Delta}{E_A(\delta,\tau)} - \frac{E_A(\delta,\tau)}{\Delta}\right],\ z = \pi\frac{M^2\omega_R^2}{Z_R R_Q} \tag{2.29}$$

where $R_Q = h/4e^2$.

Putting these elements together gives the ABS - resonator Hamiltonian $\hat{H} = \hat{H}_R + \hat{H}_A + \hat{H}_g$.

2.4 Graphene

Graphene is used in chapter 5 to make progress towards superconductor - graphene junctions in which ABS could be investigated. Graphene is unique among commonly used semiconductors so its basic properties are described here.

Graphene is a 2-dimensional material made of a single layer carbon atoms arranged on a hexagonal lattice shown in figure 2.7 and can be thought of as one sheet of the many which make up graphite. Graphene is a zero band gap semiconductor and the electrical properties resulting from its unique band structure have attracted great interest since it was isolated from graphite by mechanical exfoliation and electrically characterised [48, 49].

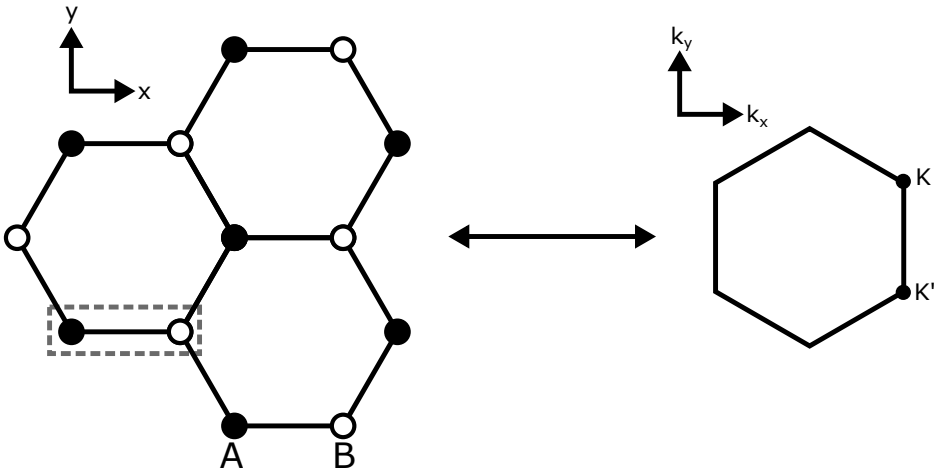

Fig. 2.7 Real space (left) and reciprocal space (right) structure of graphene. The carbon atoms are arranged on a hexagonal lattice with two inequivalent sites A and B, meaning the simplest unit cell is one A-B pair of sites. This structure produces two inequivalent sets of Dirac points K and K' in the first Brillouin zone.

The graphene lattice can be split into two sublattices of alternating lattice points, A and B, which allows the structure to be described by unit cells consisting of adjacent A-B points arranged on a triangular grid. The band structure resulting from this lattice structure has special points in the Brillouin zone where the conduction and valence bands meet called Dirac points (figure 2.8). The A and B sublattice structure produces two inequivalent sets of these points K and K' (also called valleys) and near these Dirac points the dispersion relation of the bands $E_{\pm}(\mathbf{k})$ is approximately linear in momentum $\mathbf{k}$ taking the form $E_{\pm}(\mathbf{k}) = \pm\hbar v_F|\mathbf{k}|$. Charge carriers near Dirac points act like massless free fermions described by the Dirac equation except that they travel at the Fermi velocity of the material v_F, around 300 times less than the speed of light in vacuum c at which free massless particles travel [50, 51].

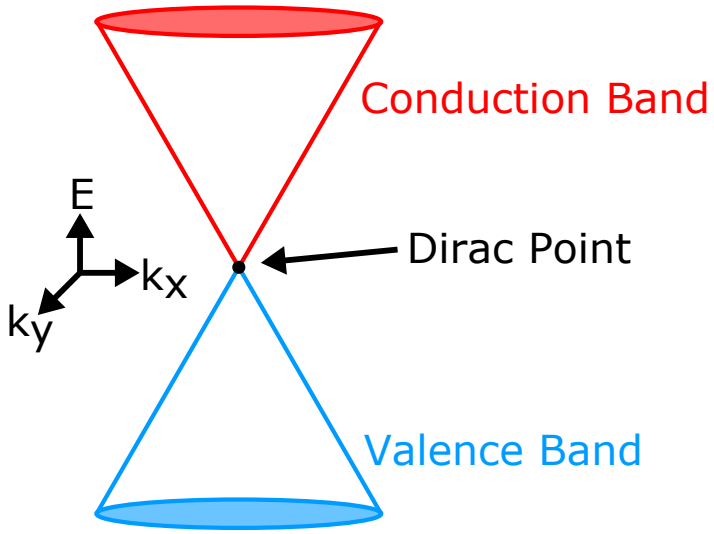

Fig. 2.8 Band structure near a Dirac point. The conduction and valence bands meet at a point and the dispersion is linear. In an undoped sample of graphene the Fermi level is at the Dirac point. Otherwise the charge carriers can be electrons or holes depending on whether the Fermi level is above or below the Dirac point which is therefore also called the charge neutrality point.

Due to the inequivalent A and B sublattices, particle wavefunctions can have differing amplitudes on each sublattice which is described to by a two-component vector. The structure of this sublattice property is similar to spin and so is called pseudospin. In the Dirac Hamiltonian for graphene pseudospin appears in the place of ordinary spin and while the particles do still have ordinary spin, pseudospin effects dominate their dynamics [49]. Denoting the pseudospin by a vector of Pauli matrices $\hat{\boldsymbol{\sigma}} = (\hat{\sigma}_x, \hat{\sigma}_y, \hat{\sigma}_z)$ the Hamiltonian near a Dirac point has the form $\hat{H} = \hbar v_F \hat{\boldsymbol{\sigma}} \cdot \mathbf{k}$ meaning the pseudospin and momentum are locked with their direction being parallel or antiparallel depending on the band and valley. This additional property means the quasiparticles in graphene are massless chiral Dirac fermions.

Chapter 3

Experimental Methods

Experiments on Andreev bound states are performed using devices which are designed to host these states and provide methods of controlling and measuring them. Some of the techniques and practical considerations for the design, fabrication and measurement of these devices are described in this chapter.

3.1 Device Fabrication

There are broadly four types of devices measured in this thesis:

1. Superconducting tunnel junctions, Al/Al oxide - chapter 4.
2. Graphene Josephson junctions, Al/graphene - section 5.1.
3. InAs Josephson junctions with split gate QPC (Andreev QPC), epi-Al/InAs 2DEG material (figure 5.10) - section 5.2.
4. Andreev qubit style devices combining the Andreev QPC with Al or NbTiN resonators and microwave readout circuitry - chapter 6.

The fabrication differs greatly between the different devices so details of fabrication processes and specific fabrication recipes can be found in appendix A. A general overview of fabrication and some of the challenges encountered with each device type is presented here.

Device fabrication starts with a wafer or chip of some starting material and through a series of processing steps results in the desired device. Most of the steps take place in a cleanroom to ensure a controlled environment containing less dust and moisture than the ambient atmosphere. Some processes also require a fixed temperature or vacuum for which other specialised pieces of equipment can be used.

The typical workflow of each fabrication step involves spinning polymer resist on the chip and lithographically defining a pattern which is used for the process which may for example be etching, metallisation or dielectric growth. A large part of optimising fabrication involves iterating over the whole process many times so reducing the time and resources used in each step makes this easier to achieve. Potential optimisations or incompatibilities between certain materials and methods may only become clear when the process as a whole is considered from start to finish.

3.1.1 Superconducting Tunnel Junctions

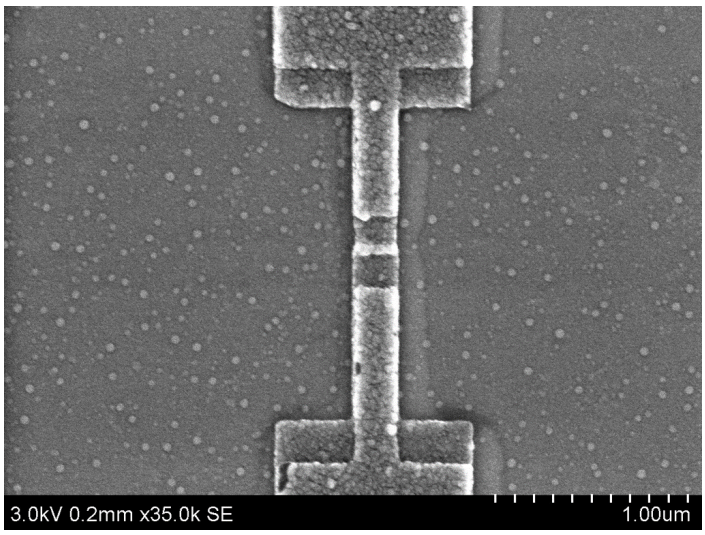

Fig. 3.1 Al tunnel junction device fabricated using a single lithography step by double angle evaporation (see appendix A.2)

The tunnel junction device shown in figure 3.1 and measured in chapter 4 is made of Al evaporated on an undoped Si/SiO_2 substrate making it fairly simple in terms of number of steps. To form the tunnel barrier between the electrodes a double-angle evaporation process is used with a controlled oxidation in between so that the tunnel barrier can be formed and covered by the second electrode while everything is under vacuum giving a controlled barrier

transparency. The double angle process relies on having a large offset between the pattern at each angle which requires forming the pattern in a tall resist stack with a large undercut without collapsing the overhanging resist.

The main challenge with these devices is that once the tunnel barrier is formed the device becomes very sensitive to electrostatic discharge (ESD) where external charge entering the device can destroy the barrier by dielectric breakdown which can also damage the surrounding metal. It became clear that these devices must be transported in and grounded continuously to a metal box to sink any excess charge throughout all following processes and there is still always a risk at the point of connecting to the fridge and cooling down that the device may end up non-conducting anyway. Extensive ESD protection and a decent device yield, to have many chances, seems to be the only solution to this situation. The device which was eventually measured was provided by Adam Esmail who initially showed me this fabrication process and was also fabricating his own related devices.

3.1.2 Graphene Josephson Junctions

Graphene Josephson junctions in chapter 5 (section 5.1) are fabricated on graphene grown by chemical vapour deposition (CVD) and one device containing three junctions is shown in figure 3.2. CVD graphene has the advantage over traditional exfoliated graphene of being grown in large areas. The potential to scale up device fabrication made CVD graphene the choice for the graphene Josephson junction work.

As with any super - semi device the interface quality is of most importance in obtaining a fully proximitised junction showing a supercurrent. This was made difficult by the inherent lower cleanliness of CVD graphene compared to exfoliated and encapsulated varieties as well as our own fabrication processes which require multiple lithography steps, each of which introduces more polymer residue onto the graphene. The compatibility between contact metals and graphene and the role of dielectric encapsulation in the interface quality required some experimentation as well.

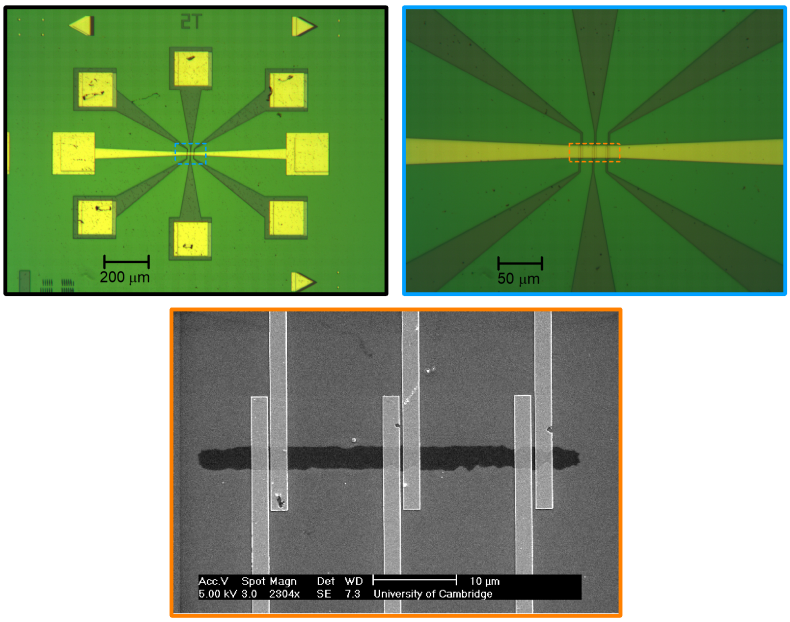

Fig. 3.2 Two-terminal graphene junctions fabricated on CVD graphene. (top) Optical images showing the six contacts for three junctions on the same mesa, plus two more bondpads for the topgate (gold horizontal line). (bottom) SEM of the mesa before top gate deposition so that the mesa (dark region) is visible. The contacts are spaced 300, 400 and 500 nm apart respectively going left to right giving three junctions of varying size on the same mesa. This concept was extended for the TLM style devices (see section 5.1) with junctions going from 200 to 800 nm on the same mesa.

3.1.3 Andreev QPC Devices

The epi-Al / InAs 2DEG devices are split into two main types. Transport devices such as in figure 3.3 are explored in chapter 5 (section 5.2) while purely microwave devices as in figure 3.10 as well as hybrid microwave and transport devices are measured in chapter 6. Fabrication of these benefited from an EBL system which I could book and use myself allowing lithography steps to be completed as soon as possible and modifications to the process to be tested out as well as being very similar to 2DEG gatemon devices for which an established process already existed.

Starting with a clean superconductor - semiconductor interface formed during wafer growth means the junction can be formed by etching material away to form a mesa and then the junction. For the mesa, a negative e-beam resist which becomes more resistant to developer when exposed was used to reduce the write time and this required some testing as it is prone to cross-linking in unwanted areas and is very hard to remove cleanly. The gate dielectric is

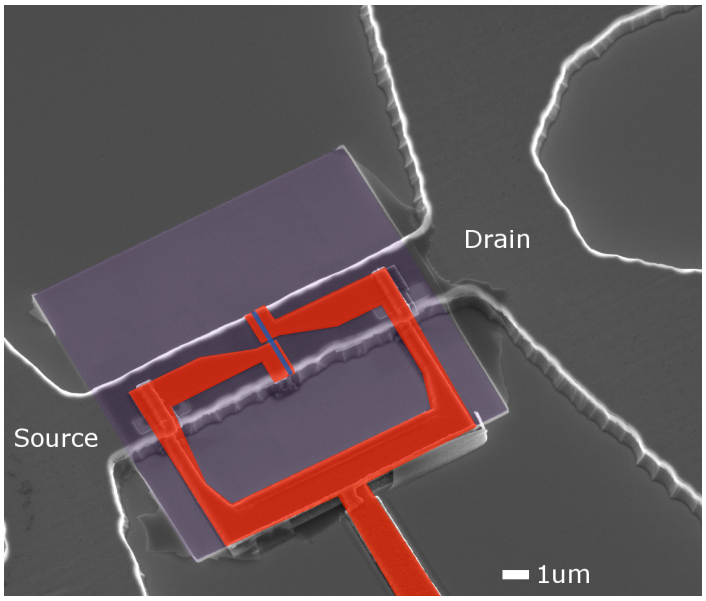

Fig. 3.3 SEM of epi-Al/InAs 2DEG transport device. InAs mesa (raised grey area) is etched down to the InP substrate (lower grey area). The junction (blue) is formed by etching just the epi-Al layer after which the dielectric (purple) and QPC top gate (red) are deposited.

deposited by ALD to separate the junction from the gates. In the transport devices dielectric is grown globally but in the microwave devices it must be lifted off to keep the substrate clear of dielectric for the following microwave circuitry. The 2DEG material has a buffer layer to relieve the strain caused by lattice mismatch between the InAs 2DEG and InP substrate (see figure 5.10). This buffer layer was around 1 µm in the early wafers and around 300 nm later on. Any metal connecting from structures on top of the mesa such as gates to lines on the substrate must climb over this buffer layer height. Since the buffer layer is a series of different material layers without single crystal orientation when it is etched away the edge profile is not a gradual slope and instead forms a concave undercut which is very hard for metal to climb over. Though not a particularly elegant solution, evaporating a large amount of metal at a high angle had the best success at overcoming this issue.

In the microwave devices the microwave circuitry, typically made of Al or NbTiN, is deposited on the InP substrate after the junction and gates are made. The ground plane of the microwave circuit must be well grounded by bonding it to the sample holder ground all around the chip and two parallel bonds are made to each side of the microwave feedline to reduce the bond inductance to minimise signal reflections at the bonds.

3.2 Transport Measurements

Transport measurements focus on determining the I-V characteristics of a device. A lock-in amplifier (LIA) can be used to generate an oscillating (AC) voltage signal at some low frequency (around 10 – 100 Hz) to a device. The signal returning from the device can then be filtered in a narrow range around this frequency since the LIA only measures the component at the original frequency which cuts out some of the noise present at DC and other frequencies. Combining a small AC excitation from the LIA with a larger DC offset allows the LIA measurement to map out either the differential conductance dI/dV against V or differential resistance dV/dI against I depending on the circuit used. These alternative measurements are derivatives of the I-V curve but can be easier to perform in certain device transport regimes and can make notable features more visible and easier and interpret.

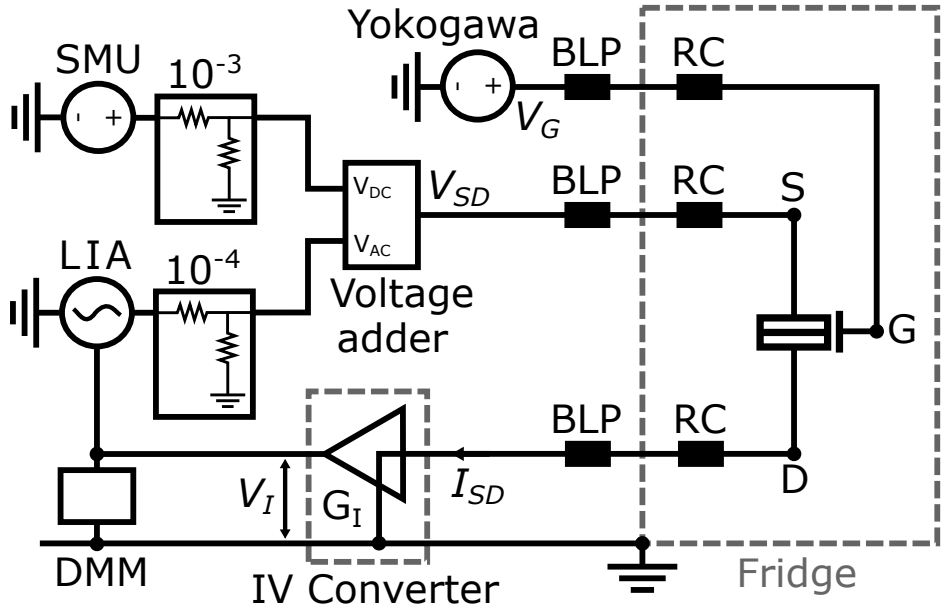

Fig. 3.4 Setup for constant voltage measurement on a 2-terminal device to measure differential conductance dI/dV. The LIA applies an AC voltage V_{AC} which is added to a DC offset V_{DC} applied by the SMU and the combined voltge V_{SD} applied across the device. The resulting current I_{SD} is amplified by the IV converter giving a voltage V_I which is measured by the LIA to find the AC current I_{AC} and by the DMM to find the DC current I_{DC}. $dI/dV = I_{AC}/V_{AC}$ is measured against DC voltage bias V_{DC} and gate voltage V_G. BLP-1.9+ low-pass filters are used on lines outside the fridge and RC filters on lines inside the fridge. This setup is most useful in the tunnelling regime for determining the superconducting gap.

Figure 3.4 shows a constant voltage measurement on a 2-terminal device. The LIA outputs an AC voltage which is reduced by a voltage divider (10^{-4}) giving the excitation V_{AC}. A DC offset voltage V_{DC} is applied by the source-measure unit (SMU) via another voltage divider

(10^{-3}). These voltages are combined and the total voltage bias V_{SD} is applied across the source (S) and drain (D) of the device. The resulting current I_{SD} is amplified by a Basel IV converter, typically with gain $G_I = 10^8$ or 10^9 V/A, giving a voltage $V_I = I_{SD} \times G_I$. The AC and DC components of this voltage are measured by the LIA and a digital multimeter (DMM) respectively from which the corresponding currents I_{AC} and I_{DC} can be calculated. A gate voltage V_G is applied to top gate (G) by a Yokogawa voltage source. Each line has BLP-1.9+ low-pass filters outside and RC filters inside the fridge to reduce high frequency noise.

The differential conductance is given by $dI/dV = I_{AC}/V_{AC}$ and is measured as a function of the DC voltage bias V_{DC} and gate voltage V_G. This setup is best used for 2-terminal devices in the tunnelling regime which have a very high resistance and so the applied voltage drop is almost entirely across the device. With a 4-terminal device the voltage across the device could be monitored to ensure it is the same as the voltage applied and to account for any deviations when calculating the conductance.

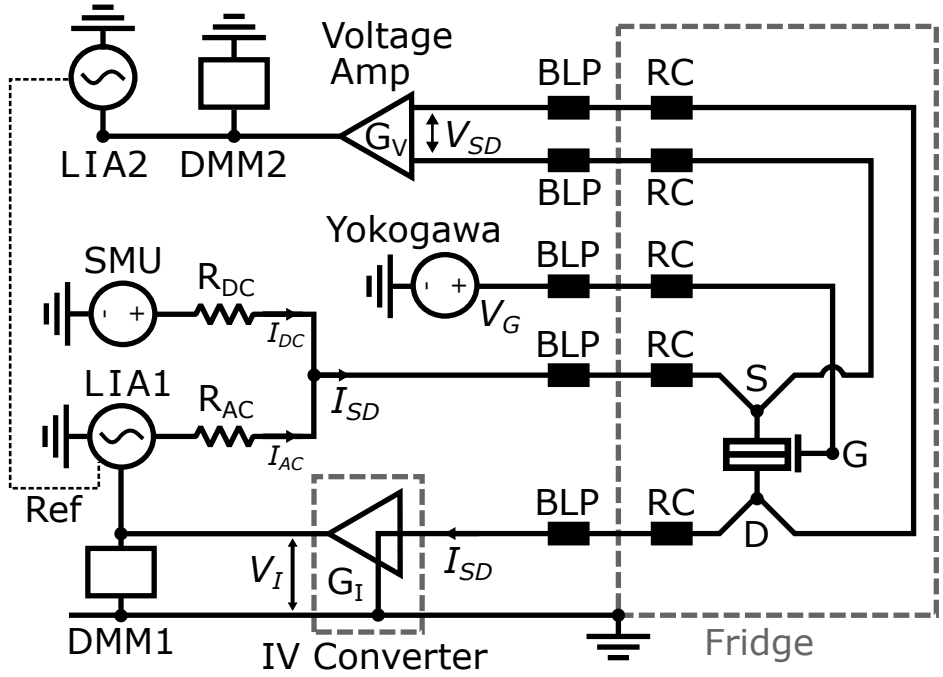

Fig. 3.5 Setup for constant current measurement on a 4-terminal device to measure differential resistance dV/dI. LIA1 and SMU, combined with resistors R_{AC} and R_{DC}, apply AC and DC currents I_{AC} and I_{DC} respectively through the device. A similar current measurement circuit to figure 3.4 is used to read back the current and ensure it stays constant. The voltage drop across the device V_{SD} has AC and DC parts V_{AC} and V_{DC} which are amplified and measured by LIA2 and DMM2 respectively. Reference 'Ref' ensures LIA2 is frequency and phase locked to LIA1. $dV/dI = V_{AC}/I_{AC}$ is measured against DC current bias I_{DC} and gate voltage V_G. This setup is most useful in the open transport regime for critical current measurements.

A constant current measurement is required for critical current measurements and figure 3.5 shows a setup for achieving this with a 4-terminal device. The AC and DC voltage biases from the LIA1 and SMU are converted to currents I_{AC} and I_{DC} by large resistors $R_{AC} = 500$ MΩ and $R_{DC} = 5$ MΩ. The combined current I_{SD} is applied through the source (S) - drain (D) path. The return current is monitored by LIA1 and DMM1 using the same circuit as in figure 3.4 to check that it stays constant. The voltage drop across the device V_{SD} is amplified (gain $G_V = 10^3$) and the AC and DC components measured by LIA2 and DMM2 respectively. From this the AC and DC voltage drop across the device V_{AC} and V_{DC} can be found. A reference signal from LIA1 to LIA2 ensures that LIA2 locks in to signals of the same frequency and phase as the excitation from LIA1. A gate voltage V_G is applied to the top gate (G) by the Yokogawa voltage source. As before, BLP-1.9+ low-pass filters and RC are used to reduce high frequency noise.

The differential resistance is given by $dV/dI = V_{AC}/I_{AC}$ and can be measured as a function of the DC current bias I_{DC} and gate voltage V_G. This setup works best for junctions which are highly conducting so that the applied voltage drops mostly across the large resistors meaning a constant current is supplied to the device.

3.3 High-Frequency Measurements

3.3.1 RF Reflectometry

A reflectometry measurement involves sending a high frequency signal to the device along a transmission line typically of impedance Z_0 (typically 50 Ω) connected to a load of impedance Z and measuring the reflected signal at the same terminal. The reflected signal can be demodulated at the same frequency as the initial signal to obtain the in-phase (I) and quadrature (Q) components of the signal, or equivalently converted to amplitude (A) and phase (θ). These two bases are related by $A = \sqrt{I^2+Q^2}$ and $\theta = \tan^{-1}(Q/I)$. If the initial signal is A_i and the reflected signal A_r then the amplitude reflection coefficient is their ratio $\Gamma = \frac{A_r}{A_i}$ so measuring the reflected signal amplitude and phase relative to the initial signal sent to the device gives the amplitude and phase of the reflection coefficient.

The reflection coefficient is related to the impedance mismatch between the load and transmission line

$$\Gamma = \frac{Z - Z_0}{Z + Z_0} \tag{3.1}$$

and so Γ is most sensitive to changes in the load impedance when it is close to Z_0. If the load is just a device of resistance R then $Z = R$ and so $\Gamma = (R - Z_0)/(R + Z_0)$. A typical tunnel junction will have R $\gg$ 10 kΩ which is much higher than Z_0 so reflectometry performed directly on a tunnel junction will be very insensitive. To overcome this a tank circuit can be used to transform the device impedance closer to Z_0 as shown in figure 3.6(a). If the Josephson junction device is treated simply as a capacitor C_d in parallel with a variable resistance R then inserting an inductor before the device forms a resonant tank circuit from the inductance L and the total capacitance $C = C_p + C_d$ where C_p is the parasitic capacitance between bond pads and tracks on the mounting PCB and a ground plane covering the back surface of the PCB. This circuit has resonance frequency $\omega_r \approx \frac{1}{\sqrt{LC}}$. The device acts as an additional impedance load on the LC resonator which will shift the resonance frequency and alter the reflected signal power around resonance. The total impedance of this circuit is given by

$$Z = i\omega L + \frac{1}{i\omega C + R^{-1}} \approx \frac{L}{RC} + i\left(\omega L - \frac{1}{\omega C}\right) \tag{3.2}$$

where the approximations made are that $\omega RC \gg 1$ which will hold for device resistances $R \gg 1$ kΩ in our system, and that the frequency is near resonance $\omega \approx \omega_r$. The approximate form of Z corresponds to the linear circuit 3.6(b) where the device is replaced by the term $Z_t = L/RC$. At resonance the LC part of the circuit becomes transparent and the reflection coefficient is given by:

$$\Gamma = \frac{\frac{L}{RC} - Z_0}{\frac{L}{RC} + Z_0}. \tag{3.3}$$

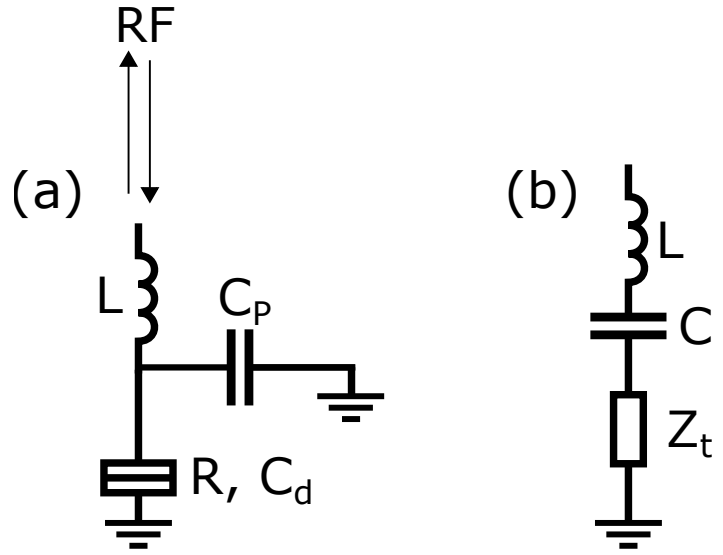

Fig. 3.6 Reflectometry Circuit. (a) Lumped element circuit used to describe the system in terms of device resistance (R) and capacitance (C_d), tank circuit inductor (L) and parallel parasitic capacitance (C_p). (b) Effective series circuit for (a) near resonance where the transformed impedance $Z_t = L/RC$ determines the reflected RF power.

The tank circuit acts as an impedance transformer since the device resistance R is replaced by the transformed impedance term $Z_t = L/RC$. Z_t will generally be closer to the line impedance Z_0 and so Γ will have a higher sensitivity to changes in R. The maximum sensitivity occurs near at resistances near where Γ goes to zero which occurs at the matching impedance $Z_t = Z_0$ at a device resistance $R_m = L/CZ_0$. The matching device resistance and the resonance frequency can be altered by changing the inductance L depending on the frequency range of interest and the expected range of device resistances.

The above treatment assumed the device can be described by a fixed capacitance and a variable resistance but in reality devices will have varying capacitance and inductance which will alter the total impedance and so the reflectometry signal will be sensitive to reactive

changes in device impedance too. Reflectometry can be used in this way to perform sensitive high frequency measurements of device impedance.

Reflectometry Measurement Setup

The measurement setup in the dilution refrigerator used for the experiments in chapter 4 is shown in figure 3.7 with the main temperature stages marked. At base temperature the sample is nominally at 50 mK. The device is mounted on a sample holder containing the tank circuit and a bias-T for separating the RF reflectometry setup from a separate DC circuit for applying a voltage bias and measuring back the current using a low frequency lock-in amplifier (LIA). RC low pass filters on the DC lines were made by previous fridge users using lumped elements on PCB. They add 2 kΩ to each line and have a cutoff at 1 KHz to reduce noise in the DC measurement.

A high frequency lock-in amplifier (UHFLI) is used to send the initial RF signal to the tank circuit and device. A variable attenuator is set at -40 dB such that, combined with other attenuators inside the fridge, the signal strength at the device stays low (generally around -120 dBm). The reflected signal from the same port is sent back using a directional coupler through low temperature (Quinstar QCA-U350-30H) and room temperature (MITEQ AU-1667) amplifiers to boost the signal strength which returns to the UHFLI to be demodulated and the resulting amplitude and phase recorded.

In figure 3.8 the reflectometry signal amplitude and phase are shown as a function of frequency. The resonance is visible as a dip in amplitude and a non-linear phase shift at $f_r =$ 328 MHz. The tank circuit is constructed using a lumped element inductor L = 620 nH and the parasitic capacitance to ground which can be estimated using the measured resonance frequency as $C_p \approx 0.38$ pF. The inductor is chosen such that the resonance frequency sits within the low temperature amplifier operating range of 300 - 400 MHz.

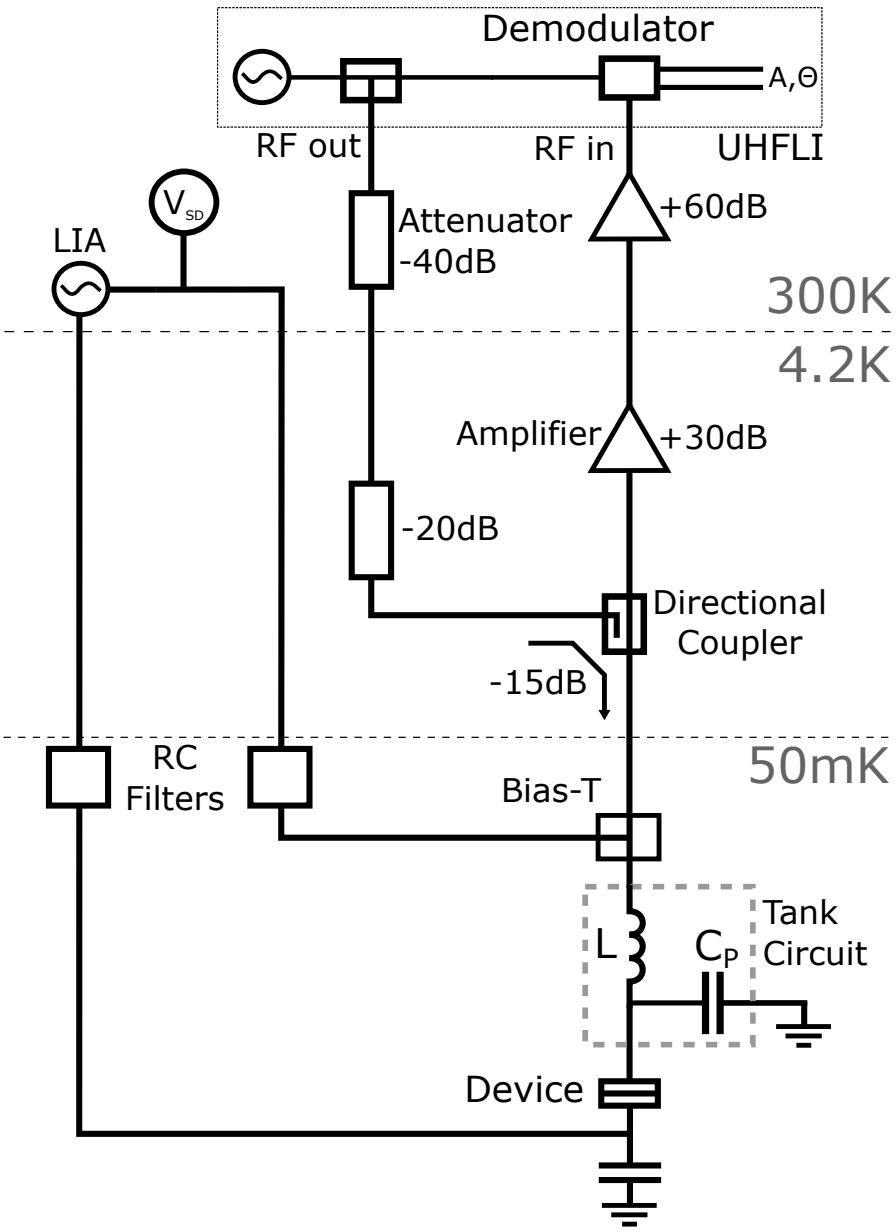

Fig. 3.7 Measurement setup in a Kelvinox 400 Dilution Refrigerator. The RF tank circuit attached to the device allows reflectometry to be performed via the directional coupler, using a high frequency lock-in amplifier (Zurich Instruments UHFLI) to generate the incident signal and demodulate the reflected signal. Attenuators ensure RF power at the device stays low while amplifiers are used to increase the signal strength for demodulation. The bias-T allows a DC bias V_{SD} to be applied and two-terminal resistance measurements to be performed using the low frequency lock-in amplifier (LIA). RC filters on the DC lines have a 1 kHz cutoff and add around 2 kΩ to each line.

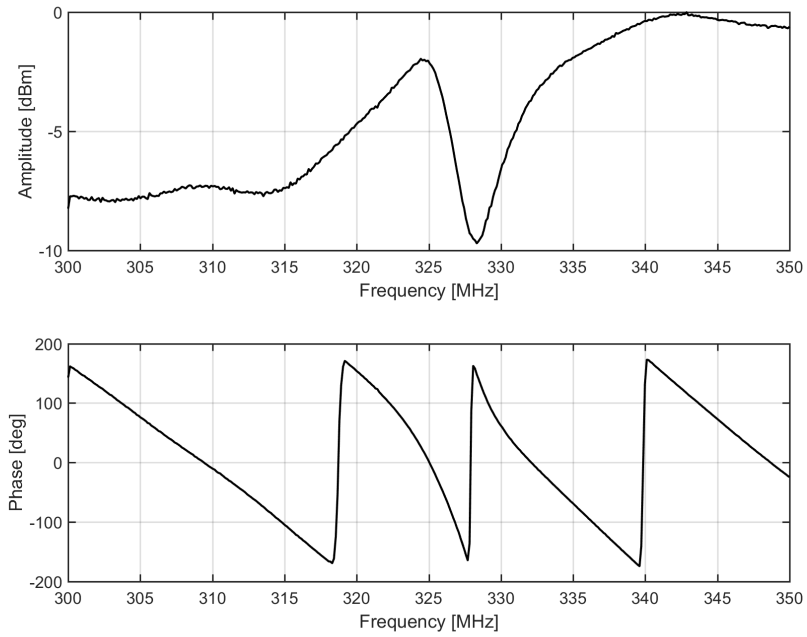

Fig. 3.8 Tank circuit resonance. The reflected power from the tank circuit and device is measured while sweeping the signal frequency. (top) Relative amplitude of the reflectometry signal against frequency showing the resonance dip at 328 MHz. (bottom) Phase of the reflected signal against frequency showing the resonance as a non-linear phase shift at the same frequency of 328 MHz. Subsequent measurements are made by reading the amplitude and phase with the frequency set to 328 MHz.

3.3.2 Microwave Spectroscopy

Microwave measurements are performed by coupling Josephson junctions to superconducting quarter wave transmission line resonators. The junction acts as an additional impedance load at the end of the the resonator which shifts its resonance frequency and alters power transmission through it. This load varies with junction properties and so measuring the resonator power response with frequency gives a measure of dynamics within the junction.

Multiple resonators are coupled capacitively to a common feedline by placing the open end of the resonators near the feedline. In this configuration any power entering a resonator reduces the transmitted power along the feedline allowing the resonator response to be found by measuring transmission through the feedline. A particular resonator will only have a significant effect on transmission when the signal along the feedline has a frequency f close to its resonant frequency f_r and so a single feedline can be used to measure many resonators as long as they are designed to have widely spaced resonance frequencies.

The response of a resonator can be characterised by quality factors Q corresponding to different power loss mechanisms which are generally defined as

$$Q = 2\pi f_r \frac{\text{Energy stored in resonator}}{\text{Rate of Energy loss from resonator}} \tag{3.4}$$

A high Q means a lower loss resonator and a large part of resonator optimisation focuses on increasing Q-factors. Losses intrinsic to the resonator such as into the dielectric substrate or any resistive elements are given by the internal Q-factor, Q_i. Power leaving via the coupling to the feedline is also a 'loss' from the resonator perspective and is given by the external Q-factor, Q_e. The system as a whole is characterised by the total Q-factor Q_T which is related to the others by $Q_T^{-1} = Q_i^{-1} + Q_e^{-1}$. The amplitude transmission S21 through a feedline coupled capacitively to a quarter-wave resonator at frequency f is given by [52]:

$$S21 = 1 - \frac{Q_T/Q_e}{1 + 2iQ_T\frac{f-f_r}{f_r}} \tag{3.5}$$

The response is completely characterised by the three parameters f_r, Q_i and Q_e (or Q_T). The power ratio through the feedline is given by $|S21|^2$ which has a characteristic Lorentzian shape around f_r which appears as a dip in power for a resonator coupled to a feedline. Often the magnitude $|S21|$ and phase $\arg(S21)$ of the signal are measured as shown in figure 3.12.

Transmission lines can be implemented using a variety of geometries. The microwave circuitry and resonators in our devices use a coplanar waveguide (CPW) geometry which is commonly used for cQED devices due to three main features: (1) It is planar meaning circuitry can be fabricated on the chip surface similarly to the rest of a typical device. (2) Fields are mostly confined in the gap between the central conductor and ground plane which reduces crosstalk with nearby structures. (3) A central conductor on the chip surface is easily interfaced with other parts of the device and measurement setup.

The CPW dimensions W, S and d shown in figure 3.9 control the characteristic impedance Z_0 and phase velocity v for EM waves on the transmission line. Although the metal is entirely above the dielectric substrate the fields partially exist below the surface meaning the substrate's dielectric constant ε_r also affects waves in the CPW. Similarly, fields penetrating the superconducting metal will introduce a 'kinetic inductance' L_{kin} due to the inertia of charge carriers in the superconductor. The inductance L' and capacitance C' per unit length of a CPW are given by [53]

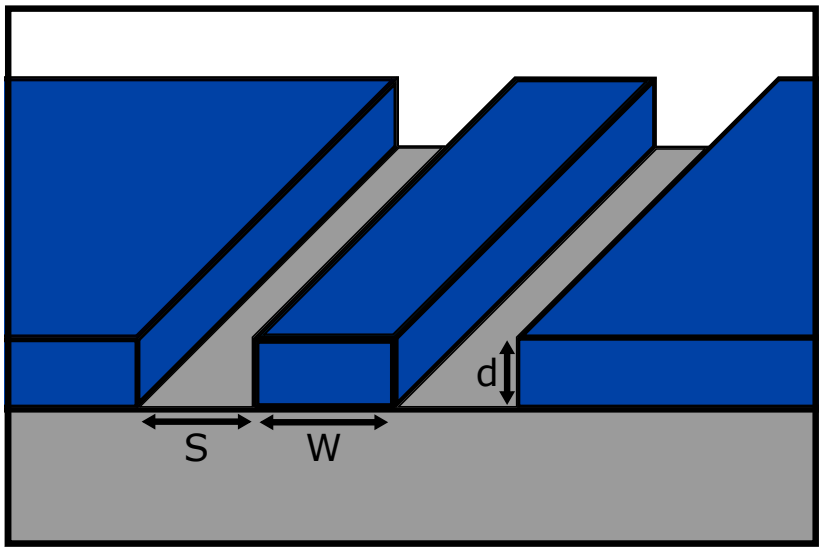

Fig. 3.9 Cross-section of a coplanar waveguide consisting of metal (blue) on a dielectric substrate (grey). Electromagnetic fields are mostly confined in the gap between the central conductor and the ground plane either side but penetrate partially into the dielectric and metal. The central conductor width W, gap width S and metal thickness d can all be controlled during fabrication and affect transmission line properties such as its characteristic impedance. The microwave feedline and resonators are made using this geometry.

$$\begin{aligned} L' &= \frac{\mu_0}{4}\frac{K(k_0')}{K(k_0)} + L_{\text{kin}} \\ C' &= 4\varepsilon_0\varepsilon_{\text{eff}}\frac{K(k_0)}{K(k_0')} \end{aligned} \tag{3.6}$$

where $k_0 = W/(W+2S)$, $k_0' = \sqrt{1-k_0^2}$ and K is the complete elliptical integral of the first kind. The effective dielectric constant $\varepsilon_{\text{eff}} = (1+\varepsilon_r)/2$ is the average of those for air (=1) and the substrate ($\varepsilon_r \approx 12$ for InP). L_{kin} will vary with material choice and metal thickness but is a small correction in typical Al resonators and so is ignored in the following equations. In chapter 6, it is accounted for due to the high L_{kin} of NbTiN used for those resonators. From these expressions the characteristic impedance Z_0 and phase velocity v can be found:

$$\begin{aligned} v &= \frac{1}{\sqrt{L'C'}} = \frac{c}{\sqrt{\varepsilon_{\text{eff}}}} \\ Z_0 &= \sqrt{\frac{L'}{C'}} = \frac{\mu_0 v}{4}\frac{K(k_0')}{K(k_0)} \end{aligned} \tag{3.7}$$

Introducing boundaries to a CPW transmission line defines a resonator with its length L determining the resonance frequency $f_r = v/4L$. For a given substrate, varying the resonator length L allows tuning of the resonance frequency while the CPW dimensions W and S control Z_0. An impedance close to 50 Ω is desirable for both the resonator and feedline in order to be well matched to each other and external MW circuitry which is normally also 50 Ω. The usable resonance frequency range is determined by the operating ranges of amplifiers and filters in the setup as well as being as close as possible to the microwave transitions of interest ($\sim$ 10 GHz for high transmission ABS modes) and so resonance frequencies around 6 - 7 GHz are used.

Part of a typical microwave device is shown in figure 3.10. CPW resonators are coupled capacitively to a common feedline at one end and inductively at the other to individual junctions as described in section 2.3. The resonators have slightly different lengths which separates their resonance frequencies allowing them to be measured without interfering with each other.

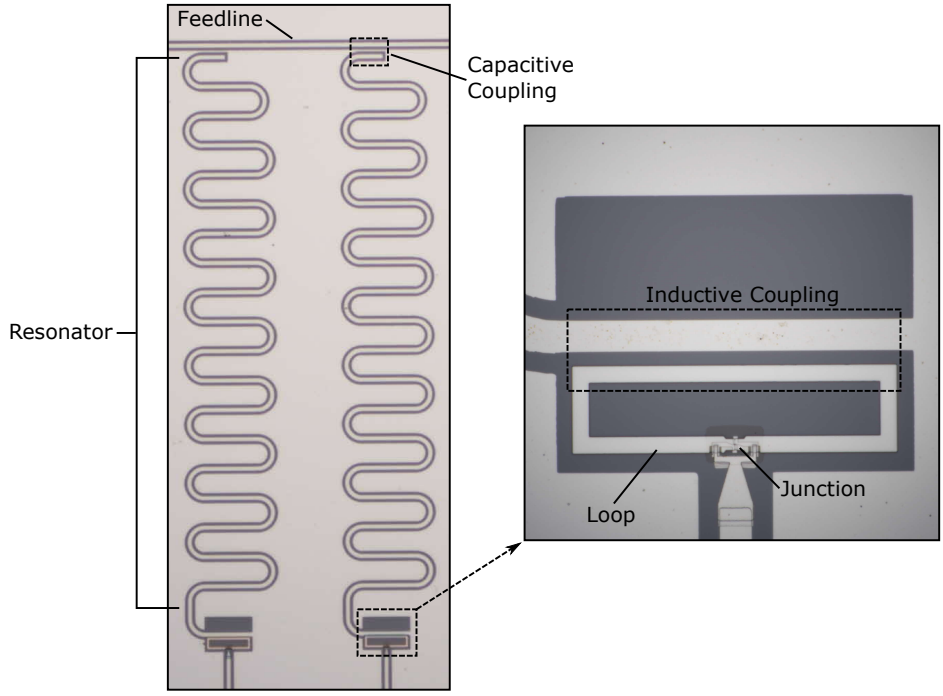

Fig. 3.10 A typical microwave device showing two CPW resonators coupled to a common feedline. The end of each resonator is coupled to a loop containing a semiconductor Josephson junction so changes in the junction affect its resonance frequency and power transmission which can be measured via the feedline.

Microwave Measurement Setup

Measurement of feedline transmission is performed using the setup shown in figure 3.11 in the Triton cryofree fridge used in chapter 6. Each microwave line has attenuators at the various temperature stages both to reduce the signal strength at the device and help thermalise the lines to each stage which together with the low-pass and eccosorb filters helps reduce noise along the lines.

A Rhode & Schwarz vector network analyser (VNA) is used to perform single-tone microwave spectroscopy of devices by sending microwaves to the device at a particular frequency and measuring the returning signal at the same frequency and this frequency can be swept to measure S21 as a function of frequency. The initial signal to the feedline input is sent from VNA port 1 through the 'cavity' line and the feedline output is sent to a travelling wave parametric amplifier (TWPA) for amplification at base temperature. The TWPA requires a microwave pump for amplification which is provided by a separate microwave source on the 'pump' line via a directional coupler. Isolators are placed either side of the TWPA to ensure power flow in one direction only. After passing through the TPWA the signal is amplified again by a Low Noise Factory cryo-amp and returns to the VNA at port 2 via the 'readout' line. DC lines are also present which can be used to apply voltages to gates and perform low frequency measurements as shown in section 3.2.

Using this setup, transmission through the device feedline can be measured by the VNA S21 parameter and the frequency can be swept quickly by the VNA to map out resonator response as in figure 3.12 which shows the amplitude and phase of a typical resonance. This can be fitted using equation (3.5) to extract the resonator parameters. Changes in the resonance shape can then monitored as a function of stimuli applied to the junction giving a high frequency measurement of Josephson junction dynamics.

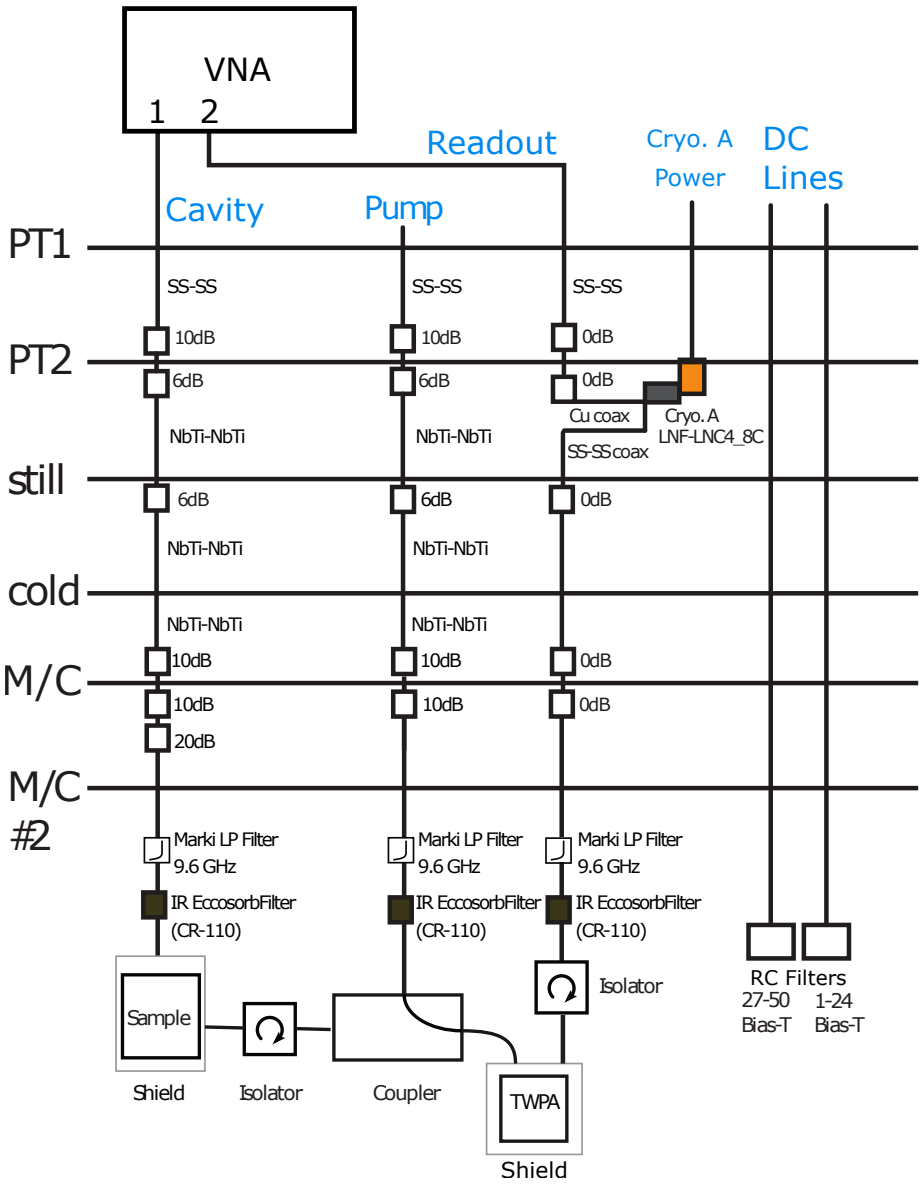

Fig. 3.11 Measurement setup for microwave measurements in Triton cryofree dilution fridge. The VNA outputs microwave signals from port 1 and measures the relative power input at port 2, S21. The 'cavity' line is connected to one end of the device feedline via the sample box. The other end connects to the travelling wave parametric amplifier (TWPA) which requires power supplied by the 'pump' line to amplify signals. Isolators ensure power flows in the correct direction through the TWPA. The return signal is amplified further by the Cryo Amp before returning to the VNA via the 'readout' line. Each microwave line has low pass and eccosorb filters to reduce noise. DC lines are available for additional control and transport measurements.

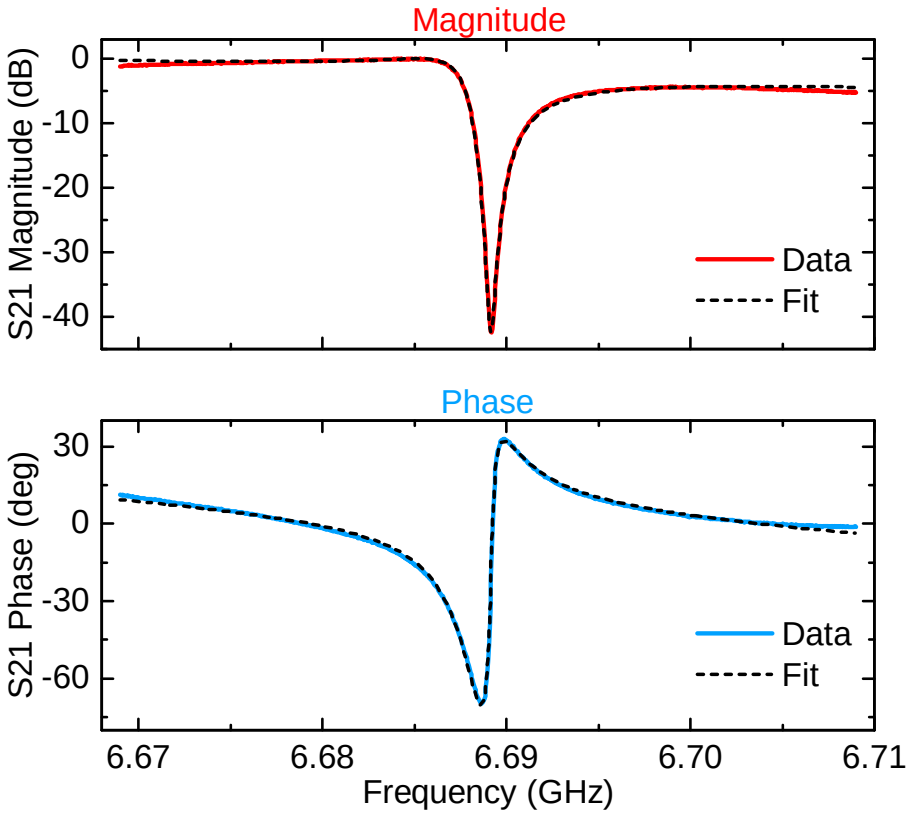

Fig. 3.12 Resonance of a superconducting quarter wave resonator coupled to a feedline. S21 is the relative power transmitted through the feedline measured by the VNA. (top) S21 magnitude against frequency shows a sharp dip signalling the resonance. (bottom) S21 phase plotted against frequency shows an abrupt shift in phase at the resonance frequency. The resonance in both magnitude and phase is fitted using equation (3.5) showing a good fit and allowing extraction of the parameters $f_r = 6.688$ GHz, $Q_i \sim 15000$, $Q_e \sim 2700$ ($Q_T \sim 2300$).

Chapter 4

Radio-Frequency Reflectometry on a Superconducting Tunnel Junction

A single tunnel Josephson junction is perhaps the simplest superconducting junction and it provides a useful test system to perform Radio-frequency (RF) reflectometry and transport measurements on the same device to see whether the results of the two can be correlated and what differences may arise. If reflectometry measurements can be related to the device transport properties of interest it could be a useful technique for measuring device dynamics at high frequency. High frequency measurements are less affected by $1/f$ noise and having a higher bandwidth available allows more averaging to increase signal to noise ratio (SNR) or tracking dynamics on fast timescales.

The device shown in figure 4.1 is an aluminium tunnel junction on undoped Si/SiO_2 fabricated and provided by Adam Esmail at the Microelectronics Group, Cavendish Laboratory. Details of the fabrication process can be found in appendix A.2 and ref [54]. Al is often the superconductor of choice for such devices since it is relatively simple to deposit by evaporation and becomes superconducting below temperatures ≈ 1 K which is easily accessible in dilution fridges. An undoped substrate is used to avoid the additional capacitance between the device and conducting Si present even at low temperature in doped Si substrates. The tunnel barrier in the measured device has a resistance of around $80\,\mathrm{k}\Omega$ at room temperature.

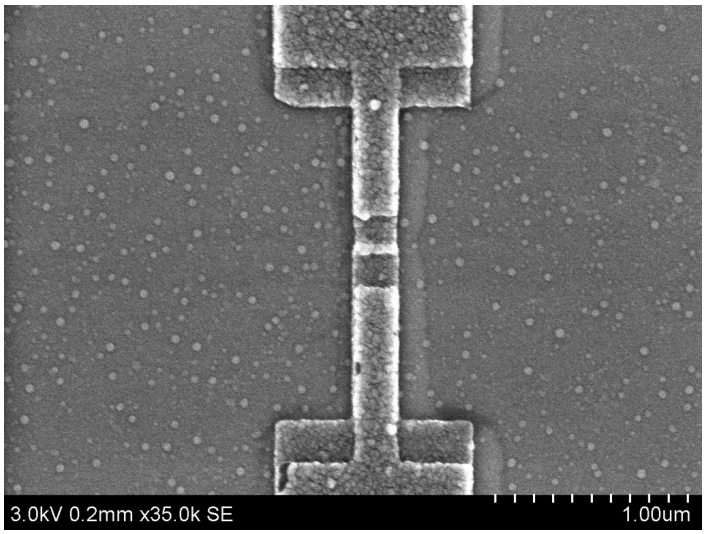

Fig. 4.1 SEM of Tunnel Junction Device made of Al on an undoped Si/SiO_2 substrate. Double angle evaporation with controlled oxidation produces the overlap in the middle where the tunnel barrier is.

4.1 RF and DC Comparison

The device is measured by RF reflectometry and DC transport using the setup outlined in section 3.3.1. Applying a small voltage excitation V from the lock-in amplifier (LIA) across the junction and measuring the current I flowing through as a result gives a direct measure of the differential conductance $G = dI/dV = 1/R$. In figure 4.2 the conductance is plotted as a function of DC bias voltage V_{SD}. In the superconducting state the density of states is gapped leading to a zero conductance region around $V_{SD} = 0$. Either side of this region peaks in conductance occur when the gap edge of the two leads are biased into alignment at $V_{SD} = \pm 2\Delta/e$. The gap edge in this device has a double-peak feature which can be caused by two slightly different superconducting gaps either side of the junction, possibly due to slight differences in the metal film between the first and second evaporation. However when a magnetic field is applied to this device later (figure 4.5) the double-peak disappears suggesting that it is instead due to magnetic flux trapped in the device which is removed upon sweeping the external field.

Near zero bias there are small peaks visible in the subgap region. A subgap conductance can occur due to multiple Andreev reflections (MAR) which produces conductance peaks at bias voltages $2\Delta/en$ where the order of the contributing MAR process is n (see section 2.2.4). However MAR features so close to zero bias would suggest a high order process and the strength of the MAR signature should scale as τ^n. In a tunnel junction all modes have

$\tau \approx 0$ so seeing any MAR signatures especially a high order one would be unlikely so it is unclear what the features visible in the data are caused by.

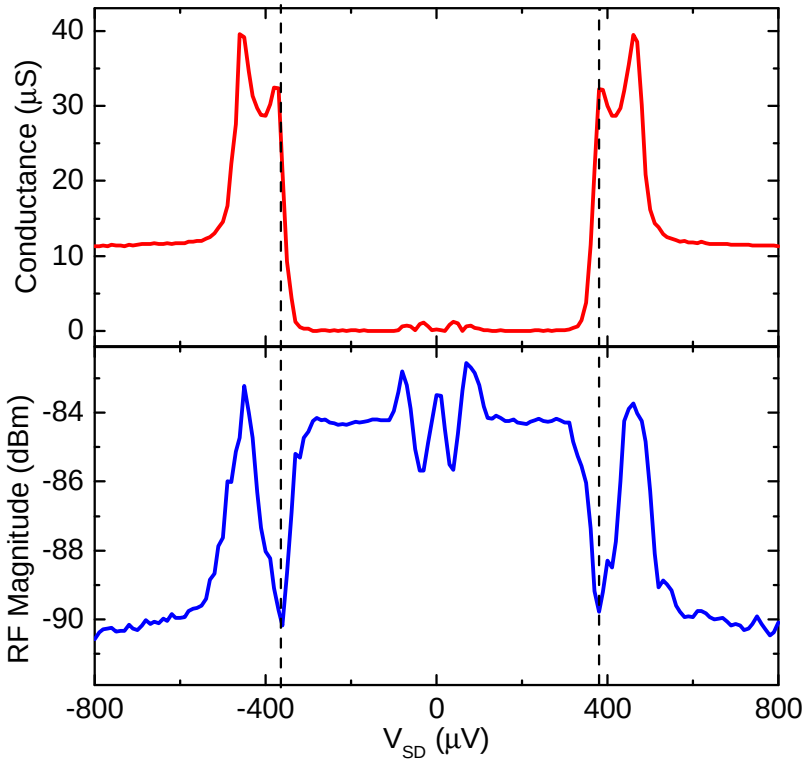

Fig. 4.2 Comparing the DC transport measurement of differential conductance (top) and RF reflectometry amplitude (bottom) against source-drain bias V_{SD}. The superconducting gap feature and sub-gap structure in conductance are reproduced in the reflectometry measurement. When the matching resistance is crossed at the dashed lines the relation between them reverses. The conductance has a double-peak at the gap edge which disappears when a magnetic field is applied (figure 4.5) suggesting it is due to trapped magnetic flux.

At the same time as the DC measurement, the RF reflectometry signal is monitored at the resonance frequency $f_r = 328$ MHz and the amplitude is plotted in figure 4.2. Comparing this to the DC conductance there are two distinct behaviours which have their boundary near the gap edge. Outside the gap the reflectometry signal increases monotonically with the conductance while inside the gap the sign is reversed with the decrease in conductance at the gap edge accompanied by an increase in reflectometry amplitude. The small subgap conductance peaks around zero bias also appear in the RF signal as proportionally larger peaks. The two opposite relations between the two measurements can be simply explained with reference to equation (3.3), when the transformed impedance crosses through the

matching impedance Z_0 the sign of the reflected power changes and so does the relationship between the RF signal and the resistance and so either side of the matching resistance R_m opposite behaviour is expected.

4.2 Temperature and Power Dependence

Being able to measure the DC and RF signals simultaneously is useful experimentally but a high RF power incident on the device may interfere with the conductance measurement. The measurement circuits themselves are isolated by the bias-T which contains a low-pass filter on DC side and a high-pass filter on the RF side but the RF power entering the device at the source acts like a high frequency voltage bias. The effect of this high frequency bias will be time averaged by the comparatively low frequency LIA and result in transport being probed over a wider voltage range than intended. This could have a similar effect to thermal broadening which spreads out the effective range of energies contributing to transport. If the broadening due to RF power is less than due to thermal broadening then the system should not be altered by the simultaneous measurement. To understand these effects it is useful to measure the temperature dependence of the device DC conductance and compare it to the effect of increasing RF power delivered to the tank circuit.

Figure 4.3 shows the DC conductance with source-drain voltage bias taken at three different temperatures. The inset shows the overall conductance trace while the main graph is a zoom on the gap edge. Compared to the base temperature of 50 mK the higher temperature plots appear almost identical except around the gap edge where there is a small reduction in the peak height and an increased conductance in the gapped region with increasing temperature. Thermal broadening is expected to have a significant effect on the tunnelling current when the thermal energy $k_B T$ is comparable to the superconducting gap $\Delta \sim k_B T_c$ for critical temperature of the superconductor $T_c \approx 1$ K for Al so it appears that even the highest temperature of 500 mK is too far below T_c to see a significant softening of the gap feature.

Similar conductance traces are taken while varying the RF power sent to the device via the tank circuit and shown in figure 4.4. At the lowest powers the conductance is largely unchanged but as power is increased a significant softening of the gap feature occurs with the crossover occurring between -100 and -90 dBm. The gap edge peaks are lowered in height and spread out in voltage while the gapped region is reduced in size as the outer regions gain a finite conductance. The connection between temperature and RF power can be quantified

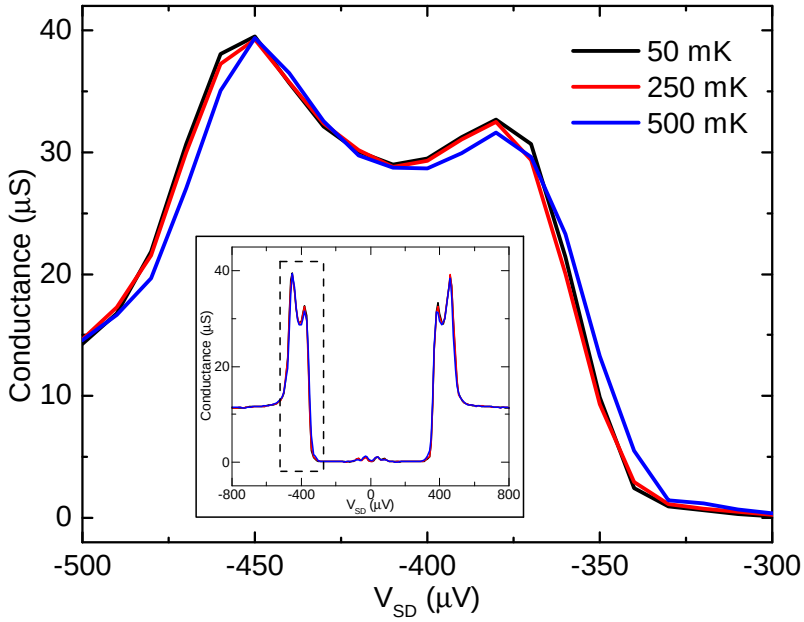

Fig. 4.3 Temperature dependence of conductance. The overall trace (inset) shows little difference between temperatures. Zooming in (main plot) it can be seen that the lowest temperature trace is highest at the peaks and lowest in the gap although the difference is very small. This behaviour is expected since increasing temperature should soften the gap but perhaps the temperature range here does not come close enough to the Al critical temperature $T_c \approx 1$ K to see a more significant change.

using $eV = k_B T$ for the voltage bias V corresponding to the temperature T and taking V as the RF signal amplitude. Converting the fridge temperature of 50 mK gives an equivalent RF power of around -94 dBm which is consistent with where in power the crossover between hard and soft gap occurs in figure 4.4.

The effect of temperature and RF power do not appear to match up. An RF power equivalent to a temperature of 50 mK is able to disrupt the gap feature significantly while directly increasing the temperature up to 500 mK shows little change in the conductance traces. It is not clear why this is the case but two possible reasons are: (1) The effect of RF power is not the same as temperature and the nature of the disruption seen is not due to an actual softening of the superconducting gap but the RF power altering the conductance measurement in some other way. (2) The device is poorly coupled to the heater and thermometer meaning its temperature, and therefore the conductance, do not change as much as expected.

A high enough temperature is expected to soften the superconducting gap and alter transport significantly but in this case we cannot reach a high enough device temperature to observe

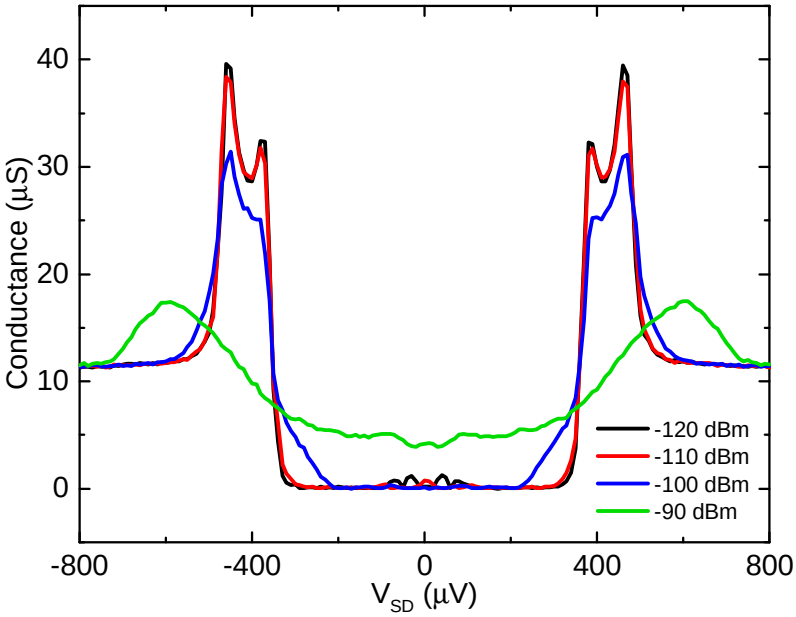

Fig. 4.4 RF power dependence of conductance. Measuring conductance while increasing the RF power shows that too high a power will soften the gap feature and make the conductance measurement inaccurate. When performing simultaneous reflectometry and transport measurements the RF power must be kept low enough to avoid this.

this effect directly. RF power has a similar effect and it can be seen that a high enough RF power can completely change the result of the DC conductance measurement so it is important to choose a low enough power to avoid this while maintaining a reasonable signal to noise ratio when performing such simultaneous measurements.

4.3 Magnetic Field Dependence

A magnetic field is applied out-of-plane to the device to measure the effect on DC conductance and compare to the simultaneously measured RF response. Figure 4.5 shows the DC and RF measurements as a function of magnetic field and source-drain bias. The differential conductance G is shown in figure 4.5(a) with the maximum gap feature visible at $B = 0$ which decreases as the field is increased either side until it completely closes around ± 50 mT. Figure 4.5(b) shows line sections at the indicated B-fields in (a). The zero-field conductance is different to previous measurements near the gap edge with the double peak replaced by a single peak. This suggests that the double peak was caused by trapped flux somewhere in or near the device which was removed once an external magnetic field was applied. At 20 mT

the gap begins to reduce but is still clearly visible and by 40 mT only a small range around zero bias remains gapped until it is completely gone by 60 mT.

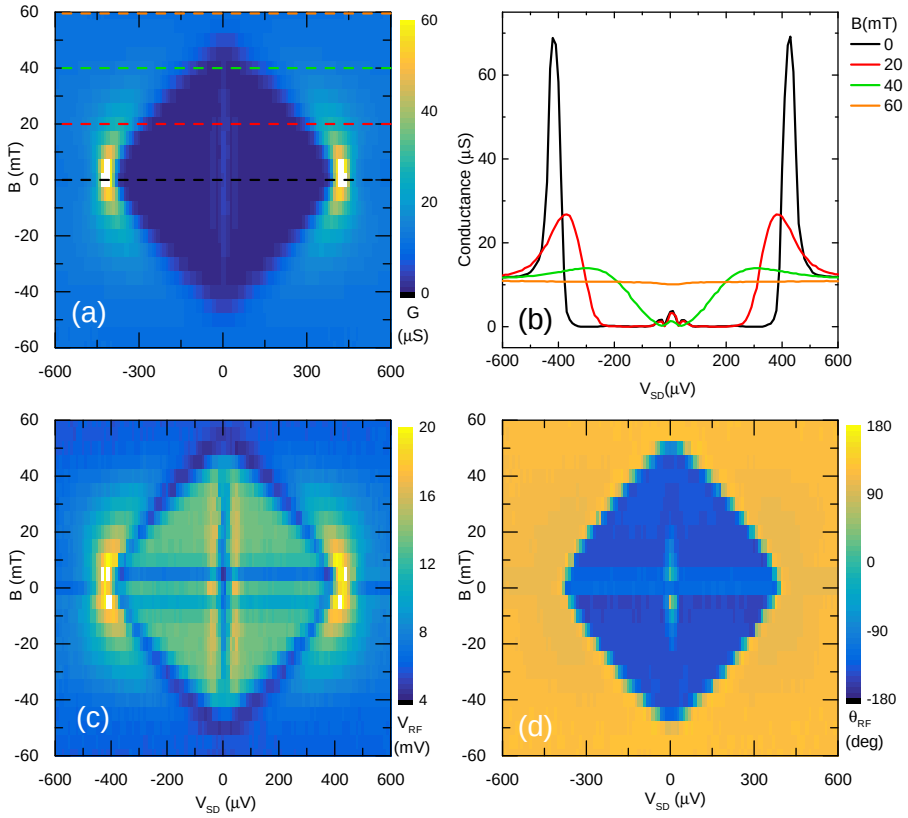

Fig. 4.5 Comparing reflectometry and transport on the same device with V_{SD} and magnetic field B. (a) Differential Conductance G. The gap feature reduces in extent with increasing field until it closes completely at $\approx \pm 50$ mT producing a diamond-shaped structure. (b) Line sections at the indicated fields in (a) showing the gap changing with field. The double-peak at the gap edge seen previously (see figure 4.2) is not there anymore suggesting it was caused by some trapped flux or impurity which was removed by raising the temperature or field. (c) Reflectometry amplitude and (d) phase showing the same diamond structure as conductance, as well as some features near zero field and zero bias more clearly visible here than in transport.

The amplitude and phase of the RF signal are shown in figure 4.5(c) and (d) respectively. Both exhibit the same diamond shape of the superconducting gap edge as seen in the conductance. Within the gap there is additional structure in the RF signals which are either not present or only weakly visible in conductance, most notably in phase where there is a peak at zero bias which first appears away from zero field and then diminishes as field increases. This along with the features near zero bias in amplitude may correspond with the small peaks seen near zero bias in conductance but in RF they are much more clearly visible. There are also abrupt

changes in the background inside the gap either side of zero field in both RF signals which is not visible in conductance.

While the RF reflectometry measurement produces very similar results to measuring the conductance directly some slight differences are observed and certain subgap features appear much more prominently in the RF measurement. This is to be expected since in principle the RF measurement is sensitive not only to the device resistance but its total impedance which includes the inductive and capacitive parts. Most notably the non-linear Josephson inductance will be a significant part of the total inductance at energies below the gap and changes in this with magnetic field may be what is being seen in the subgap structure of figure 4.5(c) and (d).

4.4 Response Curve

The sensitivity of RF reflectometry to changes in the device impedance will have an impact on its use in situations where the signal to noise ratio is small, such as signals due to single electrons in the time domain. The response of our system can be characterised since the conductance and RF signal are measured simultaneously.

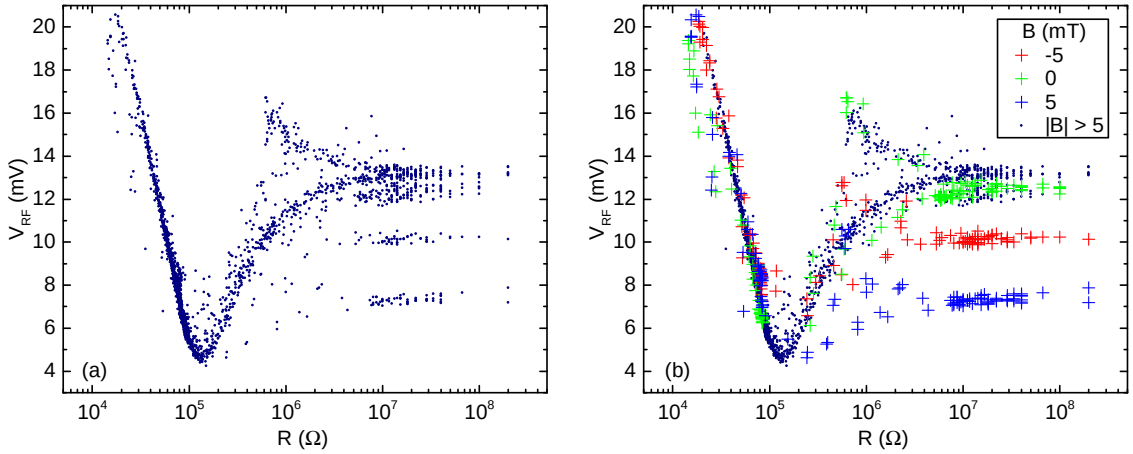

Fig. 4.6 Response Curve. (a) Curve initially obtained by plotting resistance and RF amplitude taken from figure 4.5 against each other. (b) Isolating the data points based on their position in magnetic field in 4.5 shows that the additional plateaus are entirely due to data from fields -5, 0 and $+5$ mT.

Converting the differential conductance data from 4.5(a) into differential resistance $R = 1/G$ and plotting parametrically against reflectometry amplitude V_{RF} in 4.5(c) produces the

response plot shown in figure 4.6(a). At low resistances the amplitude decreases with increasing resistance and this is the highest sensitivity region (highest $\frac{dV_{RF}}{dR}$). At the matching resistance $R_m \approx 10^5\ \Omega$ there is a minimum in RF amplitude and beyond that the response changes sign with amplitude now increasing with R. The amplitude eventually saturates at very high resistances and the sensitivity approaches zero.

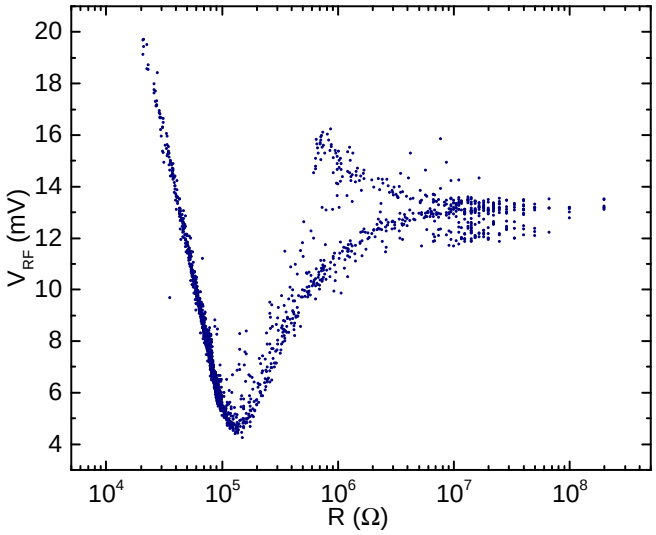

Fig. 4.7 Response Curve. Removing data from B-fields near zero in figure 4.6 removes the other plateaus leaving only one main curve. A small branch starting from above around $10^6\ \Omega$ and saturating at the same level as the main curve remains. Apart from this, the main curve gives the overall response of the reflectometry setup to a change in device resistance.

At the high resistance end of the data there appear to be three distinct plateaus which branch off from the main curve above the matching resistance. Colouring the data by which magnetic field value it comes from in 4.5(b) reveals that the extra plateaus, as well as various other points which do not lie on the main curve, are due to data from ± 5 mT. Looking back at figure 4.5 the RF data does have slight differences in the background around zero field which could be artefacts from the magnet power supply switching through zero or perhaps some low field effect which has not been considered. In order to obtain a clear response curve those data are excluded and the rest plotted in figure 4.7. Apart from the small branch coming down at around $10^6\ \Omega$ the data is now a single curve.

The response curve shows the relationship between RF reflectometry signal and device resistance from which the matching resistance and measurement sensitivity can be found. Since changing device or tank circuit elements will alter the response, such a response curve is a useful tool to see in what device resistance range the measurement is most sensitive and to alter the circuit accordingly for a given device. As well as measuring the response directly,

being able to predict it for a given set of tank circuit parameters would be useful as well as testing the validity of the effective circuit used to understand the system. The response curve should be related to the functional form of the reflection coefficient Γ given by equation (3.3).

The simple form of this equation means that at very low and very high R the reflection coefficient will always go to 1, however in the data at high R the reflected power saturates at a lower value than at low R so the simple circuit model shown in figure 4.8(a) used to derive equation (3.3) does not fully capture the observed dynamics. One simple addition would be to introduce a series resistance r in front of the inductor which represents dissipation in the tank circuit, for example PCB wiring resistance or the lumped element inductor which will always have a finite resistance and cannot be treated as a pure inductance. The modified circuit is shown in 4.8(b) and its impedance at resonance is given by

$$Z = \frac{L}{RC} + r \tag{4.1}$$

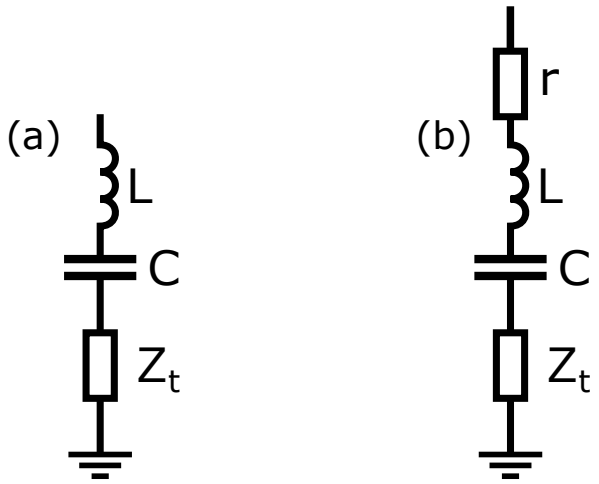

Fig. 4.8 (a) Reflectometry circuit model assumed previously. (b) Modified circuit including a series resistance r to better account for high R behaviour seen in data response curve.

Theoretical response curves are calculated at different values of r using the Matlab RF Toolbox by constructing the circuit 4.8(b) and finding the S11 parameter as a function of R and r which is given by the reflected power ratio $|\Gamma|^2$. These are shown in figure 4.9 along with the data which has been converted from the demodulated voltage V_{RF} into the power ratio in dB to more easily compare to the theoretical reflected power S11. Focusing first on the model, increasing r shifts the matching resistance up and reduces the value at which the

high R data saturates. The first change is easily understood since the inclusion of r shifts the impedance matching condition:

$$\frac{L}{R_m C} = Z_0 \longrightarrow \frac{L}{R_m C} = Z_0 - r \tag{4.2}$$

while the second is a result of the high R limit:

$$\Gamma(R \to \infty) = \frac{r - Z_0}{r + Z_0} \tag{4.3}$$

At $r = 50\,\Omega$ where $r = Z_0$ there is no minimum in S11 and the high R limit of reflected power is close to zero (large negative in dB). At higher r (not shown) the model has the same form as $r = 50\,\Omega$ but the high R plateau increases with r. Since the data has a clear minimum at the matching resistance only values of $r < Z_0$ need to be considered here.

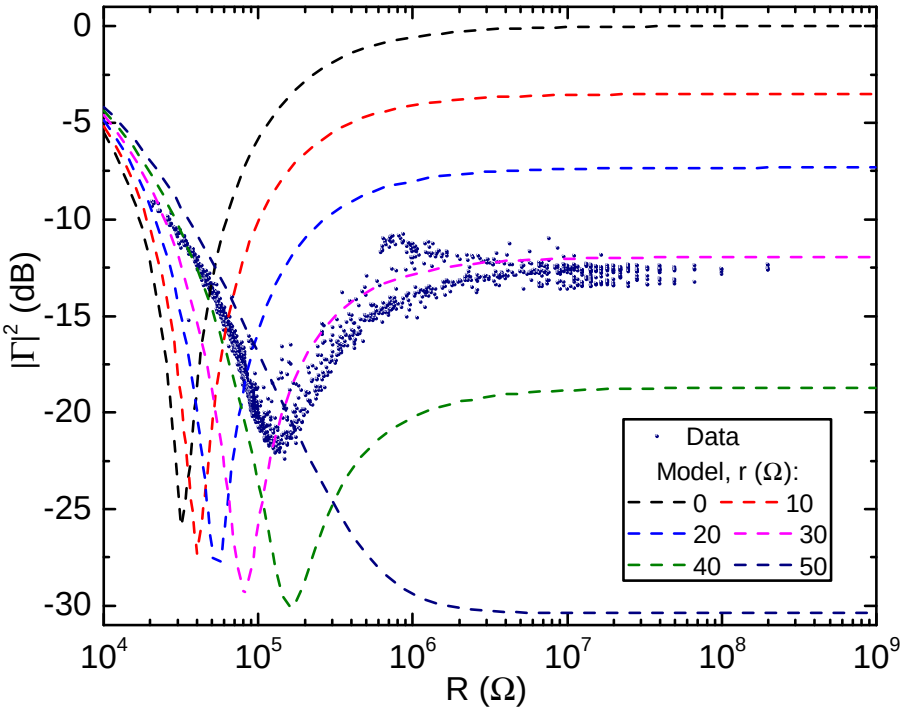

Fig. 4.9 Response Curve with model. The high R behaviour is fit best by $r = 30\,\Omega$ but the matching resistance falls between 30 and 40 Ω so this model cannot capture all features of the data. An extension to the model where L and C can vary as well or adding more elements to represent extra parasitic inductances and capacitances may improve the fit.

Comparing to the data, it seems that $r = 30\,\Omega$ most closely matches the high R plateau while the position of the minimum (matching resistance) would be better fit by something between 30 and 40 Ω. It appears that with this circuit model no single value of r will fit the data completely. The values of L and C in the model are kept fixed since L is a lumped element inductor of known inductance L = 620 nH and C can be inferred from L and the observed resonance frequency. However the assumption that L is exactly the value of the lumped element inductor may be incorrect since other parasitic inductances and capacitances will be present in the real circuit which alter L and C [55]. A different combination of L and C such that the resonance frequency is $f_r = 328$ MHz but with a different total impedance would have a different response curve and matching resistance. Therefore allowing L and C to vary as well as using a more complicated circuit including additional resistive and parasitic reactive elements may capture features in the data better, but the relatively simple model used here can at least be used to suggest that the resistive part of the circuit is around r = 30 to 40 Ω.

4.5 Conclusion

These measurements on a superconducting tunnel junction show that high-frequency measurement using RF reflectometry corresponds well with transport measurements of device resistance. Reflectometry is sensitive to the total impedance and not just resistance so it could measure changes which transport measurements cannot. These make reflectometry a viable technique for probing device impedance at high bandwidth meaning quick measurements and sensitivity to fast time domain dynamics are possible. Producing a response curve shows the matching resistance near which reflectometry is most sensitive and this can be altered by changing the tank circuit elements to ensure the measurement is sensitive in the most useful range for a given device. A simple model with an additional resistance in the tank circuit allows parts of the response curve to be fitted but a more complicated model would be required for fully predicting the response from a particular combination of device and tank circuit parameters.

In this experiment the device resistance is altered by source-drain bias and magnetic field and the data is split between very low conductance inside the gap and intermediate conductance outside the gap with values in between mostly coming from the steep gap edge. A high mobility semiconductor Josephson junction measured this way could also be controlled by a gate allowing gradual tuning of the device resistance from the tunnelling regime explored

here in the tunnel junction device all the way to the ballistic transport regime where Andreev bound states deep within the gap become important to transport.

Chapter 5

Superconductor - Semiconductor Josephson Junctions

In the reflectometry measurements on a tunnel junction (chapter 4) it was established that the junction impedance can be measured at high frequency. To investigate Andreev bound states (ABS) using the same technique requires a Josephson junction made with a semiconducting or metallic material in which ABS contribute significantly to transport. A semiconducting junction also has the advantage that the carrier density can be controlled using a gate to explore different transport regimes not possible in the tunnel junction.

Here I show initial progress towards CVD graphene Josephson junctions which were mainly hindered by high contact resistances and low mobility after fabrication. Both of these issues are alleviated by moving to an InAs-based semiconductor with epitaxially grown Al metal allowing fully proximitised Josephson junctions to be made. I present measurements on one such device which shows a hard gap and suggests that using a split-gate to form a QPC can reach the ballistic few-mode regime.

5.1 Graphene Josephson Junctions

The connection between conduction and valence bands at Dirac points mean that the carrier type in graphene can be continuously tuned between electrons and holes. Carriers in graphene have a high mobility over a range of carrier densities meaning that junctions formed using

graphene can have ballistic transport through them. These practical factors combined with the massless Dirac fermion nature of the carriers make graphene Josephson junctions (GJJs) theoretically interesting. Induced superconductivity and a supercurrent tuned continuously between electrons and holes has been shown in graphene Josephson junctions [56, 57, 58] and this has opened the door to more thorough investigation of such hybrid systems.

In the earlier work mechanically exfoliated graphene flakes were directly patterned with metal contacts to form the junctions. Encapsulating the graphene flakes in hexagonal Boron Nitride (hBN) keeps the mobility in the graphene high and low resistance edge contacts can be made to the graphene [59, 60, 61]. These devices must be designed individually for each flake depending on its size, shape and orientation on the chip making it difficult to scale such a process to large numbers of devices. For this reason we use graphene grown by chemical vapour deposition (CVD) which can be grown in large sheets. In this situation large numbers of repeating structures can be designed and fabricated to increase the yield and potentially test a large number of devices at once. The graphene used was grown at the Centre for Advanced Photonics and Electronics (CAPE) and provided by Jack Alexander-Webber and Abhay Sagade. The graphene was grown by CVD on Cu substrates before being transferred to Si/SiO_2 wafers using a PMMA-based wet transfer method [62].

Figure 5.1 shows an overview of the fabrication process after the graphene transfer which is explained in more detail in appendix A.3. Only one junction is drawn but in the actual devices this type of structure is repeated several times on a typical 10 mm x 10 mm chip. The contacts to graphene are made as the first step by electron beam lithography (EBL) since exposing the graphene to repeated polymer layers (especially photoresist) for multiple lithography steps reduces its quality and increases contact resistance [63]. Making the contacts first by EBL ensures the graphene under the contacts has the minimum possible polymer residues. After isolating the mesa and testing at room temperature using a back gate, working devices were encapsulated with an Al_2O_3 dielectric to protect the graphene from further impurities and allow devices made on undoped Si to be controlled by top gating at low temperature. An undoped substrate is required for RF reflectometry so most devices were fabricated on undoped Si to allow for this.

5.1.1 Contacting Graphene

One of the main challenges in obtaining a fully proximitised junction is the contact resistance between the superconductor and graphene since a low interface transparency reduces the

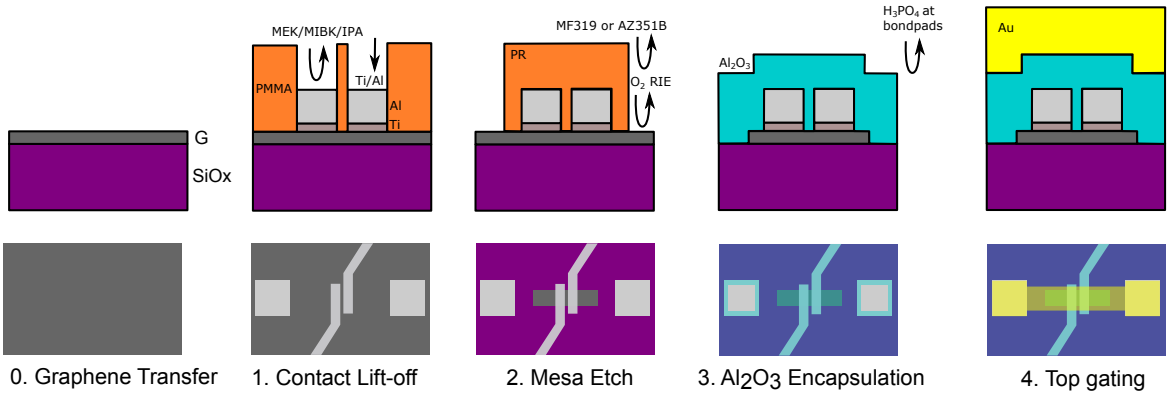

Fig. 5.1 Overview of fabrication process for graphene Josephson junctions.

induced superconducting gap [64]. Contact resistance in graphene devices is affected by a number of factors which are understood to varying degrees [65, 66].

Work function difference between the contact metal and graphene and doping of the graphene under the contact is a major factor intrinsic to the materials used [67, 68, 69]. Aluminium is often the superconductor of choice for making Josephson junctions as it can be thermally evaporated to make small structures without damaging the contact region. Unfortunately the Al-graphene binding energy is calculated to be very low [70] suggesting a weak physical contact, and indeed experimentally Al contacts to graphene tend to delaminate [71].

A Ti sticking layer can help with adhesion of Al to graphene so initially Ti/Al contacts were made to the graphene but there were often severe adhesion problems and the device resistances were higher than expected suggesting a high graphene sheet resistance in the junction or high contact resistance both of which need to be reduced. Later devices used Pd as the sticking layer as it has been shown to bond more strongly with the carbon in graphene [72] and produce low resistance contacts [73, 74]. As well as this Pd/Al contacted graphene junctions have shown a superconducting proximity effect [75] so Pd is a valid choice for superconducting graphene devices.

Another way to improve metal adhesion and contact resistance on graphene is using edge contacts. At graphene edges additional carbon orbitals participate in bonding to a contact metal so a higher interface transparency is expected at graphene edge contacts compared to contacts only on the surface of graphene [76]. With suspended or encapsulated graphene it is possible to perform an etch and then make a self-aligned contact to the exposed graphene edge. For large-area graphene on a substrate, full edge contacts cannot be as easily made but the ratio of edge to surface contact can be improved by etching out holes or trenches in the

contact region of the graphene before metallisation which has been shown to produce low resistance contacts [77, 78, 79].

Exposing the whole contact region to a gentle oxygen plasma can also reduce the contact resistance by introducing defects in the graphene sheet at which edge contacting could occur [71]. This method does not require additional lithography so we opted for a light etch in an O_2 RIE to remove EBL resist residues and possibly introduce some edge contacting. The adhesion of metal to graphene was greatly improved by the light etch but it also caused metal lift off on the smallest junctions of length 200 and 300 nm to fail. These changes did not cause a significant decrease in contact resistance but by performing the O_2 RIE light etch a higher yield was obtained which allowed more testing of subsequent devices.

Contact Resistance

Measuring the contact resistance accurately is not possible with the two-terminal devices so in later batches, devices which could be used for transfer length method (TLM) measurements were made as shown in figure 5.2. TLM involves measuring the resistances of several junctions of equal width W and varying length L. The total measured resistance of a junction is given by a sum of contributions from the graphene sheet resistance (ρ_s) and the contacts (R_c at each contact):

$$R = \rho_s \frac{L}{W} + 2R_c \tag{5.1}$$

Ideally the junctions are from the same mesa with similar doping so a constant sheet resistance in each junction region can be assumed. A plot of R vs L should be linear with slope relating to this sheet resistance and intercept giving the contact resistance. In practice it was difficult to find devices which showed a clear linear relationship, probably due to differing doping between junctions even at the same gate voltage or other contributions to the total resistance not accounted for here. Without the Dirac point being visible in many devices it is difficult to find the point where each junction has the same carrier concentration but in two TLM structures a linear relation was observed and fitting to the above equation gives contact resistances R_c of 4.76 kΩ and 1.65 kΩ respectively. Using the appropriate mesa widths W for each gives the specific contact resistivity $R_cW = 28.6$ and 16.5 kΩ µm.

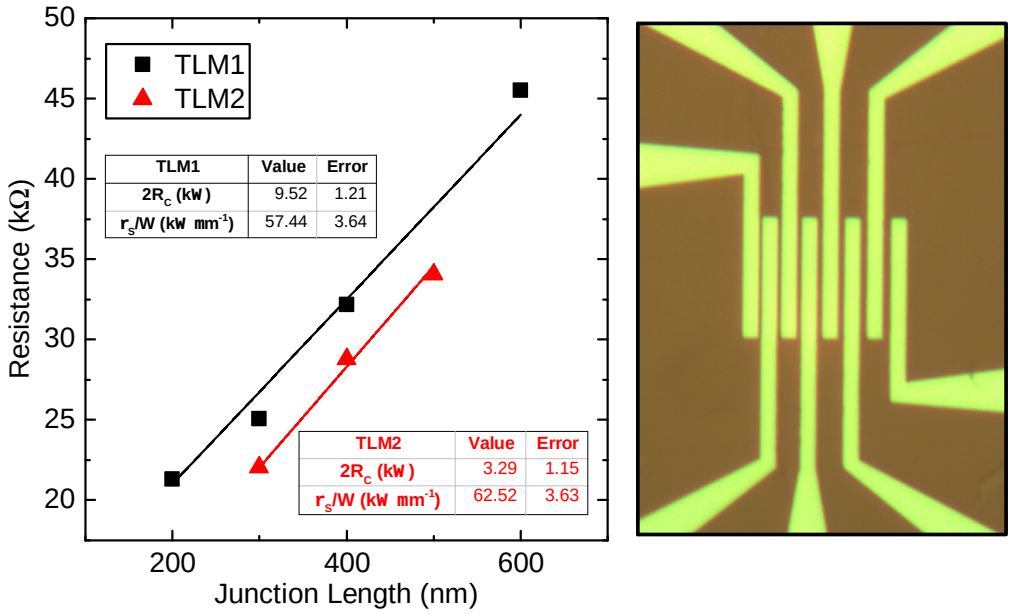

Fig. 5.2 TLM measurements. A TLM device consists of an array of juncions with progressively increasing lengths and constant width (TLM contact pattern shown on the right). Resistance vs junction length at room temperature is plotted for two TLM devices giving straight lines which can be fitted to find the contact resistance as the intercept. Most of the TLM devices measured did not show this linear relation meaning perhaps the assumption that doping is constant across the different junctions on the same mesa does not hold for these devices.

Equation (5.1) can be written in terms of the carrier density n and mobility μ using $\rho_s = 1/\sigma_s = 1/e\mu\sqrt{n^2+n_0^2}$:

$$R = \frac{L}{We\mu\sqrt{n^2+n_0^2}} + 2R_c \tag{5.2}$$

where e is the electron charge and n_0 is the residual carrier density at the Dirac point.

In some devices the Dirac point can be reached allowing the relation between gate voltage and n to be found and so the data can be fitted using the above equation (5.2) [80, 81]. The result for one junction from the final batch of devices is shown in figure 5.3 giving $R_c = 1.18\,\mathrm{k\Omega}$ and $R_cW = 11.8\,\mathrm{k\Omega}\,\mu\mathrm{m}$. This value is lower than the TLM devices from an earlier batch suggesting at least a small improvement in the metal-graphene interface.

Although some improvement was seen across the devices fabricated here, the contact resistivities measured overall, $R_cW \approx 10 - 30\,\mathrm{k\Omega}\,\mu\mathrm{m}$, are very high compared to typical

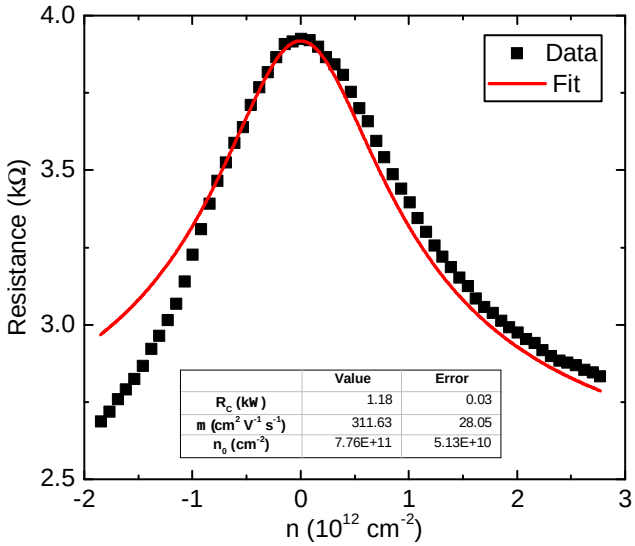

Fig. 5.3 When the Dirac point can be reached with enough data either side, a fit to equation (5.2) can be performed to find another value of R_c to complement the TLM measured value. The fit also has the mobility as a parameter which if accurate is quite low for graphene, suggesting again that transport will be poor in these devices.

metal-graphene contacts which are often <1 kΩ µm and as low as 35 Ω µm [60] in devices where supercurrent effects are seen. Therefore the transmission through these graphene junctions is unlikely to be high enough to achieve a full superconducting proximity effect meaning further work would be required to achieve a more transparent metal-graphene interface.

5.1.2 Encapsulation and Gate Response

Large area grown graphene is made up of separate grains due to growth starting in different places with differently oriented lattices. When these differently oriented grains meet there is a grain boundary where the material transitions between orientations and structures different to graphene appear. During fabrication of GJJs the graphene in the junction is exposed to polymer resists as well as water from the atmosphere and impurities such as these tend to accumulate at grain boundaries and other defects. If the junctions contain many impurities the graphene mobility will be low and the sheet resistance high due to a lower mode transmission across the junction. This will negatively affect ABS formation and superconducting transport. Using graphene with large grains reduces the chance of devices containing a grain boundary.

Encapsulating such large grain graphene with a dielectric has been shown to improve the doping and mobility [62].

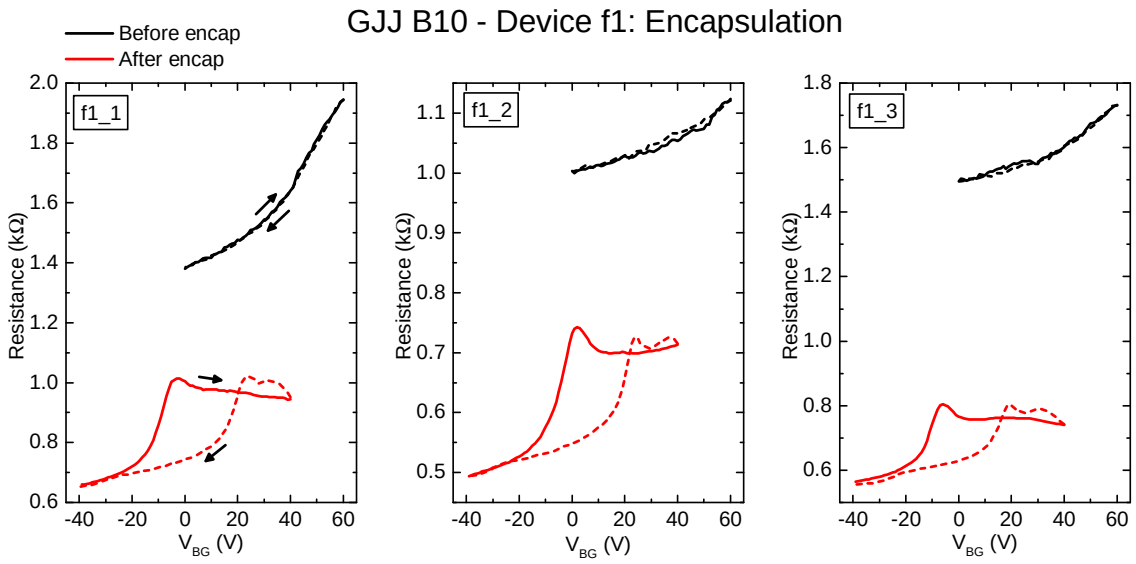

Fig. 5.4 Effect of encapsulation on device response at room temperature. Encapsulating reduces the doping and device resistance but introduces hysteresis, perhaps due to imperfect dielectric growth or trapped impurities. The asymmetry is likely due to the formation of p-n junctions in the graphene on one side of the Dirac point.

For the devices on undoped Si a dielectric is required anyway for gating at low temperature so the devices were encapsulated using Al_2O_3 grown by atomic layer deposition (ALD). Figure 5.4 shows the effect of ALD dielectric encapsulation on three devices from the same chip. Before encapsulation the resistance peak of the Dirac point is at a large positive voltage outside the accessible range of the measurement and the up and down sweeps show no hysteresis. Encapsulating shifts the Dirac point close to zero volts but the response is not symmetric, being much flatter on the n-type side. The response of all three devices also shows significant hysteresis.

The reduction in graphene doping can be explained by the encapsulation process pushing out water and passivating charged impurities and the dielectric acting as a barrier to subsequent dopants. The asymmetry and hysteresis are undesired and may be results of encapsulation but their appearance can be explained. In general graphene under the metal contacts will be doped differently to that under the dielectric. Sweeping the back gate globally changes the graphene doping but will do so more strongly in the junction than under the contacts which is pinned to the doping set by the graphene-metal interface. Assuming the doping under the contacts always stays p-type then when the junction graphene is p-type the devices as a

whole is a p-p'-p junction. In comparison on the n-type side the device is a p-n-p junction. In the latter situation the additional p-n interfaces will reduce transmission and so increase resistance compared to the former which results in a resistance and mobility asymmetry about the Dirac point. The appearance of hysteresis is likely due to charged impurities trapped in the dielectric which alter the electric field at the graphene. If they are pinned until a high enough field is applied which can move them, the gate response will show hysteresis.

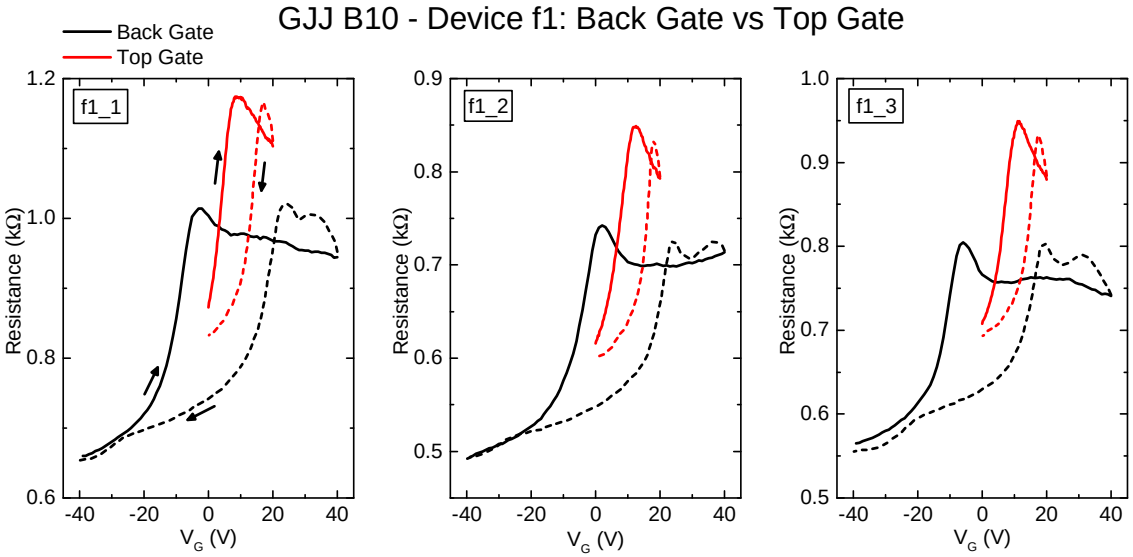

Fig. 5.5 Comparing the effect of back and top gates on device resistance at room temperature. The back gate data was taken before the top gate was fabricated while the top gate data was taken with the back gate at 0 V. The overall response is the same in both but the top gate shows a stronger lever arm and higher device resistance.

In principle growth by ALD should form atomically flat layers of dielectric which are grown sequentially to the desired thickness. However the graphene is not flat to begin with due to roughness in the SiO_2 substrate below. Impurities trapped at defects can act as multiple nucleation sites for the ALD growth leading to non-uniform layers. Some of the impurities can also remain trapped under the dielectric after growth. The result is dielectric which exhibits sub-optimal electrical properties such as highly doping the graphene, current leakage when top gated and gate hysteresis. These issues will reduce device yield so electrical testing at major fabrication steps can identify which devices are suitable to move on to the next step.

Figure 5.5 shows measurements of the same three devices after fabricating a top gate along with the back gate response from before for comparison. Qualitatively the response is the same for both gates, as expected, since the main effect of both is to change the carrier density

in the junction region. The stronger lever arm of the top gate is evident as the response from the back gate occurs over a larger voltage range. The overall value of resistance is different after top gating so it seems the top gate fabrication process or presence of top gate metal increases the junction resistance. Although gate hysteresis still occurs with the top gate, it is small enough that the Dirac point can be reached sweeping both up and down. There is only a small change in doping compared to before top gating, and no significant top gate leakage is seen in these devices. Therefore the encapsulation and top gating process used here is viable for producing junction devices suitable for low temperature measurement.

5.1.3 Low Temperature Measurements

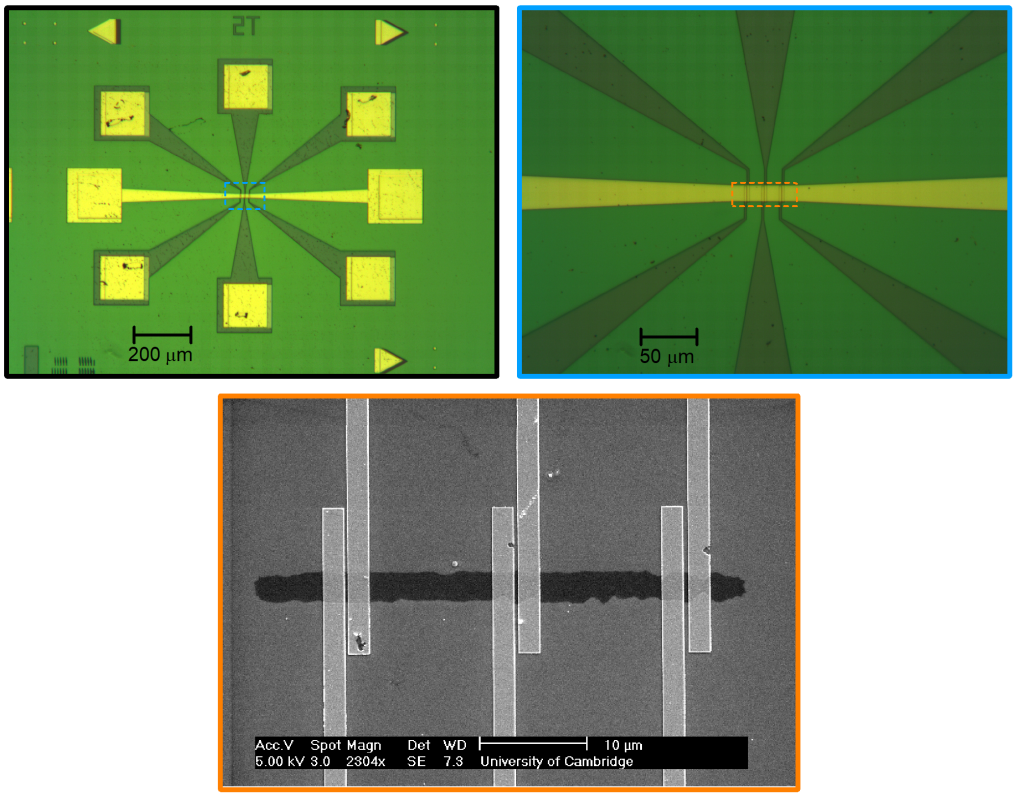

Fig. 5.6 Typical two-terminal GJJ device. (top) Optical images showing a single device consisting of three junctions. The junction lengths are 300, 400 and 500 nm going left to right and have a common top gate. (bottom) The SEM shows a device before top gate deposition so that the graphene mesa is visible.

Although the problem of high contact resistance had not been solved and other issues with the dielectric encapsulation process remained, some devices from the final batch were cooled

down to fridge temperature (50 mK) to get an idea of their superconducting properties and inform any future work on this type of device. Figure 5.6 shows a typical device consisting of three junctions arranged on the same graphene mesa with a common top gate. In this cooldown, device c1 and d1 were connected but junction c1_3 did not conduct so there were 5 junctions available to measure.

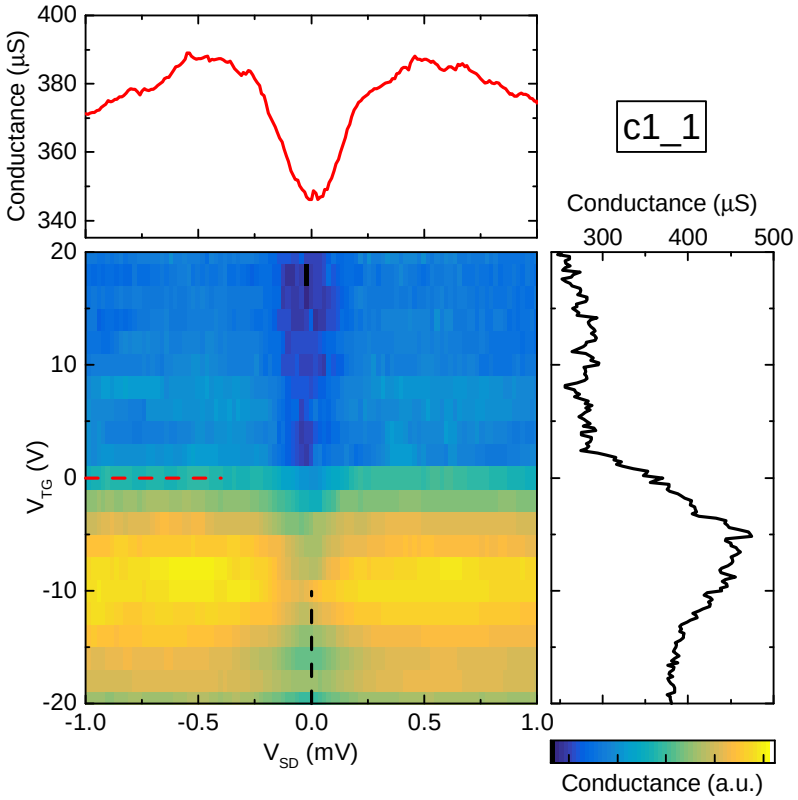

Fig. 5.7 Low temperature (T = 50 mK) measurement of two-terminal conductance against source-drain voltage bias V_{SD} and gate voltage V_{TG} on device c1_1. Dotted lines indicate where the line sections along the edges are taken. The region of lower conductance around zero bias, seen more clearly in the horizontal line section, appears to be a soft superconducting gap. The soft gap conductance dip narrows and become less deep around -10 V before opening up again below. This does not seem to be the Dirac point as it is a maximum in conductance. It could be that the p-n junction effect noted in figure 5.4 which reduces interface transmission at some gate voltages also causes a smaller superconducting gap to be induced.

Figures 5.7 and 5.8 show the two-terminal differential conductance as a function of top gate voltage (V_{TG}) and source-drain bias (V_{SD}) for two junctions c1_1 and c1_2 from the device c1. Junction c1_2 has a much lower conductance perhaps due to some additional impurity in the junction or a higher contact resistance, however qualitatively it behaves similar to

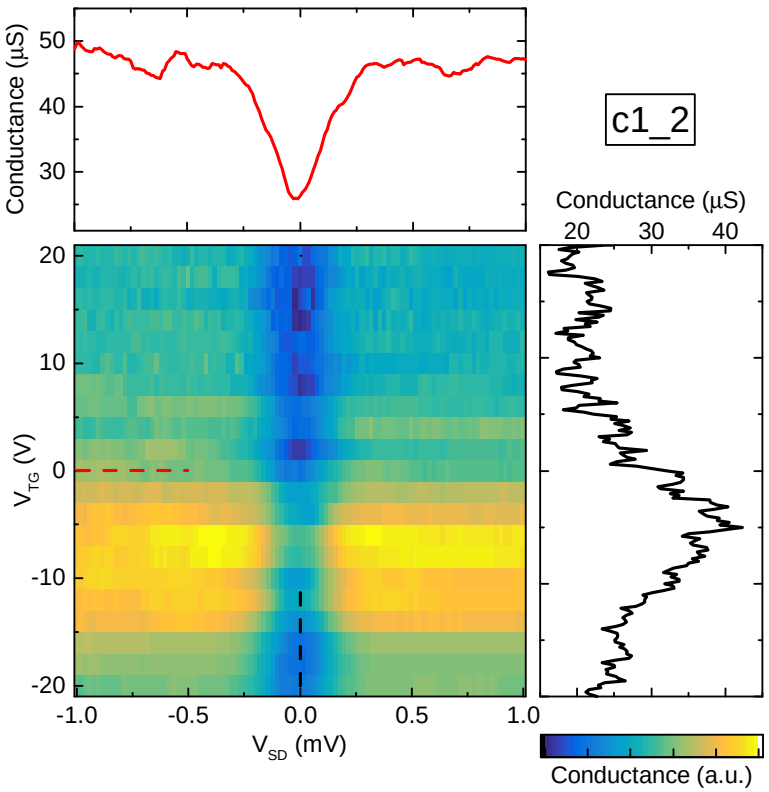

Fig. 5.8 Low temperature (T = 50 mK) measurement of two-terminal conductance against source-drain voltage bias V_{SD} and gate voltage V_{TG} on device c1_2. Behaviour is qualitatively the same as device c1_1 (see figure 5.7) but the overall conductance is much lower here. This could be due to the junction graphene being less transmitting or a worse metal-graphene interface, both of which will vary from device to device.

c1_1. The line sections at $V_{SD} = 0$ V show that in these devices the Dirac point (conductance minimum) is not accessible in a ± 20 V range, unlike in device f1, but the device conductance can be altered somewhat. The line sections at $V_{TG} = 0$ V show a soft gap feature meaning that a full proximity effect has not been achieved. The lack of a gap edge peak makes it difficult to determine its value exactly but it appears to be around 300 µV and since both source and drain are superconducting this should be $2\Delta/e$ suggesting an induced gap of around $\Delta = 150$ µeV which is similar to other work on graphene with a soft gap [61]. At the fridge temperature of 50 mK, the thermal energy $k_B T \approx 4$ µeV. This is much smaller than the apparent gap so thermal broadening alone cannot explain the observed soft gap.

The 2D plot appears symmetric about the conductance peak at $V_{TG} = -8$ V but this is not the Dirac point as a conductance dip is expected there so it is unclear what this feature is. The gap feature is less deep near this peak but appears to have a similar width in V_{SD}. This is

perhaps counter-intuitive as a higher conductance would imply higher transmission through the device and so a stronger proximity effect and larger induced gap. Since the gate mainly alters transmission in the junction this suggests that the limiting factor is low transmission across the metal-graphene interface, so even though the junction conduction increases the high contact resistance prevents a stronger proximity effect from occurring.

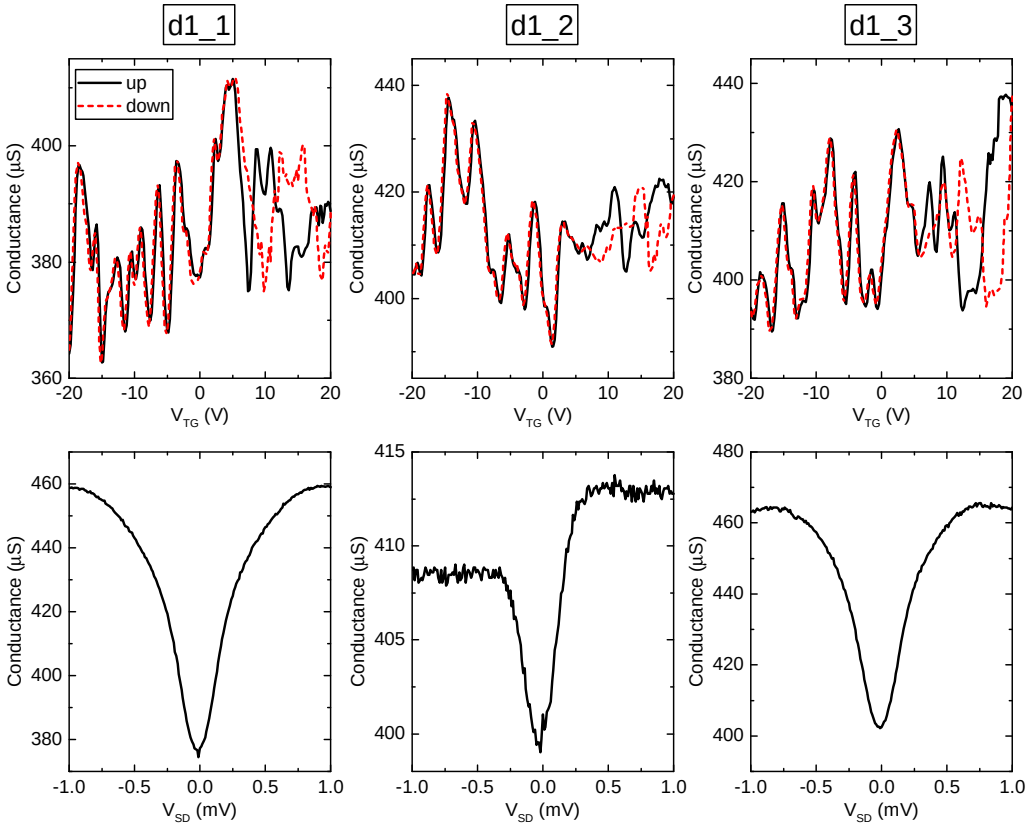

Fig. 5.9 Low temperature measurement of Device d1. (top) Gate sweeps up (solid lines) and down (dashed lines) showing reproducible conductance fluctuations over some range. There is little overall modulation of the conductance meaning the Dirac point is probably not near this gate range. (bottom) Soft gap features in source-drain bias.

Figure 5.9 shows gate and bias sweeps on three other junctions on device d1 which have a different behaviour to the c1 junctions. The soft gap feature is present as before but the gate sweeps show reproducible conductance fluctuations which become irreproducible at high positive gate voltages. Conductance fluctuations occur in diffusive systems when phase coherence is maintained over significant portions of a sample. The magnitude of fluctuations depends on how the device dimensions relate to the phase coherence length. Since these are two-terminal devices with widely varying doping and contact resistance from sample to

sample it is not possible to eliminate the contact resistance and find the true magnitude of these fluctuations, but their appearance here at least confirms that these devices are diffusive as expected and have a phase coherence length large enough to see phase coherent effects.

5.1.4 Conclusion

These low-temperature observations confirm that the contact resistance in these GJJs is too high to have a full superconducting proximity effect and so only a soft gap is seen. There are also large sample-to-sample variations in overall conductance and Dirac point position meaning the transferred graphene or following fabrication process is not completely controlled in terms of defects and impurities introduced to the graphene. In some devices conductance fluctuations are seen suggesting phase coherence over significant areas of the sample and confirming diffusive transport in the junction region. The major issue with this type of device is that each pair of materials introduces a new interface which must be understood and controlled, most importantly the graphene-metal interface for contact resistance at the junction edges and graphene-air, graphene-substrate and graphene-dielectric interfaces which affect transmission within the junction.

5.2 InAs 2DEG Josephson Junctions

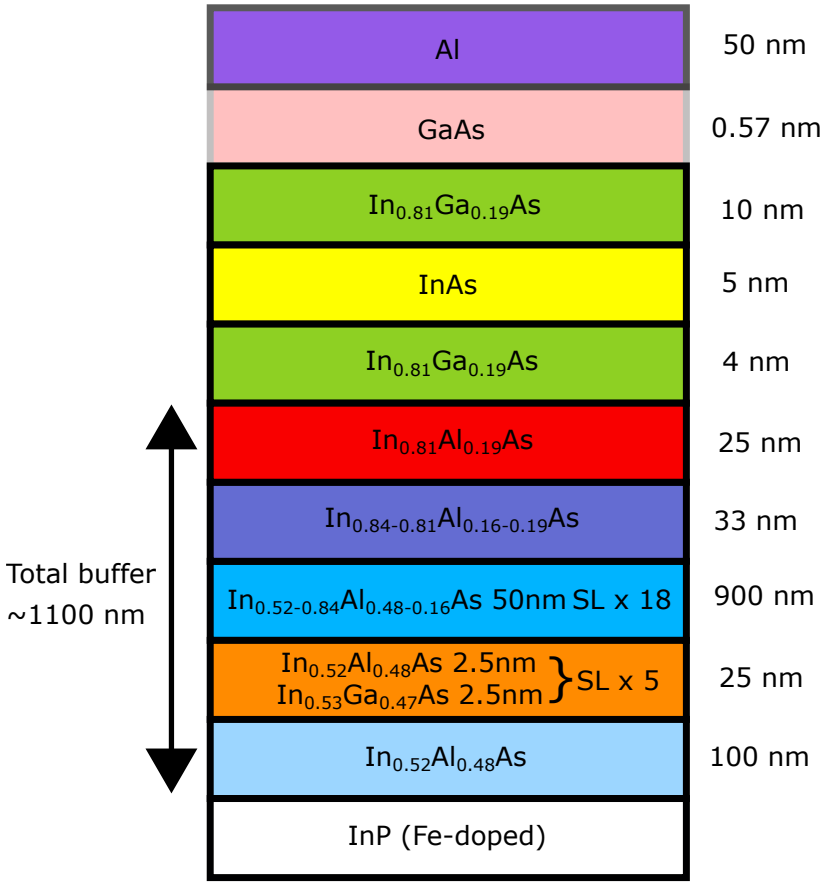

Fig. 5.10 Cross section of epitaxial Al/InAs 2DEG material on the MG3 wafer. The InGaAs-InAs-InGaAs trilayer forms the 2DEG above which is the epitaxial Al. The $\sim$ 1 µm thick buffer layer below the 2DEG matches the InAs to the InP substrate to keep the mobility high. Wafers used later had a thinner buffer layer $\sim$ 300 nm.

The above issues with the superconductor-graphene interface prompted a move to a material where the superconductor-semiconductor interface is made by controlled growth in a clean environment which would be optimal for inducing a proximity gap. One such material consists of an InAs 2DEG with Al grown epitaxially on top, producing an atomically flat interface which matches the two materials well. Figure 5.10 shows a cross section of this epi-Al/InAs 2DEG material. The InGaAs-InAs-InGaAs trilayer forms the 2DEG and the GaAs cap protects this but still allows coupling to the epitaxial Al grown above which fully proximitises the 2DEG. The buffer layer below the 2DEG relieves strain between the 2DEG and InP substrate by bridging their lattice mismatch which keeps the mobility of the 2DEG high. This material has been shown to have a highly transparent interface between the Al and InAs 2DEG producing a strong proximity effect with a hard induced gap [82, 83]. Transport

through the 2DEG is ballistic allowing quantised conductance effects to be seen in point contact devices [84] making this an ideal material to investigate Andreev bound states in the few mode regime. The material used here was grown by the Manfra Group at Purdue University and the fabrication and measurement were performed at the Center for Quantum Devices, University of Copenhagen.

5.2.1 Transport Device

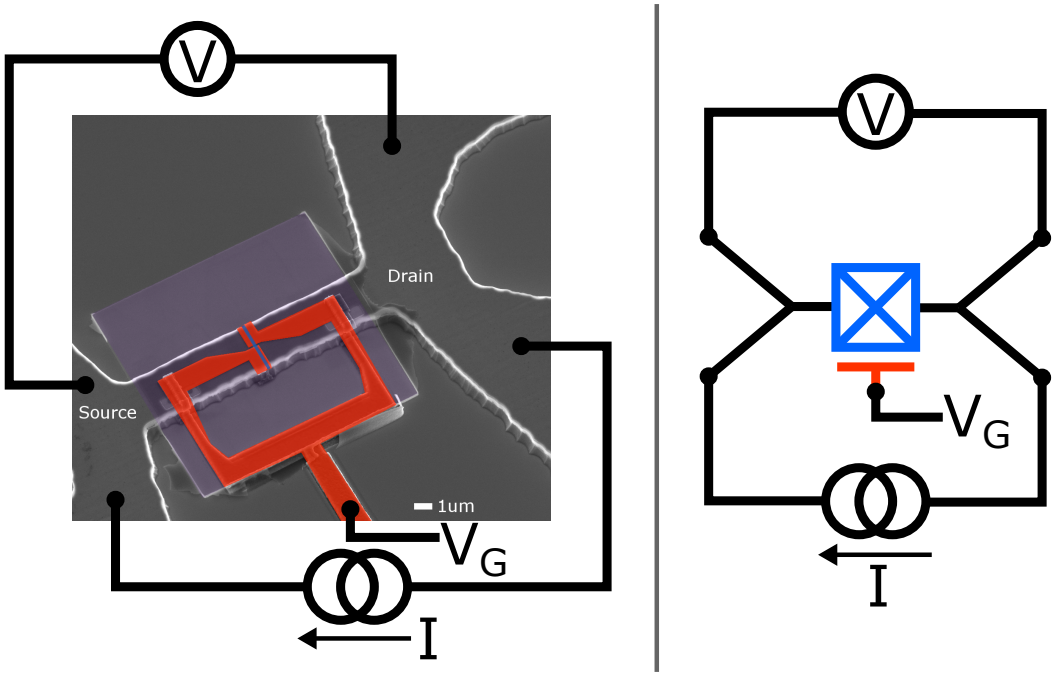

Fig. 5.11 A typical device used for transport measurements (left) with a corresponding schematic (right). The epi-Al/InAs 2DEG mesa has branched leads coming from the source and drain to allow both voltage bias measurements and 4-terminal current bias measurements where a current bias I is applied through the junction and the resulting voltage drop V is measured using the setups described in section 3.2. The epi-Al is etched away in a narrow region (blue) to define the junction and the gate (red) is deposited on top with a thin dielectric (purple) in between. The gate geometry used was either a top gate covering the whole junction or a split gate to form a QPC.

Figure 5.11 shows a typical split gate transport device on the chip MG3-ADC1. Unwanted material is etched down to the InP substrate to leave behind a mesa of the epi-Al/InAs consisting of one main rectangular transport channel with branched leads at each end. The epi-Al is etched for a short length along the channel and across the whole mesa width making a short junction of InAs 2DEG. This is the superconductor-semiconductor-superconductor

junction where Andreev bound states can form. A split gate is then deposited above the junction following a dielectric grown by ALD which is used to tune the carrier density in the junction and define a QPC. Devices were measured at a base temperature of around 20 mK using the circuits shown in section 3.2.

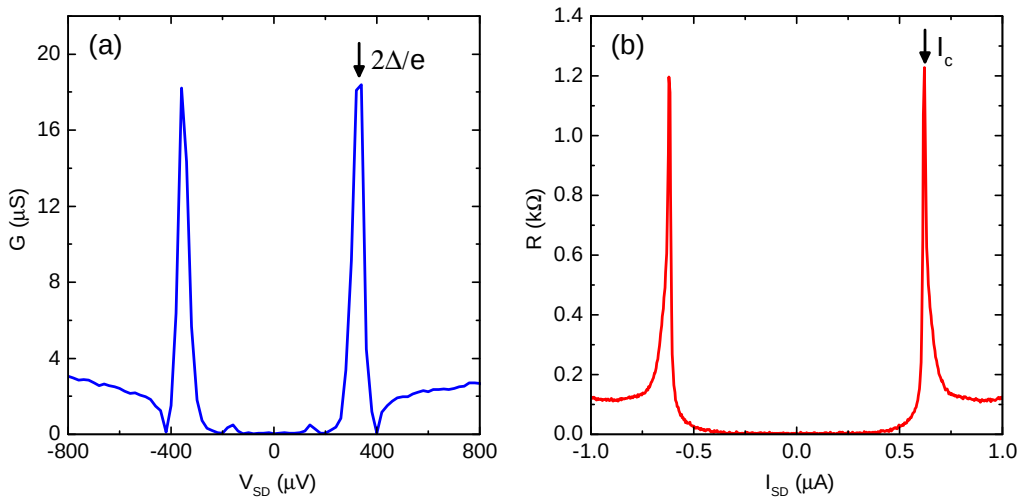

Fig. 5.12 Hard gap and critical current of device A (see figure 5.13). (a) Differential conductance G as a function of applied source-drain voltage bias V_{SD} in the tunnelling regime shows a hard gap in transport around zero bias due to a stronger proximity effect than in the graphene devices. Peaks signifying the gap edge occur at $V_{SD} = \pm 2\Delta/e$ giving $\Delta \approx 180\,\mu$eV. The smaller subgap peaks are likely due to Andreev bound states which can carry current at energies below the gap. (b) Differential resistance R with applied source-drain current bias I_{SD} shows a zero resistance supercurrent region around zero bias. Peaks either side of this region signify the start of dissipative transport and so correspond to the critical current $I_{SD} = \pm I_c$. I_c varies with gate voltage from around 600 nA down to zero at pinch off.

Measuring the device differential conductance with applied source-drain voltage bias V_{SD} in the tunnelling regime allows a transport gap to be seen in figure 5.12(a). Peaks in conductance are seen at the gap edge corresponding to a gap $\Delta \approx 180\,\mu$eV and the subgap region is mostly flat at zero conductance. Comparing to the soft gap feature in figure 5.7 it is clear that a hard gap has been induced in this device indicating a fully proximitised semiconductor. There are two small subgap conductance peaks which are likely due to transport through Andreev bound states in the junction [85].

Figure 5.12(b) shows the differential resistance of the device as a function of source-drain current bias I_{SD}. When the device is in the highly conducting open regime the critical current is high, ~ 600 nA in this case, but this can be tuned continuously to zero using the gate as will be seen later. The existence of this zero resistance region once again shows that

there is a strong enough proximity effect between the epitaxial Al and InAs 2DEG for dissipationless transport to occur through the junction and that the device fabrication process has not destroyed this. These observations show that this material and device geometry is suitable for investigating Andreev bound states in a superconductor-semiconductor junction.

5.2.2 QPC Gate Action

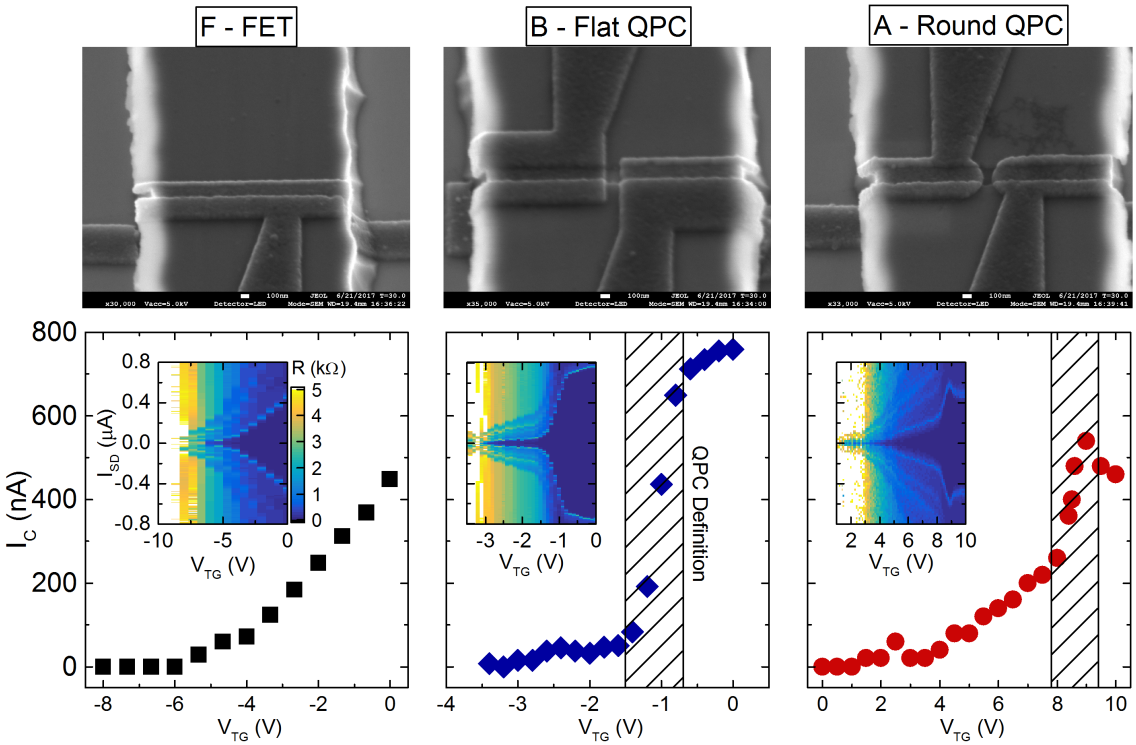

Fig. 5.13 Gate action on critical current. (top) SEMs showing an example of each gate geometry (images are not of the actual devices measured). (bottom) Critical current I_c vs gate voltage V_{TG} for each gate shape. I_c is extracted from the inset colour plots of resistance (colour scale) with bias current I_{SD} and gate voltage V_{TG} as the position of the peaks bordering the zero resistance region. F - Top gate covering the whole junction modulates I_c smoothly with only a small variation in the rate of change. B - Split gate with flat sides. QPC definition is seen around -1 V on the gate (hatched area) where I_c decreases rapidly and below this the gate laterally confines the channel reducing the number of transmitting modes towards pinch off. A - Split gate with rounded sides. Mostly the same as B at and below definition but there is a peak in I_c around $V_{TG} = 9$ V which is not seen in B. From around 3 V down to pinch off some oscillations or other finer structure in I_c are visible which may signify the few mode regime where changes in the transmissions of a small number of modes has a noticeable effect on I_c.

Reaching the few-mode regime is important for investigating individual ABS dynamics and this will depend on how well the split gate forms a QPC. The effect of three types of gate geometry on transport are compared in figure 5.13. The FET device is a simple top gate over the whole junction which when energised should nearly uniformly deplete carriers in the junction while the two types of split gate will leave a narrow region of carriers in the middle before laterally depleting them forming a QPC for ABS transport, an Andreev QPC. SEMs of each gate geometry are shown above corresponding colour plots of device resistance as a function of current bias I_{SD} and gate voltage V_{TG}. Device F (FET) shows a zero resistance region at 0 V on the gate and the edge of this region in current bias gives the critical current of the junction I_c. The critical current reduces smoothly as the gate voltage is made more negative and the zero resistance region closes completely around -7 V corresponding to complete pinch off of transport through the junction.

Device B has a large critical current at zero gate voltage which decreases slowly with negative gate voltage. Around -1 V, I_c reduces rapidly before going back to a steady decrease until pinch off. The behaviour differing from device F can be attributed to the QPC action of the split gate. Initially the junction is fully conducting so there is a large critical current but at the QPC definition point the split gate depletes carriers directly under the gate leaving only a narrow conducting channel, causing the critical current to rapidly decrease. As the gate laterally closes the narrow channel, the critical current decreases as transport modes are progressively closed until none remain at pinch off. Device A has a similar action to device B except that the critical current first increases to a maximum before decreasing rapidly at QPC definition and then the rest of the behaviour is similar to B. The split gate geometry causes differences in the fully open regime and definition of the QPC devices but their QPC pinch-off characteristics are similar suggesting that once definition has occurred they act roughly the same.

Also of note are the large differences in gate voltage range between open and pinch off for each device. Devices F and B are pinched off at negative voltages while device A is fully pinched off at zero and opens at positive voltages. The pinch off voltage for device A also varied between sweeps, sometimes being near 0 V or positive and sometimes at negative voltages, suggesting significant gate hysteresis. Device B spans the set of transport regimes in around a 4 V range while for the other devices it is around 10 V. These observations suggest that apart from the intentional differences in gate geometry, the initial doping can vary a lot between devices as can the lever arm of the gate, perhaps due to differences in dielectric quality.

In both QPC devices, close to pinch off and where the critical current is less than 200 nA, there is a range of gate voltages where the supercurrent seems to disappear and reappear until the complete pinch off point (figure 5.13 inset colour plots: ~ -3 V for device B, ~ 2 V for device A). This behaviour indicates the few-mode regime where transport varies rapidly with gate due to changes in individual mode transmissions and only a small critical currents can be maintained by the few ABS carrying current so these regions are worth investigating in greater detail.

5.2.3 Few Mode Regime

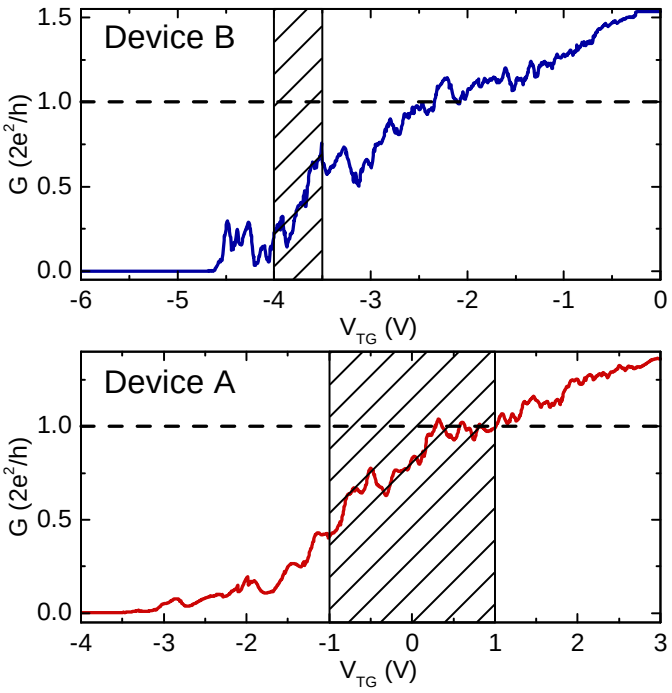

Fig. 5.14 Conductance over a large gate range for both QPC devices at high V_{SD} outside the gap giving the normal state conductance. In the normal state, $G \sim 2e^2/h$ signifies single and few mode transport and so these regions are investigated in the superconducting state. Hatched regions indicate gate range where figures 5.15 and 5.17 are taken.

Superconducting transport through a few ABSs should occur when the QPC is sufficiently narrow that only a few modes contribute to normal transport so looking at the normal state conductance can help locate the relevant range in gate. Figure 5.14 shows the conductance of devices B and A with gate voltage. The junctions are biased to a high V_{SD} outside the gap so that superconducting effects are not present and just the normal state conductance is being measured. In both devices the conductance pinch off characteristic is visible similar to the

critical current behaviour in figure 5.13 although QPC definition is not as clear here. The gate voltage for pinch off in device A is lower than before due to some gate hysteresis or drift.

A clear conductance quantisation is not seen meaning that these junctions are probably not completely ballistic. The few/single mode regime is expected when the total conductance $G \sim 2e^2/h$ which is the case here confirming that this is the relevant gate range to explore further. Higher resolution scans are taken in the indicated gate ranges and shown in figures 5.15 and 5.17 to look for any behaviour consistent with few or single mode ABS transport.

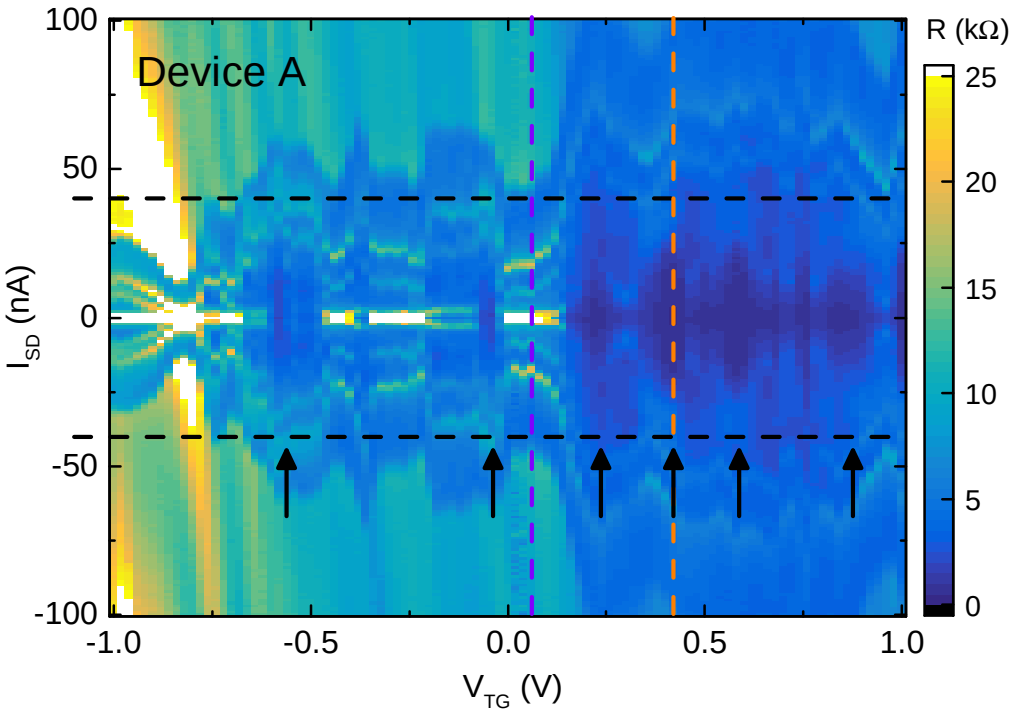

Fig. 5.15 Higher resolution scan of differential resistance on device A in potential few mode region noted in figure 5.13. Horizontal dashed lines are at ± 44 nA which is the maximum current a single ABS mode can carry for the value of Δ measured before. Arrows show areas where a low resistance region opens up which looks similar to a supercurrent region. One or multiple zero I_{SD} peaks appear in some places. Vertical dashed lines indicate positions of line sections in figure 5.16.

Looking closer at the resistance of device A in figure 5.15 shows some interesting structure. There are two main types of feature to note: (1) Regions of low resistance extended around zero bias (indicated by arrows) which open and close with gate voltage and appear mostly in the 0 – 1 V range. (2) The regions in between those containing a similarly varying envelope but also a sharp peak at zero bias which appears more often at lower gate voltages.

The low resistance 'puddles' opening and closing with gate voltage are seen in both devices A and B after QPC definition and closer to pinch off. A line section at one of the puddles is shown in 5.16(a) showing that the resistance in these regions is not exactly zero, but the shape is reminiscent of a supercurrent region with resistance peaks marking the critical current either side. When the channel is fully open with many highly transmitting modes as in figure 5.12(b) the signature of dissipationless transport is a supercurrent region which is flat at zero resistance and wide in I_{SD} due to the large critical current. It could be that in the few mode regime a lower resistance region still appears because transport occurs through ABS but since just one or a few ABS modes contribute, the minimum resistance is more sensitive to the transmissions of those modes. The supercurrent is mainly due to the most highly transmitting modes and any reflections (any $\tau < 1$) and low transmission modes lead to a non-zero resistance. From now on I assume that these regions represent a supercurrent carried by at least some of the modes in the junction and refer to them as supercurrent or supercurrent-like regions.

I_c is difficult to determine exactly since the supercurrent regions do not have sharp edges but the inner peaks (feature A) in 5.16(a), which is taken at the widest point, occur at ± 36 nA. Each Andreev bound state carries a maximum current $e\Delta/\hbar$ so using previously determined gap $\Delta/e = 180\,\mu$V this gives a maximum critical current of 44 nA per mode. If transport is ballistic the critical current would be quantised and reduce in steps of 44 nA as each mode is removed going towards pinch off but this is not observed here. Normal state conductance quantisation is not observed (figure 5.14) so it is not surprising that the critical current is not quantised either. Since the measured I_c is not too far below the maximum for one mode it appears there is either one mode with transmission slightly less than 1 or multiple modes with lower transmissions. The critical current due to a single mode is given by [33]

$$I_c(\tau) = \frac{e\Delta}{\hbar}\left(1 - \sqrt{1-\tau}\right). \tag{5.3}$$

It is not easy to tell whether the complicated modulation of I_c with gate voltage is due to modulating the transmission of just one mode or multiple modes whose contributions sum to the total I_c. If just one mode is assumed and feature A is taken as the critical current feature with value $I_c = 36$ nA, this corresponds to a mode with $\tau = 0.97$.

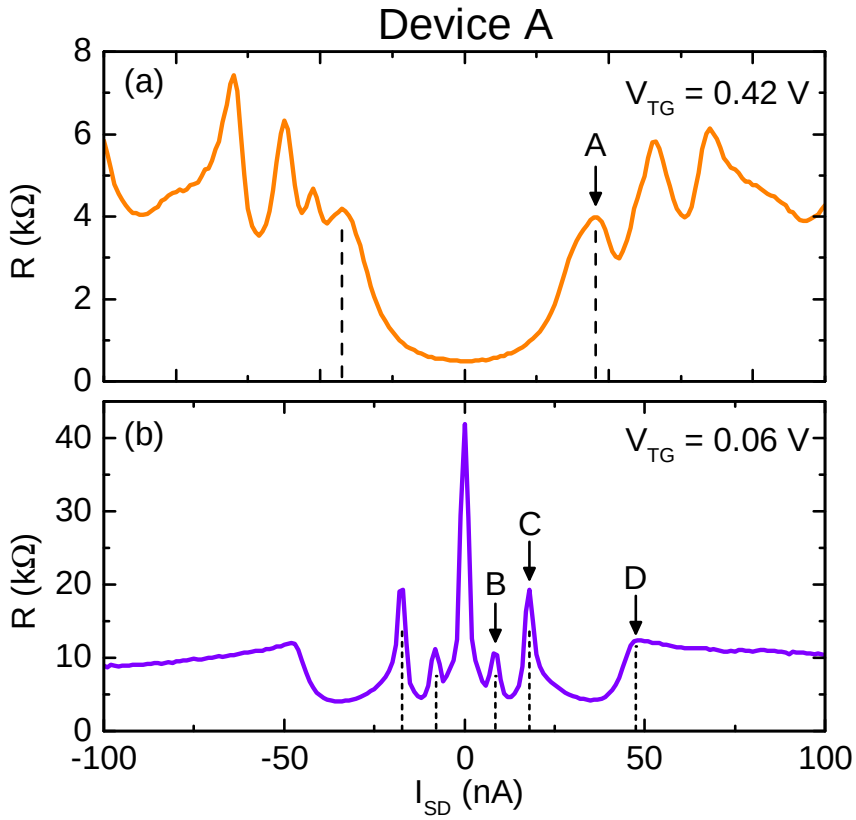

Fig. 5.16 Line sections at the indicated gate voltages in 5.15. (a) At V_{TG} = 0.42 V a region of low resistance occurs around zero bias similar to when there is a supercurrent but with the base at non-zero resistance. There are multiple peaks outside this region. (b) At V_{TG} = 0.06 V there is instead a sharp peak at zero bias and a series of other peaks nearby while the resistance is relatively featureless at higher I_{SD}. Some features of interest at positions A, B, C, D are discussed in the main text.

At other gate voltages, instead of a wide supercurrent-like region of low resistance there are one or multiple peaks centered at zero I_{SD} while the resistance is relatively featureless further out in current bias. These regions appear more frequently closer to pinch off while the supercurrent-like regions become less frequent. Figure 5.16(b) shows a line section at one of these regions containing a series of sharp peaks which are near to and symmetric about zero bias. The sharp peaks B and C and the edge of the envelope containing them (D) are indicated and looking at these in figure 5.15 they shift around smoothly with gate voltage, generally increasing and decreasing together. Following these peaks between the two line sections it appears that the peaks outside the supercurrent region in figure 5.16(a) connect smoothly to the peaks seen in 5.16(b) and their height changes as they move. So for example peak A and peak B may be the same feature but shifted in current due to gate voltage. In contrast the central peak appears and disappears abruptly near the edges of supercurrent regions and

splits into two or more peaks as it does so. This central peak being mutually exclusive with the supercurrent-like regions suggest that when the highest transmitting mode(s) become low transmission, narrowing the supercurrent region, this also causes the carriers in the junction to become localised, producing a resistance peak.

Figure 5.17 shows the resistance in (a) and the conductance in (b) in the same gate range in the few mode regime for device B. There appears to have been a slight shift in features in the time between the two measurements were taken so corresponding features do not have exactly the same gate voltage in resistance and conductance. The resistance shows a similar behaviour to figure 5.15 with three main supercurrent puddles visible (the middle one is partly obscured by the chequerboard artifact) and zero bias peaks in between. The conductance measurement in the same gate range contains broad peaks of high conductance corresponding to the supercurrent regions in resistance. Line sections through one of these in both resistance and conductance are labelled labelled P and shown in figure 5.18 where the conductance and resistance appear like mirror images of each other with the low resistance supercurrent-like region corresponding to a broad high conductance peak. A broad peaked conductance around $V_{SD} = 0\,\mathrm{V}$ is seen in other epi-Al/InAs devices in the one mode regime [84]. As opposed to the result for a normal QPC (equation (2.7)) the conductance of an Andreev QPC with one mode is given by $G = 2G_0[\tau/(2-\tau)]^2$ [35] and so will be $2G_0$ in the ideal case $\tau = 1$ but here it is at most $1.4G_0$. A single mode of transmission $\tau \approx 0.92$ would give this conductance suggesting again that the modes are quasi-ballistic in these devices.

Regions in figure 5.17(a) with a sharp zero bias resistance peak are accompanied by a zero bias peak in conductance as well as shown in the line section Q in figure 5.18. The conductance exhibits several peaks and dips, many of which do not appear in resistance. These could for example be multiple Andreev reflections (MAR) which generally appear as peaks in conductance below a voltage bias $2\Delta/e$ (see section 2.2.4) but with highly transmitting modes they can also appear as dips in conductance [83].

A full explanation of the complicated behaviour that these devices exhibit is not obvious here and there are some unexplained features such the origin of the central peak splitting before disappearing. However the overall picture given by these observations is that in the few mode regime transport is highly sensitive to the transmissions of those few modes. As the gate voltage is swept these transmissions are varied in a complicated manner which can lead to various transport phenomena depending on the exact configuration of mode transmissions.

5.2.4 Conclusion

The epi-Al/InAs 2DEG material has a hard gap and a supercurrent making it ideal for investigating ABS transport. Measurements on top-gate FET and split-gate QPC devices show that the critical current can be gate controlled over a wide range. Definition of the QPCs followed by confinement of the modes within is seen in the critical current behaviour.

After definition signatures of few ABS transport are seen such as opening and closing low resistance regions around zero bias which appear similar to a supercurrent region with a critical current slightly less than the predicted value for a single ballistic mode, 44 nA. In conductance broad peaks are seen at the same positions in gate voltage as the supercurrent regions which is consistent with the one or few mode regime, although the peak height is less than $2G_0$. At other points sharp peaks are seen close to zero bias perhaps due to some resonant transport behaviour such as MAR. The origin of these features is not fully explained here but they indicate transport through a few Andreev bound states which transition through various transport regimes and processes as their transmissions are modulated by the gate voltage.

ABS transmissions go up to $\tau \approx 0.92$ – 0.97 which are high but not fully ballistic. ABS with transmissions this high will have a minimum energy splitting corresponding to frequencies ~ 10 GHz which can be accessed by superconducting microwave resonators and so these ABS could potentially be controlled and measured at high frequency using circuit QED.

Further refinement of the fabrication or device structure may improve transmission through the device so that the transport is fully ballistic and conductance / critical current quantisation could be seen but the present devices contain at least quasi-ballistic modes. These transport measurements show that the epi-Al/InAs 2DEG is a suitable system for investigating Andreev bound states since there is a strong proximity effect and the few mode regime with highly transmitting modes can be accessed in Andreev QPC devices.

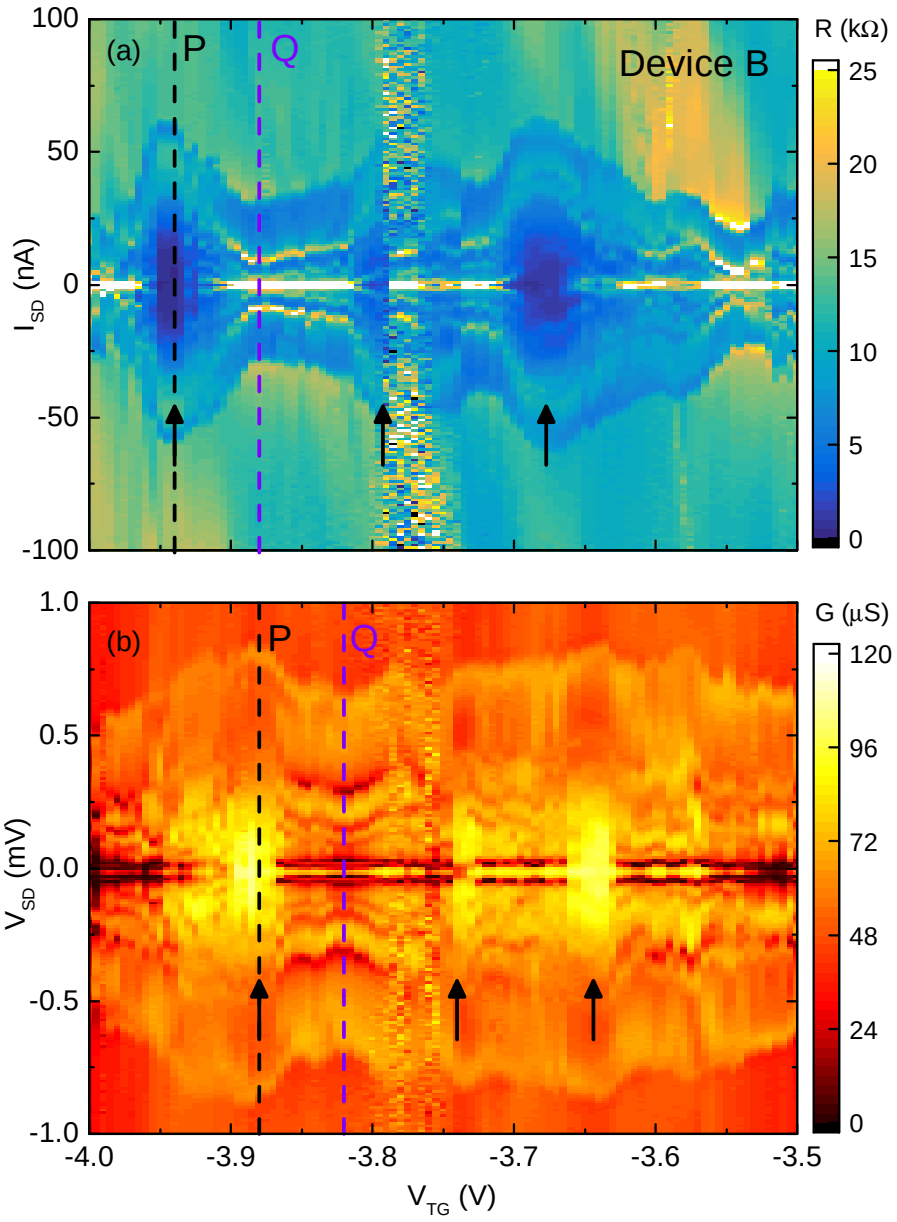

Fig. 5.17 Few mode regime for device B showing both resistance (a) and conductance (b) in the same gate range, the two plots were taken at different times so there is a slight shift of features in gate voltage. (a) The resistance plot shows a similar behaviour to device A in figure 5.15 with small supercurrent-like puddles opening and closing with gate voltage. The middle region at $V_{TG} \approx -3.8\,\mathrm{V}$ is obscured by some artifact but this appears in (b) at the same point so may be caused by some charge impurity becoming active at that gate voltage. (b) The conductance mirrors some features seen in resistance, for example the low resistance supercurrent regions appear as broad high conductance regions, however the sharp zero bias peaks in resistance appear also as zero bias peaks in conductance. Line sections at P and Q are shown in figure 5.18.

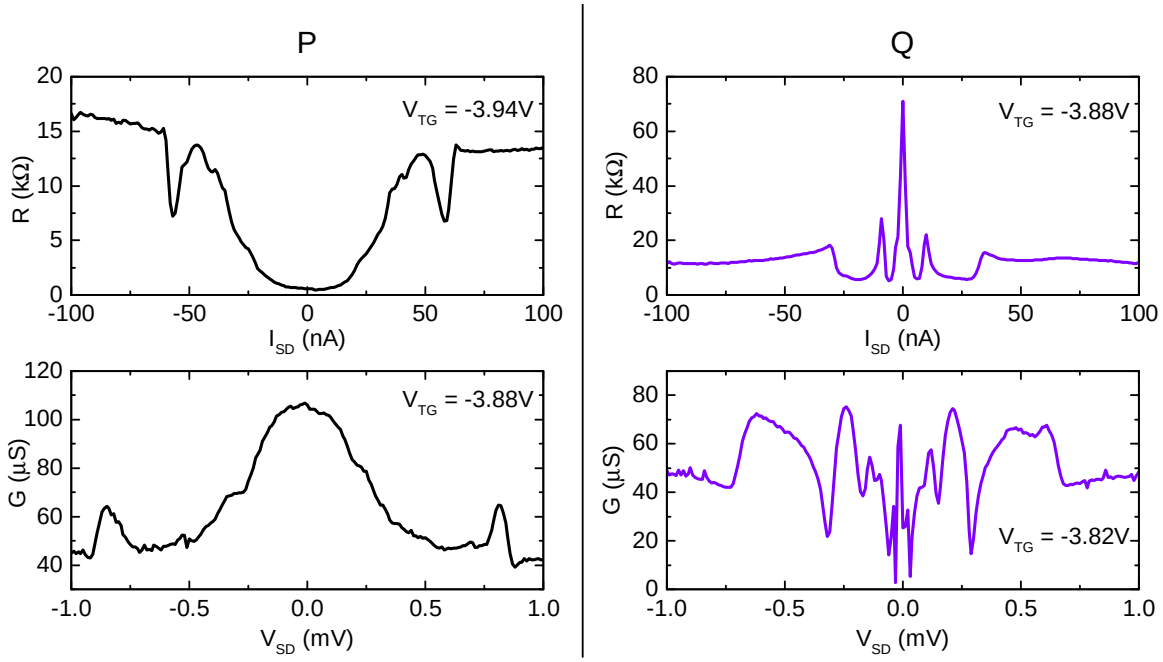

Fig. 5.18 Line sections taken from figure 5.17. P: Resistance and conductance at one of the supercurrent regions mirror each other with the dip in resistance around zero bias current appearing as a conductance peak around zero bias voltage. Q: Where there is a sharp zero bias peak in resistance there is also a zero bias peak in conductance and the two measurements do not seem to correspond in the way they do at P with many extra features in conductance that are not seen in resistance.

Chapter 6

Andreev Bound States Coupled to a Superconducting Resonator

6.1 Andreev Qubits

A single pair of Andreev bound states are a two-level system with an excitation energy which can be tuned either with the phase difference δ, via an externally applied flux Φ, or the mode transmission τ, which can be varied by a gate voltage. Using this system as a flux and gate tuneable Andreev qubit has been proposed [86] and realised in both aluminium mechanically controlled break junctions [46, 87] and proximitised InAs nanowire junctions [88]. The proximitised InAs 2DEG presents the possibility to realise an Andreev qubit in a new material system which may offer advantages to previous implementations. The 2DEG can be gated electrostatically to form and control a single Andreev mode which does not require a bendable substrate which would alter all devices on a chip at once as in the break junctions, and the 2DEG can be shaped into complicated networks with multiple junctions and connections more easily and on a larger scale than nanowire based devices. These advantages mean extending to multiple coupled Andreev qubits or other superconducting networks incorporating super-semi Josephson junctions may be more easily achievable on this material. Therefore it is useful to understand the ABS properties in the material and how they may affect their operation in an Andreev qubit.

To achieve an Andreev qubit, coupling of Andreev bound states to external control and readout systems must be demonstrated. Flux and gate control can tune the ABS excitation

energy while microwave signals are required to excite and prepare superpositions of the two levels. The devices presented here were made on the same two-dimensional electron gas (2DEG) proximitised by a superconductor introduced in section 5.2. Using standard fabrication techniques devices were made consisting of super-semi Josephson junctions with a QPC split gate (Andreev QPC) similar to those measured before. In these devices the Andreev QPC is incorporated into a superconducting loop through which an external flux can be threaded to apply a phase bias across the junction. Placing the loop near a superconducting coplanar waveguide resonator produces an inductive coupling between them. With a strong enough coupling between the ABS and superconducting resonator the ABS state can be read out by measuring changes in the resonator resonance frequency.

Two device types were measured: the Hybrid device where the Andreev QPC has source/drain leads and the Isolated device which does not. Both microwave spectroscopy and transport can be performed on the hybrid device allowing comparison of features seen in either. The isolated device can only be measured using microwaves but removal of the leads results in a higher quality resonator and lower relaxation making it useful for focusing on the ABS - resonator interaction. Measurements were performed in the dilution fridge setup shown in figure 3.11 at a base temperature of around 20 mK.

6.2 Andreev QPC Hybrid Device

Figure 6.1 shows the main elements of the hybrid device. A schematic of the device is presented in figure 6.1(a) with colours corresponding to the optical micrograph figure 6.1(b) showing the 2DEG mesa loop (orange) connected to source-drain contacts (green) and placed near a superconducting quarter wave resonator (blue). Also visible are connections for gates corresponding to the four Josephson junctions present on the device. The SEM images 6.1(c) and (d) show a closer view of the mesa loop with the junctions and gates visible. The mesa material layer structure is shown in figure 6.1(e) on which junctions are formed by etching the epitaxial Al layer of the mesa away which can then be top-gated through a 7 nm HfO_2 dielectric deposited by ALD.

The left (L) and right (R) junctions span the width of the mesa but outside the loop meaning their top-gate voltages V_L and V_R control the connection of the loop to the source and drain contacts. The loop junction spans the mesa inside the loop which allows current to flow around the loop when it is conducting and breaks the loop when pinched off using its top-gate

voltage V_{LOOP}. The small junction in the loop has a split-gate V_{QPC} (red region in 6.1(d) and (e)) which depletes the 2DEG from the edges of the mesa inwards allowing a channel of variable size to be defined. Such a quantum point contact (QPC) is used to vary the number of modes in the channel that contribute to transport and reach the few-mode regime. The QPC junction is placed at a constriction in the mesa width mainly to facilitate reaching a few transmitting modes, but also ensures that it has a low critical current and so high inductance compared to the loop junction which is placed at a widened mesa section. This ensures that any phase bias around the loop due to an externally applied flux is mostly dropped across the QPC junction since the ABS in this junction are of interest here.

Different measurement modes are possible using this network of junctions and gates:

(1) Pinching off the L and R junctions but leaving the loop junction fully conducting blocks DC transport from S to D but allows current to flow around the loop. Above the mesa loop is the meandered quarter-wave superconducting resonator which couples to the loop via the mutual inductance M and is therefore sensitive to currents in the loop. The resonator is itself coupled capacitively to a feedline and its response is measured using a vector network analyser (VNA) to measure transmission ($S21$) through the feedline. Microwave (MW) frequency power entering the resonator near its resonance frequency (typically $\sim$6 GHz) will have a reduced power transmission through the feedline and result in a dip in $S21$. Changes in the current flow around the mesa loop will change the load on the resonator resulting in a shift of the resonance dip in frequency which can be detected by the VNA measurement.

(2) By pinching off the loop junction but leaving L and R fully conducting, a current can flow from S to D but not around the loop so there is no coupling to the resonator. This mode allows two-terminal DC transport measurement of the QPC junction. The source (S) and drain (D) connections are used to perform DC two-terminal resistance measurements using a lock-in amplifier. A current bias is applied through the same connections to gain information about the critical current.

(3) Leaving L and R fully conducting and the loop junction partially conducting produces an asymmetric SQUID consisting of the loop and QPC junctions. The SQUID critical current can be modified by changing V_{LOOP} and V_{QPC} and measured by DC transport from S to D. Microwave measurement is in principle possible in this mode but the coupling to the DC leads appears to act as a large enough resistive impedance that MW signals are attenuated too much to see the resonator resonance. Only DC transport of the asymmetric SQUID is performed.

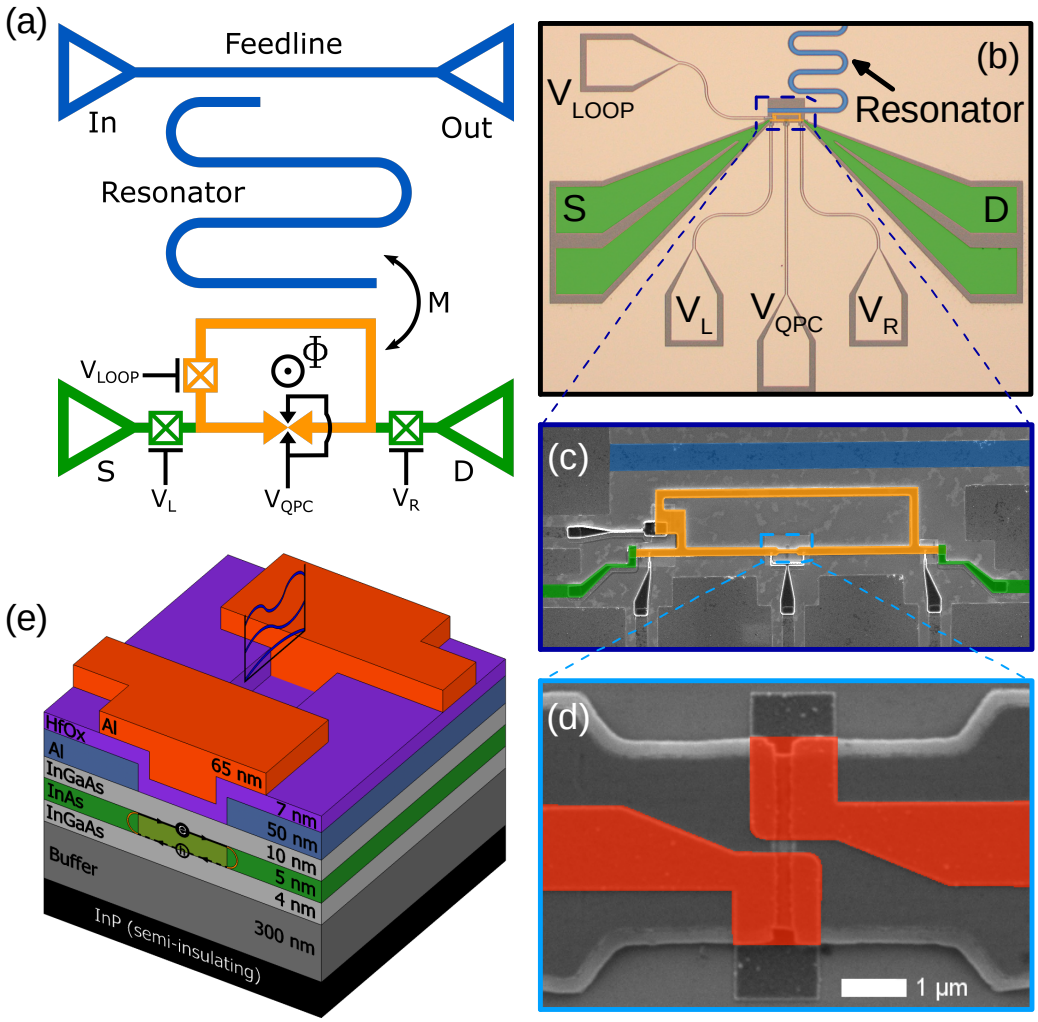

Fig. 6.1 (a) Circuit schematic of device. The main loop has a large Josephson junction (JJ) to break or connect the loop using a voltage V_{LOOP} and a smaller JJ which is split-gated (V_{QPC}) to deplete the junction and reach the few ABS mode regime. An external flux Φ can be applied through the loop. The source (S) and drain (D) leads each have a JJ on them for gate control of the connections to the DC transport circuit using $V_{L/R}$. The loop is also coupled by mutual inductance M to a quarter wave superconducting resonator which is in turn coupled to a feedline for microwave readout. (b,c) Optical micrograph and SEM image of the hybrid device with 2DEG mesa loop (orange), quarter wave resonator (blue) and source-drain leads (green) highlighted. (d) Zoom of QPC gated junction showing the split gate (red). (e) The mesa material is an InAs 2DEG proximitized by epitaxial Al. The Al can be selectively etched away to form JJs which can be top-gated via a dielectric.

6.2.1 Comparison of Microwave and Transport Measurements

Measurements from the different measurement modes 1, 2, 3 described above are shown in figure 6.2. In figure 6.2(a) the L/R junctions are pinched off but the loop junction is fully conducting so it is in mode 1 and the magnitude of $S21$ is shown as a function of applied flux and MW frequency relative to the resonance frequency $f_0 \approx 5.916$ GHz. The resonance can be fitted by a Lorentzian line shape at zero flux to obtain a quality factor of Q $\sim$ 3500 which is comparable to previous devices on the same material [89]. The resonance dip shifts down by around 1 MHz when sweeping from zero flux to half of the flux quantum (Φ_0) which is a half-period in flux. Figure 6.2(b) shows the device resistance when the L/R junctions are also opened to allow source-drain transport (mode 3), measured over the same flux range as 6.2(a) and against current bias I_{SD}. The bright peaks away from zero bias which modulate with flux appear at the critical current of the SQUID formed by the two junctions in the loop. The positive and negative critical currents are not mirror images of each other in current but are instead related by an inversion in both flux and current bias. This can occur if the geometric inductance of the loop is significant, but the device geometry was designed such that the junction inductances should be much higher than the geometric part. Therefore, this asymmetry is likely due to the non-sinusoidal current-phase relations of the junctions making up the SQUID, a result of quasi-ballistic transport through the junctions. The symmetry point in flux is $\Phi_0/2$, the same point in 6.2(a) where the resonance frequency was most shifted. There appear to be abrupt jumps in the critical current near $\Phi_0/2$ which are discussed further in figure 6.4. The flux independent peaks near zero I_{SD} are caused by the critical currents of the L/R junctions since they are always in series with the SQUID, however they are easy to keep track of and separated from the critical currents of interest as they are not affected by flux or the relevant gate voltages.

Figure 6.2(c) shows the MW transmission against QPC gate voltage V_{QPC} in measurement mode 1. As negative gate voltage is applied the resonance frequency shifts up continuously until it saturates at around -1.2 V. Small fluctuations in frequency are visible as the average resonance frequency shifts and these fluctuations disappear when the frequency saturates. Both the frequency shift and fluctuations can be attributed to the number of Andreev bound states in the junction and how the gate voltage modulates their individual transmission values which in a quasi-ballistic system can fluctuate rapidly in gate voltage as seen previously in the Andreev QPC device transport (see section 5.2.3). This interpretation is discussed further in the isolated device data. Previous work on break junction atomic contacts also show a shift in resonance frequency when reducing the size of the contact [90] however there are

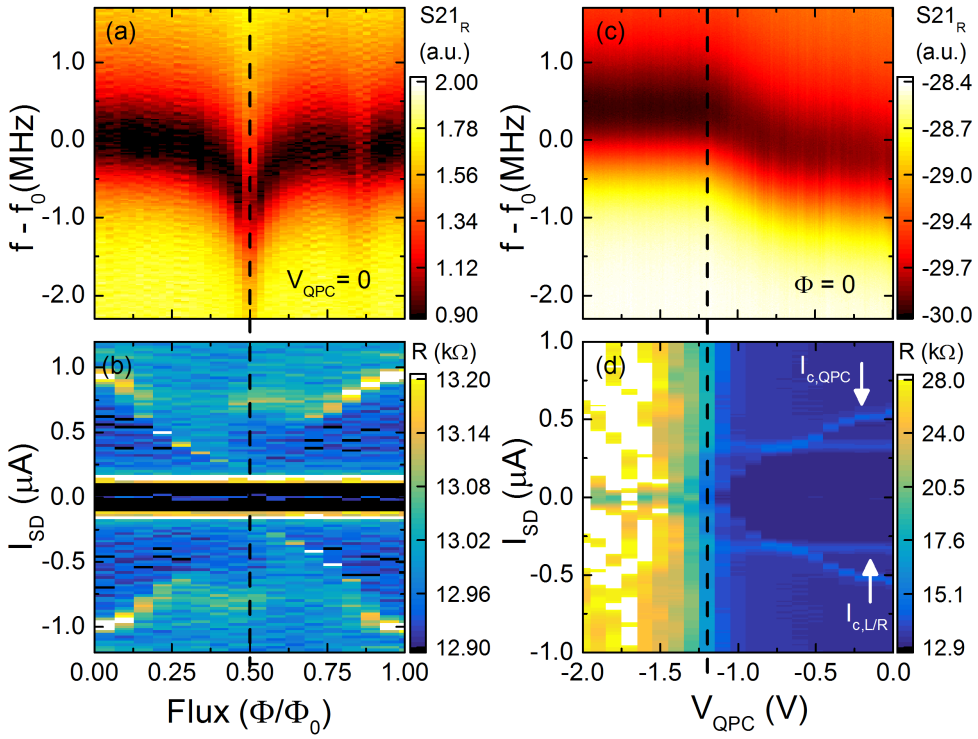

Fig. 6.2 (a) Microwave frequency transmission of feedline ($S21$) as a function of applied flux at zero QPC gate voltage showing drop in transmission at resonator frequency. The resonance frequency shifts most when approaching half of the flux quantum. (b) Two-terminal resistance as a function of flux at zero QPC gate voltage. (c) $S21$ vs applied QPC gate voltage at zero flux. Frequency shifts continuously at first before saturating around $-1.2\,\mathrm{V}$. (d) Two-terminal resistance as a function of gate voltage at zero flux. In (b) and (d) the critical current which stays constant $I_{c,L/R}$ is due to the L/R junctions which are in series with the QPC junction. The critical current peak which shifts in a corresponding way to the $S21$ frequency shift in (a) and (c) is the SQUID critical current in (b) and QPC critical current ($I_{c,QPC}$) in (d).

a few key differences to our measurements. The frequency shift in our device is positive and shifts smoothly as the QPC is narrowed while in the break junction it is negative and there is a clear jump as the contact breaks. Part of the overall frequency shift in the break junction devices is due to elongation of the resonator as the contact is broken and reformed by stretching the whole substrate, this effect is not present in our device due to the local QPC gate being used to form and control the conduction channel size so the whole frequency shift is attributable to changes in the QPC junction. The gate voltage in our device continuously tunes the carrier density and channel size in the junction and so the junction pinch-off will be a relatively smooth transition compared to the discrete breaking of an atomic contact so we do

not observe an abrupt frequency shift at pinch-off. Finally, as the junction critical current is reduced its Josephson inductance becomes large compared to the loop geometric inductance and dominates the frequency shift, and this Josephson inductance can take negative values in a range of flux around $\Phi_0/2$ and so cause a frequency shift opposite to seen in other devices.

Figure 6.2(d) shows the DC resistance against QPC gate voltage with the L/R junctions open but the loop junction pinched off (mode 2) so that only the QPC junction critical current is measured rather than the whole SQUID. The critical current starts around 500 nA at 0 V and decreases with gate voltage, approaching zero when the junction is pinched off around -1.2 V. Below this value the normal state resistance becomes very large and saturates the colour scale, but small fluctuations can still be seen especially around zero current bias. The QPC gate initially defines a transport channel and then decreases the number of modes contributing to transport by laterally confining the channel. Each transmitting mode supports an ABS pair which each contribute a fixed amount to the total critical current so as the number of modes is decreased the critical current decreases as well.

The resonance frequency shift in MW and its relation to the critical current in DC transport can be understood in terms of a simple lumped element circuit of the device shown in figure 6.3. The resonator is represented by a harmonic oscillator of inductance L and capacitance C and the QPC junction treated as a variable inductor given by its Josephson inductance L_J which is part of a loop inductively coupled to the resonator by mutual inductance M. This circuit has a resonance frequency $\omega_r = 2\pi f_r$ given by:

$$\begin{aligned} f_r &= f_0 + \Delta f \\ \Delta f &= \frac{M^2 \omega_0^2}{4\pi L_J Z_R} \end{aligned} \tag{6.1}$$

with $\omega_0 = 2\pi f_0 = \frac{1}{\sqrt{LC}}$ the bare resonance frequency and resonator impedance $Z_R = \sqrt{\frac{L}{C}}$.

This equation assumes that the typical QPC Josephson junction inductance is much larger than both the large loop junction inductance and the geometric inductance of the loop and that $\frac{M^2}{L_J L} \ll 1$ which means that the coupling is a weak perturbation to the separate resonator and QPC junction systems. Within these assumptions the resonance frequency is expected to shift as the gate voltage alters the junction inductance until the junction is eventually pinched off and its inductance stops changing, causing the resonance frequency to stay constant at lower gate voltages. Moreover due to the relationship between the Josephson inductance and critical current of a Josephson junction, this frequency shift can be connected to the

critical current changes seen in DC. The typical value of Josephson inductance in a standard Josephson junction is given by $L_J = \Phi_0/(2\pi I_c)$ so substituting this in equation (6.1) gives a linear relation between frequency shift and critical current:

$$\Delta f = \frac{M^2\omega_0^2}{2Z_R\Phi_0} I_c \tag{6.2}$$

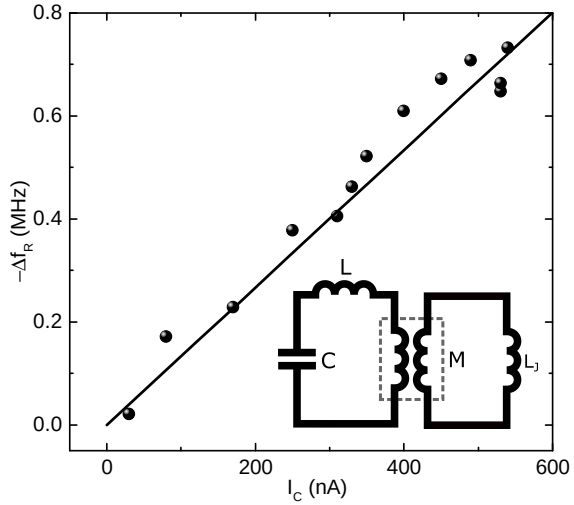

Fig. 6.3 Frequency shift from 6.2(c) plotted against critical current from 6.2(d) showing a linear relation. (inset) This relationship be explained from a simple circuit model of the system as a tuneable inductive loop coupled to a resonator and fitting to this gives a coupling inductance $M \approx 15$ - 20 pH.

The critical current and frequency shift are compared in figure 6.3 showing a linear relation and using equation (6.2) we can extract a mutual inductance $M \approx 15$ - 20 pH which is similar to the value of $M \approx 30$ pH obtained from the geometric mutual inductance of a rectangular loop next to a wire. The actual Josephson inductance of the junction will not be as simple as shown above due to the non-sinusoidal current-phase relation but using this approximate expression here gives a rough estimate of the mutual inductance M which governs the resonator – ABS coupling which agrees with the value obtained from the isolated device (section 6.3.1).

6.2.2 SQUID Critical Current and Quasiparticle Poisoning

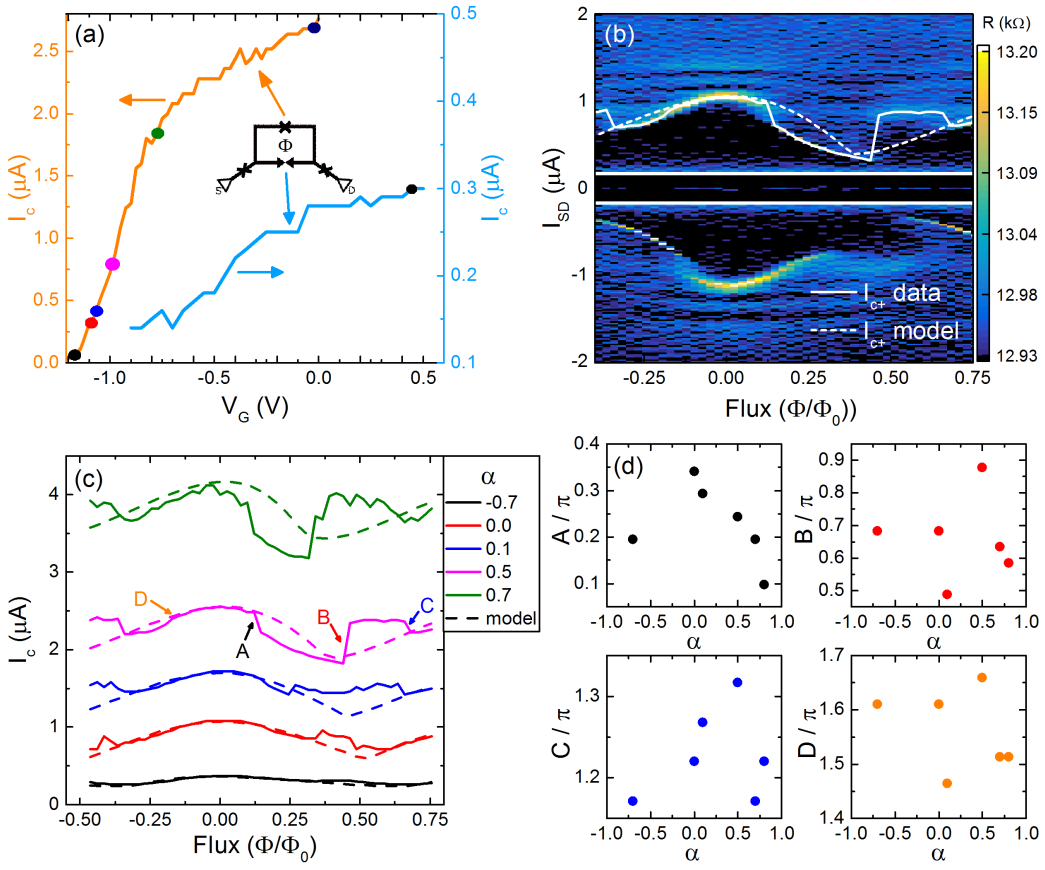

Fig. 6.4 (a) Critical current I_c of the two junctions on the SQUID arms can be tuned independently, with the loop junction spanning a larger range. (b) Two-terminal resistance in as a function of flux at SQUID asymmetry $\alpha = 0.5$ showing non-sinusoidal modulation of critical current. I_c is extracted from the data (solid line) and compared to a model using the chosen values of critical currents as inputs (dashed line). (c) I_c from data (solid lines) and model (dashed lines) for a range of asymmetries (offset from each other by 0.5 μA) showing an increase in the average value and the total modulation. Certain reproducible jump-like features labelled A,B,C,D can be seen in the data only and are at different positions with asymmetry. (d) Positions A,B,C,D extracted in (c) and plotted as a function of asymmetry. A appears to decrease away from $\alpha = 0$ while the other points B, C, D show no clear trend.

Having established the correspondence between the MW and DC measurements in the hybrid device, we now focus on features in the DC flux dependence of figure 6.2(b) to further investigate the device properties as a tuneable SQUID. SQUIDs have a total critical current related to the critical currents of the individual junctions and the flux through the loop. In traditional tunnel junction SQUIDs the asymmetry in critical current between the two junctions is fixed while those based on super-semi junctions have the possibility of tuning

this asymmetry during measurement. Tuneable SQUIDs have previously been investigated in graphene [75] where the effect of a non-sinusoidal current-phase relation is present and gates on the two graphene junctions can change the SQUID asymmetry [91, 92]. However, due to graphene being a zero-gap semiconductor these junctions cannot be fully pinched off so the asymmetry at given gate voltages must be inferred by fitting the total critical current to a numerical simulation. In our device each arm of the SQUID can be pinched off individually to measure the critical current vs gate curve of the other and so determine the asymmetry of a particular gate configuration independently of the total critical current.

Figure 6.4(a) shows this calibration measurement of the loop junction and QPC junction critical currents against their respective gate voltages. The loop junction can be tuned from 0 to around 3 µA while the QPC junction up to around 300 nA and these ranges mean a range of asymmetries can be accessed in this device. Labelling the critical currents as I_{cL} for the loop junction and I_{cQ} for the QPC junction, one can define an asymmetry parameter $\alpha = \frac{I_{cL}-I_{cQ}}{I_{cL}+I_{cQ}}$. In the following we fix I_{cQ} = 300 nA and set I_{cL} to the points indicated by the coloured dots to span a range of asymmetries.

Figure 6.4(b) shows the DC resistance as a function of flux and current bias at $\alpha = 0.5$. The critical current modulated by flux is extracted (solid line) and compared to a simple model (dashed line) of the SQUID made up of two junctions characterised by a single transmission parameter each, τ_L and τ_Q. The total SQUID current is the sum of Andreev current terms (equation (2.11)) for each junction giving a one mode version of equation (2.18):

$$I_{SQUID}(\gamma,\delta) = \frac{I_{cL}\tau_L \sin\gamma}{\sqrt{1-\tau_L \sin^2(\gamma/2)}} + \frac{I_{cQ}\tau_Q \sin\delta}{\sqrt{1-\tau_Q \sin^2(\delta/2)}} \tag{6.3}$$

where the reduced flux $\phi = \Phi/2\pi$ is related to the phase drops δ, γ across the two junctions by $\phi = \delta - \gamma$ due to flux quantisation around the superconducting loop. This expression cannot be simply factored to analytically find the critical current as in the standard case of a SQUID current made up of two sinusoidal current-phase terms so it must be calculated numerically.

In reality each junction will comprise several transmitting modes but this model assumes just one for each with the transmission coefficients $\tau_{L/Q}$ representing an effective value which captures some aspects of the distribution of transmissions over all modes present in the actual device. However this model can still provide some insight as shown in figure 6.4(c) where the critical current extracted at different values of α are plotted together. The calculated

critical current has an average value similar to the data while closely matching the data near zero flux at all values of α. The asymmetry between positive and negative critical current is also replicated well by the model (see section 2.2.5). Away from zero flux there are strong deviations from the model due to reproducible abrupt jumps in the critical current. These jumps appear to change size and position depending on asymmetry. Four distinct jump features (marked A, B, C, D) are identified and their positions in flux are plotted against asymmetry in figure 6.4(d). Point A shows a clear decrease as α is increased from zero. Since there is only one measurement at negative α it is difficult to say definitively whether this trend is monotonic or peaked about $\alpha = 0$. No clear trend is visible for B, C and D so these may behave differently to A, or perhaps the changing visibility of these jumps at different asymmetries could mean the errors in extracting them obscure any potential correlation.

The appearance of abrupt jumps in the SQUID critical current suggests a process is taking place which sharply reduces the transmission or completely removes the contribution of one or more ABS to the total critical current. Similar abrupt changes in critical current are seen by others in fixed asymmetry SQUIDs [33, 93] and attributed to quasiparticle poisoning. Quasiparticle poisoning occurs when a single quasiparticle enters the system and 'poisons' one of the ABS modes. The ABS states which can carry current $\{|-\rangle, |+\rangle\}$ both have even parity and exciting between them takes a pair of particles but if a single particle becomes trapped in the ABS the parity becomes odd. These two odd states (corresponding to spin up and down of the extra quasiparticle) do not carry current and so the current contribution of a poisoned mode will drop to zero, reducing the overall critical current.

If the poisoning process occurs at a particular energy then when an ABS crosses through this energy a quasiparticle transfer is expected which will either poison an even state or un-poison an odd state. A possible process is sketched in figure 6.5(a) for some energy E_1. If there are two ABS modes in the junction with different transmissions, their energies will cross through E_1 at different values of phase giving 4 different points (A, B, C, D) in each period where a poisoning/unpoisoning event will occur. Below are three example critical current curves corresponding to no poisoning (yellow), 1 mode poisoned (orange) and 2 modes poisoned (red). The case with both modes poisoned is not just zero since there will still be a contribution from the other junction in the SQUID. The black curve shows the critical current of the system assuming poisoning events at A and B and unpoisoning at C and D, giving 4 jumps in critical current as seen in figure 6.4.

Figure 6.5(b) shows the same process at a different energy E_2 and the critical current curves are overlaid in (c) showing that depending on the energy chosen the positions and height

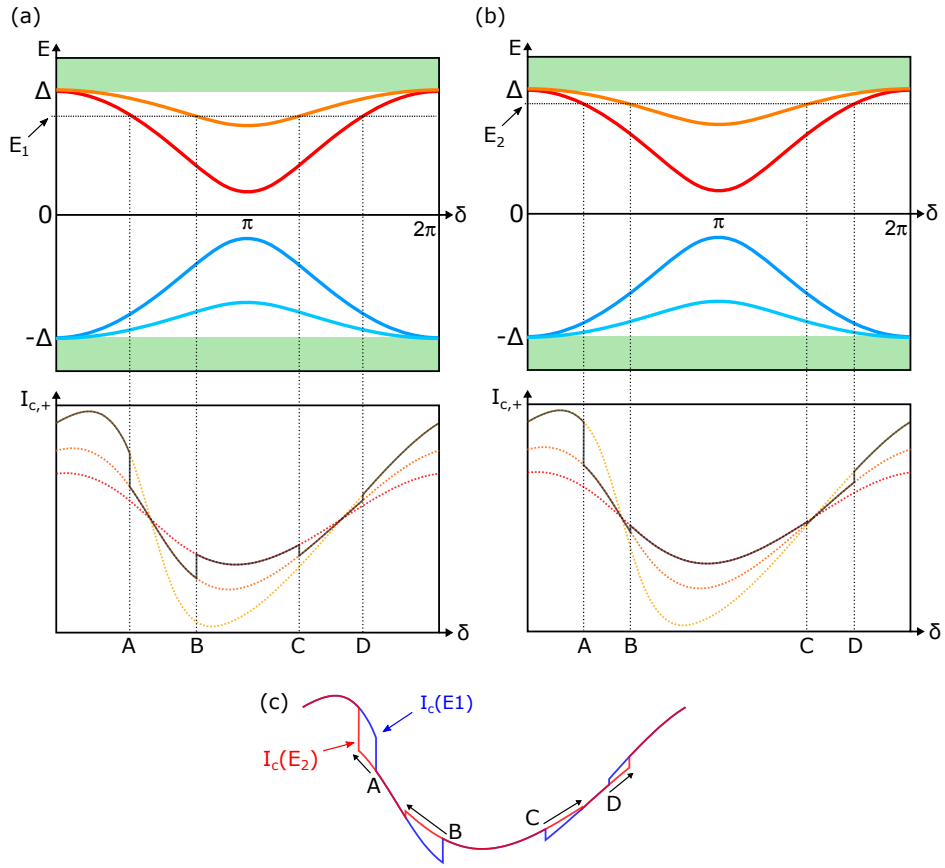

Fig. 6.5 Sketch of quasiparticle poisoning effect on critical current. (a,b) The top panels show energies of two ABSs with different transmissions. Assuming quasiparticle transfer into or out of the junction occurs at a particular energy, each mode will be poisoned or un-poisoned when their energy crosses it. Two example energies labelled E_1 and E_2 are shown and below the corresponding effect on the SQUID critical current is sketched. As each mode becomes poisoned or un-poisoned at the intersection points (A, B, C, D) the critical current jumps between the three curves producing a structure similar to the measured I_c. (c) The two resulting critical currents overlaid showing that the position and height of jumps can vary greatly depending on the exact configuration of modes and poisoning energy.

of each jump can change so some jumps will be more visible than others. Although the most clear change in jump position in figure 6.4(d) is seen for point A, from figure 6.4(c) it can be seen that the height and position of the jumps do in general change with SQUID asymmetry. The exact reason for this is not clear but considering extremes of asymmetry can provide some insight. When the asymmetry is very high ($|\alpha| \gg 1$ the phase across the high I_c junction is nearly constant and most of the phase change occurs across the smaller I_c junction. Conversely in the symmetric case $\alpha \approx 0$ the phase drops across each junction are nearly equal. So one effect of asymmetry is changing how much of the total phase is

dropped across each junction in the SQUID, and therefore altering the asymmetry will shift the positions of jumps in phase.

Operating the hybrid device as a SQUID with independently tuneable arms allows a range of asymmetries to be accessed over which the critical current varies from $\sim 300\,\text{nA}$ to $\sim 4\,\mu\text{A}$. The non-sinusoidal nature of the underlying current-phase relations is seen in the SQUID critical current. Jumps in the critical current are attributed to quasiparticle poisoning which may be present due to coupling quasiparticle reservoirs such as the leads or some part of the semiconductor stack such as the buffer layer.

6.3 Isolated Device

Relaxation and dephasing mechanisms such as quasiparticle poisoning and charge noise will reduce the lifetime of states prepared in Andreev two-level systems in the proximitised 2DEG material. This will affect its viability for making long lifetime qubits or other elements in quantum circuits which must remain coherent. The relaxation rate of Andreev two-level systems can in principle be investigated via their interaction with the resonator in the MW measurement mode of the hybrid device, however there are some confounding factors which complicate what is being measured. The source-drain leads which are made of 2DEG material and are coupled to the outside world can act as quasiparticle reservoirs which are still weakly tunnel coupled to the loop when the L/R junctions are closed off as well as appearing as a capacitively coupled load to the resonator. The loop junction contains many high-τ Andreev two-level systems when fully conducting and although it's inductance is small it still reduces the phase dropped across the QPC junction slightly and makes the loop a highly asymmetric SQUID rather than the desired setup of a single small junction in an otherwise superconducting loop. Therefore we move to the Isolated device shown at the bottom of figure 6.6, consisting of a loop interrupted by one junction which is gated by a QPC split-gate.

The loop is only coupled to the resonator so only the MW measurement mode is possible, but this simpler device provides a higher quality MW measurement which can be seen in figure 6.6(a) where the flux response of the feedline transmission is shown. The resonator itself has a higher quality factor $Q \sim 5000$ and the shift in frequency at $\Phi_0/2$ is larger, $\sim$3.5 MHz compared to $\sim$1 MHz in the hybrid device. The frequency shift with flux is extracted in figure 6.6(b) and compared to the functional form of the Andreev – resonator coupling g and $g^2/\Delta\omega$

where $\Delta\omega = \omega_r - \omega_A$ is the Andreev – resonator detuning for Andreev bound state splitting frequency $\omega_A = 2E_A/\hbar$. The term $g^2/\Delta\omega$ is the resonator frequency shift given by the Jaynes-Cummings model of coupling between a resonator and two-level system in the dispersive limit $|\Delta\omega| \gg g$ [43]. The shape of the resonator shift is more closely fit by the coupling g using plausible fitting parameters consistent with the gap seen in other experiments [88] (induced superconducting gap $2\Delta = 60$ GHz, g: $\tau = 0.990$, $g^2/\Delta\omega$: $\tau = 0.892$) suggesting that this shift is not due to a dispersive Jaynes-Cummings-type interaction but directly proportional to the coupling which appears in the Andreev - resonator Hamiltonian (see equation (2.28)).

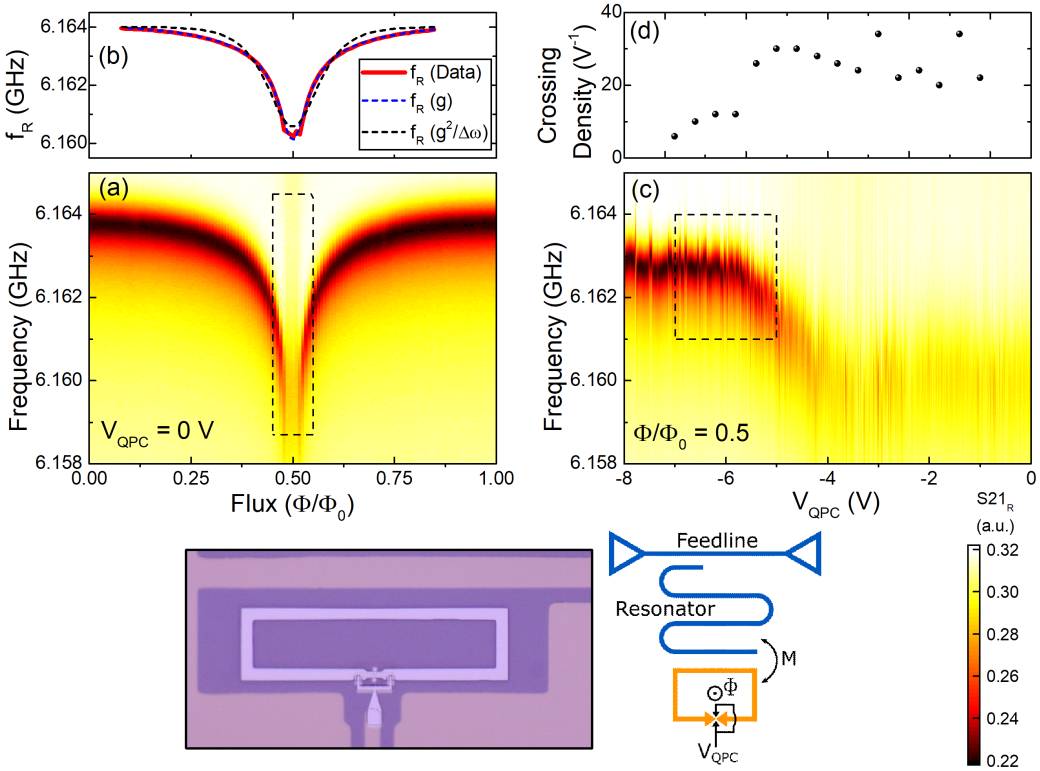

Fig. 6.6 (below) Isolated device optical image and circuit schematic. This device has the resonator measurement circuit but no source-drain leads. (a) $S21$ with applied flux showing frequency shift at half-flux quantum as in the hybrid device. (b) Resonance frequency extracted from (a) with fits to the functional form of the coupling g (equation (2.29)) and dispersive shift $g^2/\Delta\omega$ showing the fit to g is better. (c) $S21$ with gate voltage showing overall shift and saturation of resonance frequency as in the hybrid device but rapid fluctuations in frequency are also visible which become less rapid as the gate voltage goes more negative. These can be associated with individual ABS crossing near or through the resonator in frequency. (d) Density of fluctuations is extracted from (c) as the number of crossing events per volt and plotted at 0.5 V intervals showing a jump down around -6 V, which is also where the resonance frequency saturates in (c).

Figure 6.6(c) shows the QPC gate response of MW transmission which has a similar form to figure 6.2(c) with the resonance frequency shifting up with more negative gate voltage and small fluctuations around this overall shift. Here the shift and fluctuations are more pronounced than before revealing that the fluctuations do not stop abruptly but seem to decrease in density as the resonator frequency shifts and saturates. The average density of fluctuations is plotted in figure 6.6(d) showing an overall decrease with decreasing gate voltage and an abrupt drop around -6 V, suggesting QPC definition.

The number of modes at definition can be estimated using the gate capacitance from a parallel plate capacitor model and definition gate voltage. Despite having the same nominal junction length and gate dimensions, QPC definition occurs at very different voltages in the hybrid (-1 V) and isolated (-6 V) devices. This could be due to the isolated device having no DC reference to ground which is provided by the source/drain in the hybrid device so the gate action appears weaker. Therefore using the hybrid device value gives the carrier density $n \approx 5 \times 10^{12}\,\mathrm{cm}^{-2}$ and Fermi wavelength $\lambda_F \approx 11$ nm. Using equation (2.6) and the channel width ($\lesssim$ split gate gap, 250 nm) gives N = 22 modes, so this rough upper estimate gives a relatively low mode number. The few-mode regime is where the physics of individual ABS becomes important and where such a device would be operated as a qubit so we focus on this region now.

6.3.1 Few Mode Regime

In figure 6.7(a) the flux response in the indicated region of 6.6(a) is plotted with the gate voltage set in the few-mode region below -6 V. Here the resonator does not have a monotonic frequency shift either side of $\Phi_0/2$ and exhibits more detailed structure with drops in visibility where a mode crosses through and frequency shifts up or down depending on if the mode crossed from above or below the resonator in frequency. The ABS transition frequency ω_a changes smoothly with applied flux having a minimum at half the flux quantum but if there are multiple modes present with different transmission τ then they will cross the resonator at slightly different values of flux, producing the multi-lobed structure seen in the data. Figure 6.7(b) shows the gate response at flux $\Phi_0/2$ in the indicated region of 6.6(c) where the fluctuations drop in density and frequency begins to saturate – the beginning of the few-mode regime. The fluctuations are caused by individual ABS crossing through the resonator causing frequency shifts and damping the resonator as seen in 6.7(a) but here it is due to the gate voltage varying the transmission of each individual mode. Modes with high enough transmission to reach the cavity frequency when modulated by the gate will cross

occasionally so the more modes there are the higher the crossing density. However, even in the few mode regime many crossings are seen suggesting that the gate voltage modulates the τ of the remaining few modes quite rapidly. The overall shift in resonance frequency can be explained by the changing number of modes. Initially a large number of modes are present above the resonator in frequency which interact with it and push the resonance frequency down. As a more negative gate voltage is applied the conduction channel is narrowed, reducing the number of modes and reducing the overall push down of the resonator frequency. Therefore a shift up and eventual saturation of the resonator frequency occurs when approaching the few mode regime.

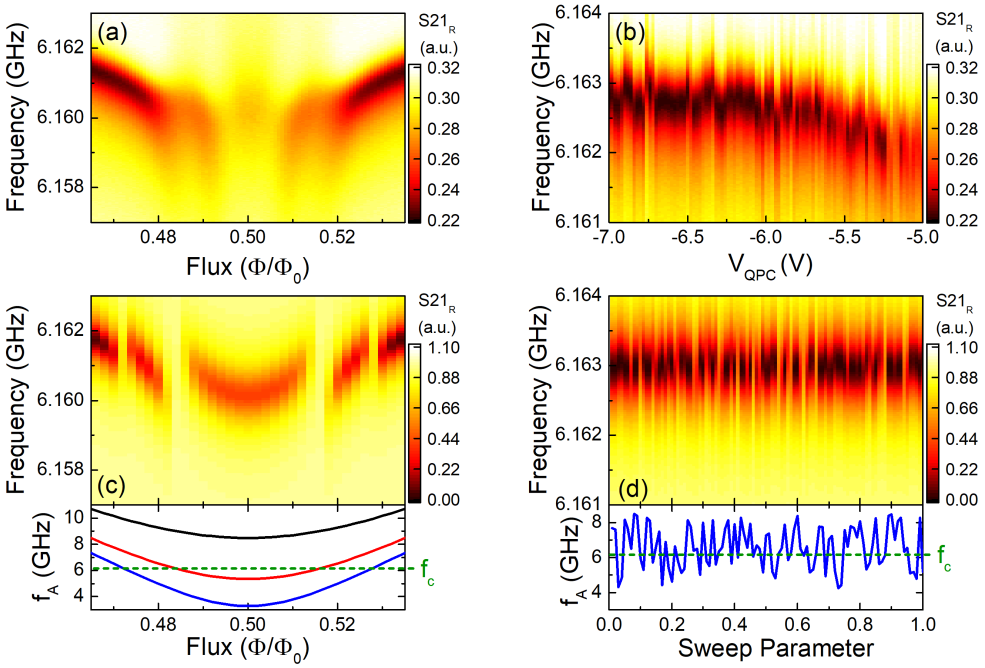

Fig. 6.7 (a,b) Device transmission vs flux/gate in region indicated in 6.6(a,c) respectively. (c,d) Calculated $S21$ from Andreev qubit Hamiltonian vs flux/gate, showing similar behaviour to the data can be produced in this model. Below are the Andreev mode spectra use to generate (c,d). For (c) three modes with different transmissions are used to achieve the observed multiple crossing features in (a). For (d) the transmission of a single mode is varied randomly to simulate the action of gate voltage on a mesoscopic semiconductor.

In order to explain these observations qualitatively and to later analyse single crossings more quantitatively we simulate the ABS – resonator system using a master equation approach coded in QuTiP [94] to calculate the resonator response. The system Hamiltonian consists of three parts $\hat{H} = \hat{H}_R + \hat{H}_A + \hat{H}_g$ for the resonator, Andreev two-level system and the interaction between them respectively and the full form of each term is outlined in section 2.3. The

coupling g shown in equation (2.29) is of particular importance since it governs the overall interaction strength and varies with the phase and transmission of the Andreev bound state.

In general the system dynamics are governed not just by unitary evolution according to the above Hamiltonian but incoherent relaxation of the resonator and Andreev states due to the external environment, for example the substrate, gate dielectrics and other devices coupled to the same feedline. These relaxation processes are included in the master equation method and characterised by parameters κ for resonator relaxation and γ for the Andreev system. The three tuneable parameters g, κ and γ govern the dynamics of the system and their relative values determine how long quantum states stay coherent, for example if operating as a qubit. The above model is for a single Andreev two-level system coupled to the resonator and for most of what follows this is the situation considered since we are in the few mode regime and generally only one mode will have high enough τ (low enough ω_A) to interact significantly with the resonator.

As noted above, the features in figure 6.7(a) appear to be the result of multiple modes crossing through the resonator and the model can be readily extend to multiple ABS modes by expanding the state space and introducing Andreev and coupling terms for each additional mode. Figure 6.7(c) illustrates this, showing the simulated MW transmission against flux for three Andreev modes with different τ values. The frequencies of the modes themselves are shown in the panel below (c) in which two of the modes cross through the cavity at slightly different fluxes while the third stays above. This arrangement qualitatively reproduces the multiple crossing points and overall curve of the resonator seen in 6.7(a). Figure 6.7(d) shows a single-mode simulation with the Andreev mode frequency in the panel below again. In order to capture the effect of the gate voltage on the quasi-ballistic semiconducting junction the transmission τ of the mode is varied randomly which causes the Andreev frequency to vary randomly around the resonator frequency. This reproduces the crossing features seen in figure 6.7(b) but not the overall shift in resonator frequency which could be due to a change in the average value of τ for the single mode, or more likely due to the reduction in the number of modes which are low enough in frequency to push the resonator down as the channel is narrowed. Note that the x-axis of the simulation is not gate voltage since each step in the simulation is just the next generated random value of τ. This list of τ values will relate to the gate voltage action but in an unknown way so an identification between the simulation sweep parameter and gate voltage has not been made.

The flux and gate dependence of the device can be qualitatively reproduced using few and single-mode versions of this model with values of g, κ, γ selected to improve this qualitative

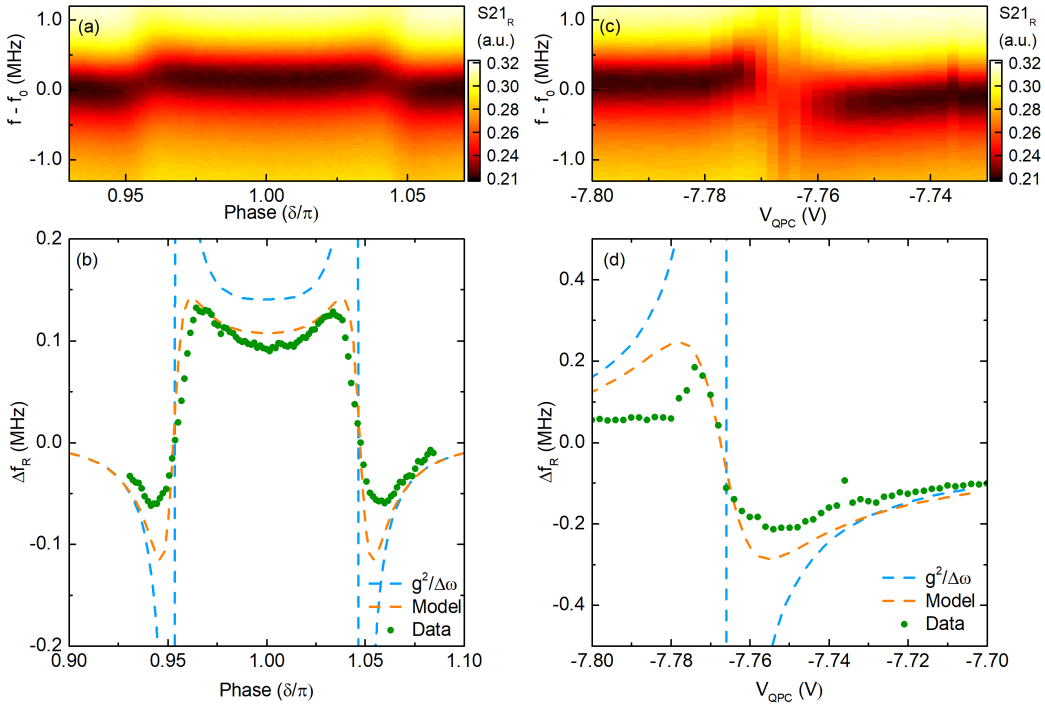

Fig. 6.8 (a) Resonator response with flux in small range around half-flux quantum ($\delta = \pi$) in the few-mode regime (gate voltage below -6 V) showing a single mode crossing through the resonator around $\delta = 0.95\pi$ and $\delta = 1.95\pi$. (b) Resonator frequency shift with flux extracted from the data in (a) and from the model, compared to what would be expected from a simple dispersive shift $g^2/\Delta\omega$. (c) Resonator response in small gate range in the few-mode regime showing a single crossing at -7.77 V. (d) Resonator frequency shift with gate from the data and model compared to the dispersive shift $g^2/\Delta\omega$. For both the flux and gate response the model more closely approximates the data showing the strong effect of ABS relaxation in our device.

agreement, however the features present in a large flux or gate voltage range may be due to more factors than can be accounted for in the model so it will be useful to focus on just a single feature caused by a single mode crossing the resonator due to gate voltage or flux. Figure 6.8 shows measurements where the gate voltage has been placed far into the few mode regime and we focus on features around or at $\Phi_0/2$. In figure 6.8(a) is the experimental transmission data showing a single mode crossing through the resonator. The flux axis has been rescaled as the phase variable $\delta = 2\pi\Phi/\Phi_0$ which appears naturally in the theory and model, so the crossings occurs around 0.95π and 1.05π with the Andreev state being below the resonator between the crossing points. Below in figure 6.8(b) the frequency shift from figure 6.8(a) is shown alongside the calculated dispersive shift $g^2/\Delta\omega$ and the frequency shift

given by the full Andreev-Resonator model including relaxation showing that the latter can much more closely fit the data. This suggests that the relaxation plays a significant role in this system and must be included to accurately capture its dynamics.

Figures 6.8(c) and (d) show the same as (a) and (b) but for a single crossing in gate voltage. In figure 6.8(c) the Andreev mode is below the resonator at $-7.80\,\mathrm{V}$ and crosses through at $-7.77\,\mathrm{V}$. The crossing does not resemble the typical avoided crossing when two modes hybridise strongly as the resonator is heavily attenuated far from the crossing and does not exhibit a clear Rabi splitting meaning that the device is not in the strong coupling regime [95]. These observations can be attributed to a low coupling and high relaxation rate as shown in 6.8(d) where the resonance frequency shift is again plotted alongside the dispersive shift and the model using the same parameters as in figure 6.8(c). The sharp jump of resonance frequency at the crossing point seen in the dispersive shift is not present in the data, which has a more gradual frequency shift that is well replicated by the model. It is worth noting that in both flux and gate the full model and dispersive shift formulas agree with each other increasingly well far away from the crossing points, suggesting that the discrepancy is specifically related to the interaction with the Andreev mode and not something which persists far from the interaction regions.

The model shows agreement with a single crossing in both flux and gate voltage using the same set of the parameters g, κ, γ. The resonator relaxation κ can be fixed using the measured Q factor of 5000 and resonance frequency $f_0 = 6.163$ GHz to give $\kappa \approx 1$ MHz. The values of g and γ were varied to improve the fit and we find $g_{max} \approx 18$ MHz and $\gamma \approx 1$ GHz. This value of g corresponds to $M = 10$ pH which is similar to but slightly lower than the value obtained previously in the hybrid device. Being able to fix κ experimentally and finding M similar to that obtained previously gives confidence in this set of values for describing the system in this device. The values of g and κ seem reasonable when comparing to previous devices, and based on device geometry, while γ appears to be anomalously high. Possible reasons for this are highlighted in the discussion below.

The Andreev state relaxation $\gamma \approx 1$ GHz obtained by comparing the data to the Andreev-Resonator model is quite high. This could be due to several factors present in this device, for example the Hybrid device SQUID experiments in section 6.2.2 show there is quasiparticle poisoning present in these super-semi junctions that causes the system to move from the even to odd state manifold of the Andreev system, which does not interact with the resonator. Additionally, there are various sources of charge noise on the device such as the gate dielectric, buffer layer and substrate which could contribute to state decoherence and relaxation. Al-

though ABS - resonator hybridisation is observed, attempting to excite the transition between ABS levels while monitoring the resonator response (two-tone spectroscopy) produces no clear signal of this transition. These considerations suggest that the ABS relaxation rate was too high to produce a visible signal before becoming poisoned or otherwise relaxing.

6.4 Conclusion

Using the Andreev qubit device structure, flux and gate control of Andreev bound states in a super-semi Josephson junction has been demonstrated. In the hybrid device, measurement of the junction properties via DC transport current and microwave response of a coupled superconducting resonator shows that the two are correlated meaning circuit QED could be used for fast measurement of ABS dynamics. Hybridisation between the resonator and ABS states is seen in the isolated device. Observing how the hybridisation evolves with gate voltage and flux shows broad shifting and damping of the cavity when there are many modes while individual modes crossing the resonator frequency can be seen in the few mode regime.

The ABS-resonator coupling in this system is much lower than the apparent relaxation rate obtained from a model meaning a clear Rabi splitting was not visible and so the individual states of the ABS two-level system cannot be distinguished for operating the system as a qubit. The cause of this high relaxation rate is likely in part due to quasiparticle poisoning from the nearby gates and dielectric material or the semiconductor buffer layer. Evidence of quasiparticle poisoning is seen in the critical current of the hybrid device when operated as an asymmetric SQUID confirming that it is present in these devices.

Reducing quasiparticle poisoning may require altering the metals and dielectric used for contacting and gating the device or changing to a different semiconductor structure entirely. Ensuring the electronic system is well thermalised to low temperature, placing quasiparticle traps made from normal metal far from the junction and using a high gap superconductor would reduce both the number of quasiparticles present and their ability to move into the junction region. Increasing the coupling strength is another option to improve the microwave signal. Moving the loop closer to the resonator will increase the inductive coupling while overlapping them and connecting them directly will change the nature of the coupling to a galvanic one. This will change the resonator properties since the impedance load at one end is altered, but if the increase in coupling strength is enough it may be worthwhile to consider.

Chapter 7

Conclusion

In this thesis I have presented a series of experiments on superconductor - semiconductor Josephson junctions and related devices which I summarise the key points of below.

Simultaneous RF Reflectometry and DC Transport

One of the main goals was to combine DC transport measurements with high frequency measurements. This concept is demonstrated in chapter 4 where transport and RF reflectometry were performed simultaneously on a superconducting tunnel junction. This was achieved by connecting the junction to an LC resonant circuit used as an impedance transformer, making the reflected RF power sensitive to changes in device resistance in near the circuit's resonance frequency. By also connecting a bias-T at the device source, transport measurements could be performed alongside reflectometry. The two measurements were compared as a function of source - drain voltage bias and perpendicular magnetic field showing a correspondence in features that mark the superconducting gap edge. Other sub-gap features, particularly around zero voltage bias, appear more strongly in the RF signal suggesting it may be sensitive to reactive changes in the device that the transport measurement is not. Also of note is that increasing the RF power incident on the device causes features in the transport measurement to broaden and distort so care must be taken when performing simultaneous measurements to use small enough stimuli that the device remains in equilibrium.

A response curve was obtained showing the relationship between the RF reflectometry signal amplitude and the device resistance measured in transport. The RF measurement is most

sensitive near the matching resistance, which can be altered by changing the tank circuit elements so that the high sensitivity occurs in the resistance range of interest. The measured response curve was compared to what would be expected from a simple model of the device as a resistor connected to the LC tank circuit and reasonable agreement is obtained by assuming a small additional series resistance.

RF reflectometry was shown to allow measurement of device impedance at high frequency making it possible to perform fast measurements and perhaps resolve certain time domain dynamics. Having tested a tunnel junction, the next step was move to super - semi junctions which could be measured with a similar setup in a range of transport regimes.

Super - Semi Junctions and the Few Mode Regime

Section 5.1 of chapter 5 showed progress towards making fully proximitised graphene Josephson junctions using CVD graphene grown by collaborators at CAPE, University of Cambridge. Using large area CVD graphene allowed devices to be fabricated quickly in relatively large batches compared to exfoliated graphene flakes, but there is a trade-off in graphene quality and therefore device yield. The effects of encapsulating the devices in Al_2O_3 dielectric deposited by ALD were explored. The junctions were initially highly p-doped but encapsulation shifted the Dirac point close to zero gate voltage and their overall resistance was reduced. It seems that encapsulation drives out some of the impurities, such as polymer residues from fabrication, while preventing further contamination of the graphene.

The metal - graphene interface transparency determines the strength of the superconducting proximity effect so a low contact resistance is required to obtain fully proximitised junctions. To improve metal - graphene contact resistance, different contact metal combinations were tried as well as introducing a light etch process prior to metallisation. Doing this improved the contact resistance somewhat but the values remained high at $\sim$10 kΩ µm compared to the typical $<$1 kΩ µm in devices where supercurrent effects are seen. Low temperature transport measurements show a soft superconducting gap confirming that the contact resistance is not yet low enough for a full proximity effect. Further changes to the fabrication process may have improved the metal - graphene interface incrementally, but taking a new approach in a different material proved to be the best way to proceed.

In section 5.2 the epi-Al/InAs 2DEG material grown by collaborators in the Manfra group at Purdue University is introduced, in which a highly transparent super - semi interface is

obtained by epitaxial Al growth leading to a strongly proximitised InAs 2DEG. Josephson junction devices fabricated on this material showed a hard gap and clearly defined supercurrent region, confirming a full proximity effect. Junction critical currents could be varied by a gate voltage allowing QPC definition in split gated devices. In these 'Andreev QPC' devices, the number of Andreev bound states and their transmissions can be altered using the gate.

The transport regime close to pinch-off where a few ABS contribute to transport was identified and measurements there showed re-emergence of supercurrent-like features at certain gate voltages. The critical currents of these features were slightly below what would be expected from one ballistic mode, giving upper estimates for ABS transmissions of $\tau \approx 0.92 - 0.97$, meaning these junctions are quasi-ballistic. At other gate voltages in the few mode regime, various sub-gap peaks were observed which are likely due to multiple Andreev reflections.

The few mode regime of these Andreev QPC devices showed a rich structure in transport due to the existence of quasi-ballistic modes. The high mode transmissions mean ABS transition frequencies are likely to be low enough ($\sim$10 GHz) to couple to microwaves. Therefore the Andreev QPC device structure is suitable for investigating individual ABS further in transport and by coupling to a microwave resonator.

Coupling Andreev Bound States to a Superconducting Microwave Resonator

The devices in chapter 6 combine the Andreev QPC from above with the microwave circuitry used by others for Andreev qubits. Embedding the junction in a superconducting loop which is inductively coupled to a superconducting resonator couples ABS in the junction to microwaves in the resonator. Magnetic flux can be applied through the loop to phase bias the junction meaning this setup gives both flux and gate control of ABS in the junction.

In the 'Hybrid' device, the QPC junction is connected to source/drain leads via additional 'control' junctions which are top gated to connect or break the current path. As well as the QPC junction, the loop contains another control junction used for breaking or completing the loop itself to respectively disable or enable coupling to the resonator. These control junctions make the device a re-configurable superconducting network which can be operated in either transport or microwave spectroscopy measurement modes. Measurements of the transport current and microwave resonator spectroscopy as a function of flux and gate voltage showed

a correlation between the critical current and resonator frequency shift meaning circuit QED could be used for fast measurement of ABS dynamics.

The 'Isolated' device has no source/drain leads or other control junctions meaning the QPC junction is only coupled to the resonator. The resonator quality factor was higher in this device allowing hybridisation between the resonator and ABS states to be resolved as avoided crossings. The transition to the few mode regime in gate voltage is identified by a saturation of the average resonator frequency and a drop in the density of crossing events. In the few mode regime, single crossings in both flux and gate voltage were compared to a model of the ABS - resonator system giving the coupling as $g \approx 18$ MHz. This is much lower than the ABS relaxation rate found from the model, $\gamma \approx 1$ GHz, meaning the device is in the weak coupling regime and cannot be reliably operated as a qubit. The high relaxation rate of ABS in the junction may be caused by a combination of quasiparticle poisoning and charge noise due to nearby gates and gate dielectric, the semiconductor buffer layer, and the InP substrate.

Transport and microwave spectroscopy were performed on the hybrid device, with each measurement providing complementary information about junction properties. In the isolated device, hybridisation between individual ABS and the resonator is observed but the weak coupling and high relaxation rate hindered operating the ABS - resonator system as a qubit.

Future Directions

Measurement of super-semi junctions in transport and microwave spectroscopy was achieved by combining certain key elements which could inform future experiments into transport and circuit QED measurement/control of Andreev bound states:

(1) The Andreev QPC, a highly transmitting super-semi junction QPC. Interesting transport structure was seen in the few mode regime which could be investigated further.

(2) The Andreev qubit geometry for circuit QED measurement. A gate tuneable transmon (gatemon) has been shown using the epi-Al/InAs 2DEG [89]. A gatemon or Andreev qubit with an Andreev QPC would allow individual ABS to be measured via circuit QED.

(3) A superconducting network with superconducting switches to alter the device geometry and change between measurement modes. Efforts to produce Majorana bound state qubits would benefit from the ability to switch between searching for MBS signatures in transport and using circuit QED to measure qubit lifetimes in the same device.

References

[1] R. C. Jaklevic, J. Lambe, A. H. Silver, and J. E. Mercereau, *Quantum interference effects in josephson tunneling*, Phys. Rev. Lett. **12**, 159 (1964). (Cited on page 2.)

[2] P. K. Day, H. G. LeDuc, B. A. Mazin, A. Vayonakis, and J. Zmuidzinas, *A broadband superconducting detector suitable for use in large arrays*, Nature **425**, 817 (2003). (Cited on page 2.)

[3] C. M. Caves, *Quantum limits on noise in linear amplifiers*, Physical Review D **26**, 1817 (1982). (Cited on page 2.)

[4] B. Yurke, L. R. Corruccini, P. G. Kaminsky, L. W. Rupp, A. D. Smith, A. H. Silver, R. W. Simon, and E. A. Whittaker, *Observation of parametric amplification and deamplification in a josephson parametric amplifier*, Phys. Rev. A **39**, 2519 (1989). (Cited on page 2.)

[5] P. W. Shor, Algorithms for quantum computation: discrete logarithms and factoring, in *Proceedings 35th Annual Symposium on Foundations of Computer Science*, pages 124–134, 1994. (Cited on page 2.)

[6] L. K. Grover, A fast quantum mechanical algorithm for database search, in *Proceedings of the Twenty-eighth Annual ACM Symposium on Theory of Computing*, STOC '96, pages 212–219, New York, NY, USA, 1996, ACM. (Cited on page 2.)

[7] C. Dickel, How to make artificial atoms out of electrical circuits – part II: Circuit quantum electrodynamics and the transmon, 'Bits of Quantum' QuTech Blog, 2017, http://blog.qutech.nl/index.php/2017/08/13/how-to-make-artificial-atoms-out-of-electrical-circuits-part-ii-circuit-quantum-electrodynamics-and-the-transmon/, Last accessed on 2020-05-20. (Cited on page 3.)

[8] V. Bouchiat, D. Vion, P. Joyez, D. Esteve, and M. H. Devoret, *Quantum coherence with a single cooper pair*, Physica Scripta **T76**, 165 (1998). (Cited on page 3.)

[9] Y. Nakamura, Y. A. Pashkin, and J. S. Tsai, *Coherent control of macroscopic quantum states in a single-Cooper-pair box*, Nature **398**, 786 (1999). (Cited on page 3.)

[10] J. Koch, T. M. Yu, J. Gambetta, A. A. Houck, D. I. Schuster, J. Majer, A. Blais, M. H. Devoret, S. M. Girvin, and R. J. Schoelkopf, *Charge-insensitive qubit design derived from the Cooper pair box*, Physical Review A - Atomic, Molecular, and Optical Physics **76**, 1 (2007). (Cited on page 4.)

[11] E. Majorana, *Symmetric Theory of the Electron and the Positron*, Il Nuovo Cimento **5**, 171 (1937). (Cited on page 6.)

[12] F. Wilczek, *Majorana returns*, Nature Physics **5**, 614 (2009). (Cited on page 6.)

[13] J. Alicea, *New directions in the pursuit of Majorana fermions in solid state systems*, Reports on Progress in Physics **75** (2012). (Cited on page 6.)

[14] C. Beenakker, *Search for Majorana Fermions in Superconductors*, Annual Review of Condensed Matter Physics **4**, 113 (2013). (Cited on page 6.)

[15] A. P. Mackenzie, *The superconductivity of Sr_2RuO_4 and the physics of spin-triplet pairing*, Reviews of Modern Physics **75**, 657 (2003). (Cited on page 6.)

[16] S. Das Sarma, C. Nayak, and S. Tewari, *Proposal to stabilize and detect half-quantum vortices in strontium ruthenate thin films: Non-Abelian braiding statistics of vortices in a px +i py superconductor*, Physical Review B - Condensed Matter and Materials Physics **73**, 3 (2006). (Cited on page 6.)

[17] L. Fu and C. L. Kane, *Superconducting proximity effect and majorana fermions at the surface of a topological insulator*, Physical Review Letters **100**, 096407 (2008). (Cited on page 6.)

[18] A. L. Rakhmanov, A. V. Rozhkov, and F. Nori, *Majorana fermions in pinned vortices*, Physical Review B **84**, 075141 (2011). (Cited on page 6.)

[19] P. A. Ioselevich, P. M. Ostrovsky, and M. V. Feigel'man, *Majorana state on the surface of a disordered three-dimensional topological insulator*, Physical Review B **86**, 035441 (2012). (Cited on page 6.)

[20] P. San-Jose, J. L. Lado, R. Aguado, F. Guinea, and J. Fernández-Rossier, *Majorana zero modes in graphene*, Physical Review X **5**, 1 (2015). (Cited on page 6.)

[21] A. Y. Kitaev, *Unpaired Majorana fermions in quantum wires*, Phys.-Usp. **44**, 131 (2001). (Cited on page 6.)

[22] J. D. Sau, R. M. Lutchyn, S. Tewari, and S. Das Sarma, *Generic New Platform for Topological Quantum Computation Using Semiconductor Heterostructures*, Physical Review Letters **104**, 040502 (2010). (Cited on page 6.)

[23] V. Mourik, K. Zuo, S. M. Frolov, S. R. Plissard, E. P. A. M. Bakkers, and L. P. Kouwenhoven, *Signatures of majorana fermions in hybrid superconductor-semiconductor nanowire devices*, Science **336**, 1003 (2012). (Cited on page 6.)

[24] L. P. Rokhinson, X. Liu, and J. K. Furdyna, *The fractional a.c. Josephson effect in a semiconductor–superconductor nanowire as a signature of Majorana particles*, Nature Physics **8**, 795 (2012). (Cited on page 6.)

[25] J. P. Xu et al., *Experimental detection of a Majorana mode in the core of a magnetic vortex inside a topological insulator-superconductor $Bi_2Te_3/NbSe_2$ heterostructure*, Physical Review Letters **114**, 1 (2015). (Cited on page 6.)

[26] D. Laroche et al., *Observation of the 4π-periodic Josephson effect in InAs nanowires*, Nautre Communications , 1 (2019). (Cited on page 6.)

[27] C. W. Beenakker and H. van Houten, *Quantum Transport in Semiconductor Nanostructures*, Solid State Physics **44**, 1 (1991). (Cited on page 11.)

[28] L. N. Cooper, *Bound Electron Pairs in a Degenerate Fermi Gas*, Physical Review **104**, 1189 (1956). (Cited on page 13.)

[29] J. Bardeen, L. N. Cooper, and J. R. Schrieffer, *Microscopic Theory of Superconductivity*, Physical Review **106**, 162 (1957). (Cited on page 13.)

[30] J. Bardeen, L. N. Cooper, and J. R. Schrieffer, *Theory of Superconductivity*, Physical Review **108**, 1175 (1957). (Cited on page 13.)

[31] A. F. Andreev, *THE THERMAL CONDUCTIVITY OFTHE INTERMEDIATE STATE IN SUPERCONDUCTORS*, Journal of Experimental and Theoretical Physics **19**, 1228 (1964). (Cited on page 14.)

[32] C. W.J. Beenakker, *Universal Limit of Critical-Current Fluctuations in Mesoscopic Josephson Junctions*, Physical Review Letters **67**, 3836 (1991). (Cited on page 15.)

[33] L. Bretheau, *Localized Excitations in Superconducting Atomic Contacts: Probing the Andreev Doublet*, PhD thesis, Universit´e Paris-Saclay, 2013. (Cited on pages 16, 20, 81, and 97.)

[34] B. D. Josephson, *The discovery of tunnelling supercurrents*, Rev. Mod. Phys. **46**, 251 (1974). (Cited on page 17.)

[35] M. Kjaergaard, *Proximity Induced Superconducting Properties in One and Two Dimensional Semiconductors*, PhD thesis, University of Copenhagen, 2015. (Cited on pages 18 and 83.)

[36] G. E. Blonder, M. Tinkham, and T. M. Klap, *Transition from metallic to tunneling regimes in superconducing microconstrictions: Excess current, charge imbalance and supercurrent conversion*, Physical Review B **25**, 4515 (1982). (Cited on page 18.)

[37] T. M. Klapwijk and G. Blonder, *Explanation of subharmonic energy gap structure in superconducting contacts*, **4363** (1982). (Cited on page 18.)

[38] M. Octavio, M. Tinkham, G. E. Blonder, and T. M. Klapwijk, *Subharmonic energy-gap structure in superconducting constrictions*, Physical Review B **27**, 6739 (1983). (Cited on page 18.)

[39] D. Averin and A. Bardas, *ac Josephson Effect in a Single Quantum Channel*, Phys. Rev. Lett. **75**, 1831 (1995). (Cited on page 18.)

[40] E. N. Bratus', V. S. Shumeiko, and G. Wendin, *Theory of subharmonic gap structure in superconducting mesoscopic tunnel contacts*, Phys. Rev. Lett. **74**, 2110 (1995). (Cited on page 18.)

[41] J. C. Cuevas, A. Martin-Rodero, and A. L. Yeyati, *Hamiltonian approach to the transport properties of superconducting quantum point contacts*, **54**, 7366 (1996). (Cited on page 18.)

[42] W. D. Oliver, Superconducting Qubits, in *Quantum Information Processing: Lecture Notes of the 44th IFF Spring School 2013*, edited by D. P. Divincenzo, chapter A4, Forschungszentrum Jülich, 2013. (Cited on page 19.)

[43] A. Blais, R. S. Huang, A. Wallraff, S. M. Girvin, and R. J. Schoelkopf, *Cavity quantum electrodynamics for superconducting electrical circuits: An architecture for quantum computation*, Physical Review A - Atomic, Molecular, and Optical Physics **69**, 1 (2004). (Cited on pages 21 and 100.)

[44] A. P. Rodríguez, Circuit Quantum Electrodynamics with Transmon Qubits in the Ultrastrong Coupling Regime, Master's thesis, University of the Basque Country, 2016. (Cited on page 22.)

[45] S. Bishop, *Circuit Quantum Electrodynamics*, PhD thesis, Yale University, 2010. (Cited on page 22.)

[46] C. Janvier, *Coherent manipulation of Andreev Bound States in an atomic contact*, PhD thesis, Universit´e Paris-Saclay, 2017. (Cited on pages 24 and 87.)

[47] A. N. Omelyanchouk, S. N. Shevchenko, Y. S. Greenberg, O. Astafiev, and E. Il'ichev, *Quantum behavior of a flux qubit coupled to a resonator*, Low Temperature Physics **36**, 893 (2010). (Cited on page 24.)

[48] K. S. Novoselov, A. K. Geim, S. V. Morozov, D. Jiang, Y. Zhang, S. V. Dubonos, I. V. Grigorieva, and A. A. Firsov, *Electric Field Effect in Atomically Thin Carbon Films*, Science **306**, 666 (2004). (Cited on page 25.)

[49] A. K. Geim and K. S. Novoselov, *The rise of graphene*, Nature Materials **6**, 183 (2007). (Cited on pages 25 and 26.)

[50] A. H. C. Neto, F. Guinea, N. M. R. Peres, K. S. Novoselov, and A. K. Geim, *The electronic properties of graphene*, Reviews of Modern Physics **81** (2007). (Cited on page 25.)

[51] E. McCann, Electronic properties of monolayer and bilayer graphene, in *Graphene Nanoelectrics*, edited by H. Raza, Springer Berlin Heidelberg, 2011. (Cited on page 25.)

[52] J. Gao, *The Physics of Superconducting Microwave Resonators*, PhD thesis, California Institute of Technology, 2008. (Cited on page 40.)

[53] M. Göppl, A. Fragner, M. Baur, R. Bianchetti, S. Filipp, J. M. Fink, P. J. Leek, G. Puebla, L. Steffen, and A. Wallraff, *Coplanar waveguide resonators for circuit quantum electrodynamics*, Journal of Applied Physics **104**, 113904 (2008). (Cited on page 40.)

[54] A. Esmail, *Charge dynamics in superconducting double dots*, PhD thesis, University of Cambridge, 2017. (Cited on pages 47 and 123.)

[55] U. Kemiktarak, *Radio-Frequency Scanning Tunneling Microscopy: Instrumentation and Applications To Physical Measurements*, PhD thesis, Boston University, 2010. (Cited on page 58.)

[56] H. B. Heersche, P. Jarillo-Herrero, J. B. Oostinga, L. M. K. Vandersypen, and A. F. Morpurgo, *Bipolar supercurrent in graphene*, Nature **446**, 56 (2007). (Cited on page 62.)

[57] X. Du, I. Skachko, and E. Y. Andrei, *Josephson current and multiple Andreev reflections in graphene SNS junctions*, Physical Review B - Condensed Matter and Materials Physics **77**, 1 (2008). (Cited on page 62.)

[58] C. Ojeda-Aristizabal, M. Ferrier, S. Guéron, and H. Bouchiat, *Tuning the proximity effect in a superconductor-graphene-superconductor junction*, Physical Review B - Condensed Matter and Materials Physics **79**, 1 (2009). (Cited on page 62.)

[59] V. E. Calado, S. Goswami, G. Nanda, M. Diez, A. R. Akhmerov, K. Watanabe, T. Taniguchi, T. M. Klapwijk, and L. M. Vandersypen, *Ballistic Josephson junctions in edge-contacted graphene*, Nature Nanotechnology **10**, 761 (2015). (Cited on page 62.)

[60] M. Ben Shalom et al., *Proximity superconductivity in ballistic graphene, from Fabry-Perot oscillations to random Andreev states in magnetic field*, Nature Physics **12**, 318 (2015). (Cited on pages 62 and 66.)

[61] L. Bretheau, J. I. Wang, R. Pisoni, K. Watanabe, T. Taniguchi, and P. Jarillo-Herrero, *Tunnelling spectroscopy of Andreev states in graphene*, Nature Physics **13**, 756 (2017). (Cited on pages 62 and 71.)

[62] Z. A. Van Veldhoven, J. A. Alexander-Webber, A. A. Sagade, P. Braeuninger-Weimer, and S. Hofmann, *Electronic properties of CVD graphene: The role of grain boundaries, atmospheric doping, and encapsulation by ALD*, Physica Status Solidi (B) Basic Research **253**, 2321 (2016). (Cited on pages 62, 67, and 124.)

[63] C. A. Chavarin, A. A. Sagade, D. Neumaier, G. Bacher, and W. Mertin, *On the origin of contact resistances in graphene devices fabricated by optical lithography*, Applied Physics A: Materials Science and Processing **122**, 1 (2016). (Cited on page 62.)

[64] J. C. Hammer, J. C. Cuevas, F. S. Bergeret, and W. Belzig, *Density of states and supercurrent in diffusive SNS junctions: Roles of nonideal interfaces and spin-flip scattering*, Physical Review B - Condensed Matter and Materials Physics **76**, 1 (2007). (Cited on page 63.)

[65] W. Liu, J. Wei, X. Sun, and H. Yu, *A Study on Graphene—Metal Contact*, Crystals **3**, 257 (2013). (Cited on page 63.)

[66] A. Allain, J. Kang, K. Banerjee, and A. Kis, *Electrical contacts to two-dimensional semiconductors*, Nature Materials **14**, 1195 (2015). (Cited on page 63.)

[67] T. Cusati, G. Fiori, A. Gahoi, V. Passi, M. C. Lemme, A. Fortunelli, and G. Iannaccone, *Electrical properties of graphene-metal contacts*, Scientific Reports **7**, 1 (2017). (Cited on page 63.)

[68] S. Min Song, J. K. Park, O. J. Sul, and B. J. Cho, *Determination of work function of graphene under a metal electrode and its role in contact resistance*, Nano Letters **12**, 3887 (2012). (Cited on page 63.)

[69] S. A. Peng et al., *The sheet resistance of graphene under contact and its effect on the derived specific contact resistivity*, Carbon **82**, 500 (2015). (Cited on page 63.)

[70] G. Giovannetti, P. A. Khomyakov, G. Brocks, V. M. Karpan, J. van den Brink, and P. J. Kelly, *Doping graphene with metal contacts*, Phys. Rev. Lett. **101**, 026803 (2008). (Cited on page 63.)

[71] J. A. Robinson, M. Labella, M. Zhu, M. Hollander, R. Kasarda, Z. Hughes, K. Trumbull, R. Cavalero, and D. Snyder, *Contacting graphene*, Applied Physics Letters **98** (2011). (Cited on pages 63 and 64.)

[72] M. Politou et al., *Transition metal contacts to graphene*, Applied Physics Letters **107** (2015). (Cited on page 63.)

[73] B. C. Huang, M. Zhang, Y. Wang, and J. Woo, *Contact resistance in top-gated graphene field-effect transistors*, Applied Physics Letters **99**, 97 (2011). (Cited on page 63.)

[74] F. Xia, V. Perebeinos, Y. M. Lin, Y. Wu, and P. Avouris, *The origins and limits of metal-graphene junction resistance*, Nature Nanotechnology **6**, 179 (2011). (Cited on page 63.)

[75] C. Girit, V. Bouchiat, O. Naaman, Y. Zhang, M. F. Crommie, A. Zettl, and I. Siddiqi, *Tunable Graphene DC Superconducting Quantum Interference Device*, Nano Letters **9**, 198 (2009). (Cited on pages 63 and 96.)

[76] Y. Matsuda, W.-Q. Deng, and W. A. Goddard, *Contact resistance for "end-contacted" metal-graphene and metal-nanotube interfaces from quantum mechanics*, The Journal of Physical Chemistry C **114**, 17845 (2010). (Cited on page 63.)

[77] J. T. Smith, A. D. Franklin, D. B. Farmer, and C. D. Dimitrakopoulos, *Reducing contact resistance in graphene devices through contact area patterning*, ACS Nano **7**, 3661 (2013). (Cited on page 64.)

[78] S. Min Song, T. Yong Kim, O. Jae Sul, W. Cheol Shin, and B. Jin Cho, *Improvement of graphene-metal contact resistance by introducing edge contacts at graphene under metal*, Applied Physics Letters **104** (2014). (Cited on page 64.)

[79] L. Anzi et al., *Ultra-low contact resistance in graphene devices at the Dirac point*, 2D Materials **5**, 025014 (2018). (Cited on page 64.)

[80] S. Kim, J. Nah, I. Jo, D. Shahrjerdi, L. Colombo, Z. Yao, E. Tutuc, and S. K. Banerjee, *Realization of a high mobility dual-gated graphene field-effect transistor with Al_2O_3 dielectric*, Applied Physics Letters **94**, 062107 (2009). (Cited on page 65.)

[81] H. Zhong, Z. Zhang, H. Xu, C. Qiu, and L. M. Peng, *Comparison of mobility extraction methods based on field-effect measurements for graphene*, AIP Advances **5** (2015). (Cited on page 65.)

[82] J. Shabani et al., *Two-dimensional epitaxial superconductor-semiconductor heterostructures: A platform for topological superconducting networks*, Physical Review B **93**, 1 (2016). (Cited on page 74.)

[83] M. Kjaergaard, H. J. Suominen, M. P. Nowak, A. R. Akhmerov, J. Shabani, C. J. Palmstrøm, F. Nichele, and C. M. Marcus, *Transparent Semiconductor-Superconductor Interface and Induced Gap in an Epitaxial Heterostructure Josephson Junction*, Physical Review Applied **7**, 1 (2017). (Cited on pages 74 and 83.)

[84] M. Kjaergaard et al., *Quantized conductance doubling and hard gap in a two-dimensional semiconductor–superconductor heterostructure*, Nature Communications **7**, 12841 (2016). (Cited on pages 75 and 83.)

[85] T. Dirks, T. L. Hughes, S. Lal, B. Uchoa, Y.-F. Chen, C. Chialvo, P. M. Goldbart, and N. Mason, *Transport through Andreev bound states in a graphene quantum dot*, Nature Physics **7**, 386 (2011). (Cited on page 76.)

[86] A. Zazunov, V. S. Shumeiko, E. N. Bratus', J. Lantz, and G. Wendin, *Andreev Level Qubit*, Physical Review Letters **90**, 4 (2003). (Cited on page 87.)

[87] C. Janvier et al., *Coherent manipulation of Andreev states in superconducting atomic contacts*, Science **349**, 1199 (2015). (Cited on page 87.)

[88] M. Hays, G. De Lange, K. Serniak, D. J. Van Woerkom, D. Bouman, P. Krogstrup, J. Nygård, A. Geresdi, and M. H. Devoret, *Direct Microwave Measurement of Andreev-Bound-State Dynamics in a Semiconductor-Nanowire Josephson Junction*, Physical Review Letters **121**, 047001 (2018). (Cited on pages 87 and 100.)

[89] L. Casparis et al., *Superconducting gatemon qubit based on a proximitized two-dimensional electron gas*, Nature Nanotechnology **13**, 915 (2018). (Cited on pages 91 and 110.)

[90] C. Janvier, L. Tosi, Ç. Ö. Girit, M. F. Goffman, H. Pothier, and C. Urbina, *Superconducting atomic contacts inductively coupled to a microwave resonator*, Journal of Physics: Condensed Matter **26**, 474208 (2014). (Cited on page 91.)

[91] G. Nanda, J. L. Aguilera-Servin, P. Rakyta, A. Kormányos, R. Kleiner, D. Koelle, K. Watanabe, T. Taniguchi, L. M. K. Vandersypen, and S. Goswami, *Current-Phase Relation of Ballistic Graphene Josephson Junctions*, Nano Letters **17**, 3396 (2017). (Cited on page 96.)

[92] M. D. Thompson, M. Ben Shalom, A. K. Geim, A. J. Matthews, J. White, Z. Melhem, Y. A. Pashkin, R. P. Haley, and J. R. Prance, *Graphene-based tunable SQUIDs*, Applied Physics Letters **110** (2017). (Cited on page 96.)

[93] M. Zgirski, L. Bretheau, Q. Le Masne, H. Pothier, D. Esteve, and C. Urbina, *Evidence for Long-Lived Quasiparticles Trapped in Superconducting Point Contacts*, Physical Review Letters **106**, 257003 (2011). (Cited on page 97.)

[94] J. Johansson, P. Nation, and F. Nori, *Qutip 2: A python framework for the dynamics of open quantum systems*, Computer Physics Communications **184**, 1234 (2013). (Cited on page 102.)

[95] A. Wallraff, D. I. Schuster, A. Blais, L. Frunzio, R. S. Huang, J. Majer, S. Kumar, S. M. Girvin, and R. J. Schoelkopf, *Strong coupling of a single photon to a superconducting qubit using circuit quantum electrodynamics*, Nature **431**, 162 (2004). (Cited on page 105.)

Appendix A

Device Fabrication Recipes

A.1 Common Fabrication Processes

Resist Processing

Resists are typically long-chain polymers which have a variable solubility in certain solvents depending on their length. Lithography is performed by exposing the resist to radiation or high energy particles which break apart the chains and reduces the average chain length selectively in the exposed regions. This allows certain regions of polymer to be dissolved away while leaving others behind forming a mask for further processing.

Chips are coated in resist by spinning the chip after applying a few drops of resist which spreads the resist into an even layer across most of the chip. The edges of the chip will have slightly raised resist called edge beads and these must be considered when designing patterns near the edge of chips. Using a chip slightly larger than the final intended size during fabrication is the easiest way to get around this so that the resist is flat across the whole pattern.

One layer of resist is sufficient for many processes but lifting off metal or dielectric from small features may be improved by an undercut in the resist profile. This is achieved by spinning on two layers of resist with the lower one having a higher sensitivity to lithography than the top layer.

Lithography

Two main types of lithography are used, optical (or photo-) lithography where ultraviolet radiation is used to break apart the chains and electron beam lithography (EBL) where thermal electrons are accelerated to form a high energy beam. Optical lithography is generally quicker and requires less specialised equipment than EBL but is limited in resolution by the radiation wavelength to around 0.5 - 1 μm. For finer features down to 20 nm EBL is more suitable.

The pattern for a device is designed using a CAD program (AutoCAD for example) and each step kept on a different layer to easily separate them for lithography. Patterns are prepared for EBL using Beamer to fracture complicated and curved patterns into small and simple shapes and to assign doses across the pattern. The dose will depend on the chip material, pattern density resist/solvent combination so some experimentation is required to find the correct one. Beamer is also used to perform proximity effect correction (PEC) which accounts for the fact that some of the electrons dosing one area will reflect from the substrate or create secondary electrons which dose nearby regions. This means each part of the pattern cannot be treated independently and all the doses must be adjusted depending on the doses and shapes of nearby sections of the pattern.

The chip with resist is loaded onto the stage of the EBL machine and the prepared pattern used to direct the stage and beam which both move to write the pattern. Depending on the pattern and dose this can take from a few minutes to many hours so it is important to keep the temperature well controlled or account for any temperature or stage drift every so often.

Once written the chip can be unloaded and the pattern developed using an appropriate solvent. The solvent used is generally MIBK (Methyl isobutyl ketone) mixed with IPA (isopropyl alcohol) in a 1:3 ratio. Development affects the resulting pattern greatly and both an under- or over-developed pattern will cause issues for further processes so the correct developing time must be found for a particular resist / pattern / dose combination. If the pattern looks correctly developed under inspection then the chip can be moved on to the next process.

Etching

Etching is used to define device shapes by subtracting existing material. It can be divided into two broad categories: wet etching which uses liquid acids or solvents and dry etching which uses a high energy plasma made from a gas.

Wet etching involves a chemical reaction between the etchant and target material and so certain choices can be highly selective to the target material. The etch is normally isotropic but can depend on the etched material's crystal structure and orientation. The main issue with wet etching is residues deposited by the etch causing uneven etching which can be mitigated by ensuring etchants which are a mixture are mixed freshly each time, being accurate with amounts and careful with contaminants, and mixing well before and during etching. Controlling the amount etched requires making sure the temperature is well controlled and taking the chip out exactly at the right time and clearing the etchant away quickly and thoroughly. Etchant running under resist is also a problem which is solved by using resist with better adhesion to the surface or including an adhesion promoter layer.

Dry etching uses high power electromagnetic waves to strike a plasma creating ions and reactive species. These particles bombard the surface and remove material by physical momentum transfer. Reactive species can also react chemically so some dry etching is both physical and chemical in nature. By accelerating the ions a highly anisotropic etch can be achieved and since the plasma can be stopped rapidly this makes dry etching useful for defining small features. Physical etching is not selective and so when using resist or some other material as an etch mask its thickness and resistance to etching must be enough for the mask to stay intact until the desired amount of target material has been removed.

Metallisation

Metal for electrostatic gates or electrical contacts can be applied by evaporating the metal onto the chip. The chip is placed in a sealed chamber which is pumped out to form a vacuum to ensure no impurities interfere with the formation of clean metal layers. Thermal evaporation involves heating a container which holds the metal in ball or wire form by passing a large current through the container. E-beam evaporation uses an electron beam to heat the metal directly but operates similarly otherwise. The metal evaporation rate must be steady and low (typically 0.1 nm/s) to ensure growth of a high quality metal film, otherwise defects can occur which compromise the electrical properties of the film.

Metal is evaporated equally across the whole chip so the metal outside the pattern must be removed afterwards. The desired metal will be directly on the chip surface and should adhere relatively strongly while the rest will be on top of the resist left behind by lithography, Removing the excess metal is then simply a case of removing the resist by soaking in a strong solvent such as acetone for several hours or overnight after which the excess metal

lifts off from the chip. This step is sensitive to issues with metal adhesion and resist profile for example if the evaporation chamber becomes too hot during evaporation the resist profile can be altered leading to poor lift-off.

ALD

Atomic layer deposition (ALD) is used to deposit dielectric layers commonly used to separate the current path of a device from gates such as Al_2O_3 and HfO_2. The ALD machine has a vacuum chamber and multiple chemical sources. Dielectric is grown by pulsing in a small amount of precursor from the relevant sources in turn which arrange themselves on the chip evenly and combine to form the dielectric. By controlling the pulse length and repetition rate of each source it can be ensured that each cycle of pulses grows a single atomic layer so that the overall result is an ordered film made of single clean layers. A high quality dielectric film will have a high breakdown voltage ensuring that main device is well insulated from the gates.

Wire Bonding

Once a device is successfully fabricated it can then be prepared for measurement. The device must be mounted on a sample holder and connected electrically to it. Sample holders have a recess or space for the device and nearby electrical contacts which connect to the measurement circuit in the fridge setup. Devices are mounted by sticking them to the sample holder with an adhesive such as GE varnish which is electrically insulating or silver DAG which is conducting, depending on whether a back gate is required or not.

The device can then be connected to the sample holder electrically by attaching metal wire between the device bondpads and sample holder connections. A wire bonder consists of a stage on which the sample is fixed and a tip above which has the metal wire threaded through. The height difference between the two surfaces can pose problems for bonding and must be calibrated beforehand. Bonds are made by lowering the tip to the surface of the sample holder followed by the chip and breaking the wire off after, leaving a length of wire attached between the chip and sample holder bondpads.

Once a device is bonded it is even more prone to electrostatic discharge (ESD) via the sample holder connections which can destroy the device. Therefore it is advisable to have the sample

holder connections grounded while bonding and keep them grounded until the device is connected to the fridge at which point it should be grounded at the fridge setup's connections.

A.2 Tunnel Junction Devices

Device from chapter 4 which was fabricated by Adam Esmail from the Microelectronics Group, Cavendish Laboratory. The full fabrication process is outlined in ref [54] so just some key aspects are presented here. The junction is fabricated on an undoped $Si/Si0_2$ substrate by double-angle evaporation with a controlled oxidation step. This method is outlined in figure A.1 and allows tunnel junctions with a controlled resistance to be fabricated using just one EBL step and one evaporation chamber usage.

The resist is a bilayer chosen to give a large undercut when developed:

1. AR-P 617.08. Spin for 1 min @ 4000rpm, bake for 10 mins @ 180 °C, expose to UV in a light box for 1.5 hours
2. PMMA A2 2.2M. Spin for 1 min @ 2400 rpm, bake for 10 mins @ 160 °C

The first layer (lower green layer in figure A.1) is a thick layer around 500 nm tall with a low EBL clearing dose while the second (upper orange layer) is a thin layer <100 nm with a higher dose. When exposed to an e-beam dose suitable for the top layer and developed, the desired pattern will appear in the top layer while the lower layer will have a large area developed away leaving an undercut. This undercut is crucial since patterns evaporated at an angle will be displaced along the chip surface so a large space must be clear of resist.

The first metal layer is deposited at an angle and then exposed to an oxygen environment for a set time to grow a controlled aluminium oxide layer. When the next Al layer is evaporated at the second angle a tunnel barrier is formed by the grown oxide between the two metal layers. The end result is a superconductor - insulator - superconductor (SIS) Josephson junction when the Al becomes superconducting at low temperature.

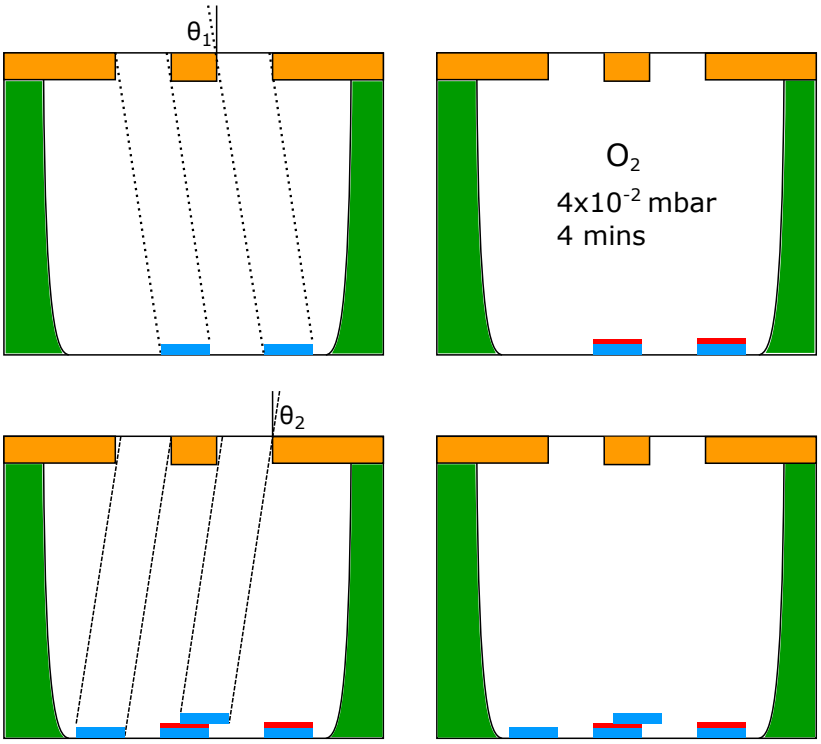

Fig. A.1 Process for tunnel junction evaporation. (top left) Al metal (blue) is evaporated at the first angle. (top right) Oxygen is introduced to the chamber to grow a controlled Al oxide (red). (bottom left) Al is evaporated at the second angle, overlapping with the first layer. (bottom right) The resulting structure is a vertical tunnel barrier.

A.3 Graphene Josephson Junctions

Fabrication of graphene devices in section 5.1. Investigating the effects of contact metal choice and encapsulation was part of the work undertaken and is described more in the chapter. Here I describe the steps in a typical overall process shown in figure A.2. Figure A.3 shows a summary of the fabrication process used for each batch as well as the result of each one and any changes which were implemented for future batches.

Graphene Transfer

The graphene is grown by collaborators at CAPE by chemical vapour deposition (CVD) on Cu substrates before being transferred to Si/SiO_2 wafers using a PMMA-based wet transfer method explained in ref [62]. Our fabrication starts from here with CVD graphene on Si/SiO_2.

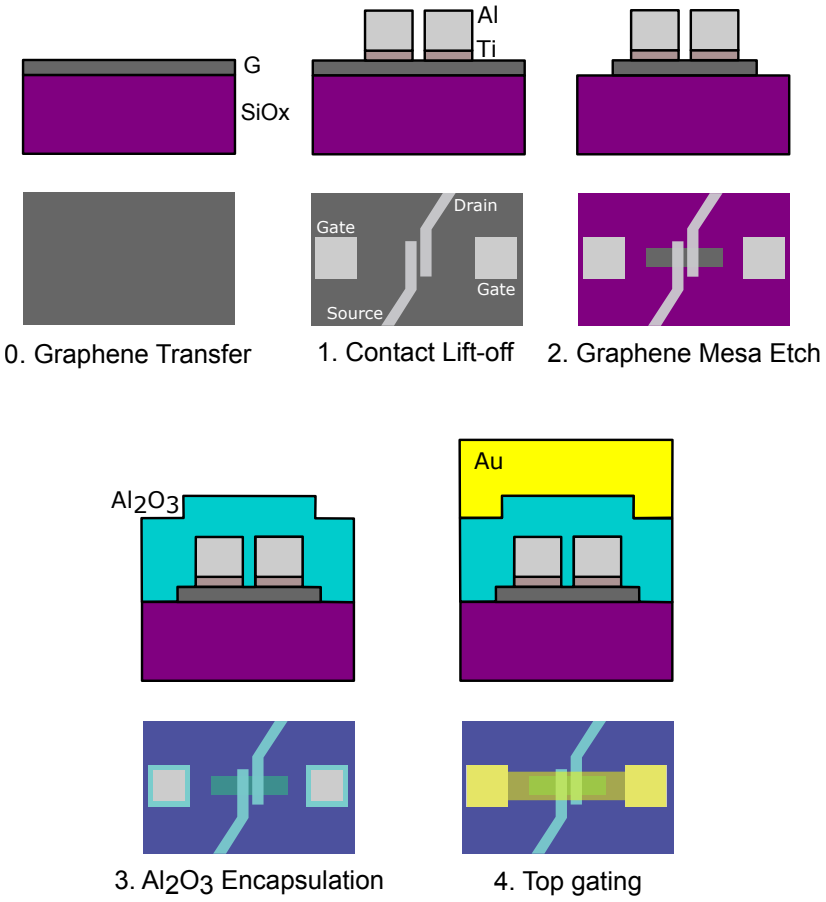

Fig. A.2 Fabrication process for graphene Josephson junctions.

Metal Contacts

Resist:

1. Spin PMMA 100k A6 1:1 anisole, 60s at 4000 rpm, bake 10 min at 125 °C.
2. Spin PMMA 950k A11 1:5 MIBK, 60s at 3500 rpm, bake 10 min at 125 °C.

EBL: Performed by EBL facility technicians who optimised for the resist structure but exact parameters unknown.

Develop: 30s in 1:3 MIBK/IPA for 30s, rinse 30s in IPA.[1]

[1] Developed patterns are often plasma ashed for 1-2 mins to clean up edges and substrate but graphene is rapidly etched by ashing and reactive ion etching so didn't plasma ash these devices throughout the fabrication except when trying to etch.

Pre-Contact Treatment: Light etch in O_2 reactive ion etcher (RIE) to clean graphene surface and improve contact to metal without removing the graphene by stopping soon after plasma strikes. 3s - 5s at 50% power.

Evaporation: Various metal combinations (see figure A.3 and section 5.1) but mainly did thermal evaporation of 10 nm Ti + 70 nm Al and sometimes + 10 Au cap. Device from Batch 10 which was cooled down and measured had 10 nm Pd + 50 nm Nb (Pd deposited by e-beam evaporation, Nb deposited by sputtering).

Lift-off: Overnight in acetone. Inspect under IPA. N_2 dry

Mesa Etch

Resist: Spin S1813, 60s at 5500 rpm, bake 1 min at 90 °C.

Photolithography: Expose 6.5s on UV mask aligner ('orange aligner').

Develop: MF319 is the standard developer for photolithography but metal ion free (MIF) developers containing TMAH will etch aluminium rapidly, destroying the contacts. Metal ion containing (MIC) developers based on NaOH or KOH attack Al slowly so AZ Developer (MIC) was used.

30s in 1:1 AZ Developer (MIC)/De-ionised (DI) H_20, rinse 30s in DI H_20.

Etch: 20s at 50% power in O_2 RIE.

Strip resist: 5 min acetone, 2 min IPA, N_2 dry.

Encapsulation

Performed by collaborators at CAPE. No lithography beforehand, just encapsulate entire chip and etch holes at bondpands after.

ALD: Deposit 30 nm - 90 nm Al_2O_3 (tried different thicknesses across batches).

Bondpad Photolithography: Spin S1813, 60s at 5500 rpm, bake 1 min at 90 °C.
Expose 6.5s on UV mask aligner ('orange aligner').
Develop 30s in MF319, rinse 30 in DI H_20.

Bondpad Etch: Al_2O_3 etch solution - 1:3 DI H_20:H_3PO_4 heated to 80 °C.

Etch as appropriate for dielectric thickness (rate ∼20-30 nm / min) and rinse 60s in DI H_20 while shaking/swirling vigorously to clear away etchant.

Strip resist: 5 min acetone, 2 min IPA, N_2 dry.

Post bake: Bake 10 min at 200 °C.

Top Gate

Resist: Spin S1813, 60s at 5500 rpm, bake 1 min at 90 °C.

Photolithography: Expose 6.5s on UV mask aligner ('orange aligner').

Develop: Soak 2 min in chlorobenzene (to help create undercut) and N_2 dry. Develop for ∼2 min in MF319 (develop in 30s increments until pattern cleared then 30s more), rinse 30s in DI H_20.

Evaporation: Thermal evaporation 10 nm Ti + 100 nm Au.

Lift-off: Overnight in acetone. Inspect under IPA. N_2 dry

Batch (un/doped)	Overall Process	Pre-Contact Treatment	Contact Metal (nm)	Encapsulation	Top-Gate	Result	Notes
1 (D)	Contacts (EBL) Mesa (PL) Encap (ALD)	none	10Ti/70Al	30nm AlOx	N	Probe station testing before/after encap shows Dirac point shift	Noticed issue with using MF319 for mesa - etches Al rapidly, used AZ351B and later AZ Developer after this
2 (D)	Contacts (EBL) Mesa (PL)	none	10Ti	none	N	Tragically incinerated along with sharps	
3 (D)	Contacts (EBL) Mesa (PL)	none	10Ti/70Al	none	N		
4 (U)	Contacts (EBL) Mesa (PL) Encap (ALD) Gate (PL)	none	10Ti/70Al	30nm AlOx	Y	Tested at probe station and later MX400 using top gate	TG process works in principle to produce gateable GJJ on undoped Si but gate leaks due to thin alumina dielectric and device mobility/ R_c still poor.
5 (U)	Contacts (EBL) Mesa (PL) Encap (ALD) Gate (PL)	none	10Ti/100Al/10Au	60nm AlOx	Y	Probe station testing before/after encap	Au cap improved yield, device quality still poor and not improved much by encap. Scribing 10x10mm chip up causes problems for graphene isolation etch
6 (D)	Contacts (EBL) Mesa (PL) Encap (ALD)	none	10Ti/100Al/10Au	60nm AlOx	N	Probe station testing	Still high resistances, couldn't test after encap because AlOx etch didn't work properly
7 (U)	Contacts (EBL) Mesa (PL)	none	10Ti/70Au	none	N	Most contacts lifted away during mesa PL	Some sort of light etch may be required for adhesion
8 (U)	Contacts (EBL) Mesa (PL)	none	10Ti/70Al/10Au	none	N	Probe station testing	Lower yield and poorer quality than expected despite doing everything that has worked before (AP, Au cap, AZ developer etc.)
9 (U)	Contacts (EBL) Mesa (PL)	Light Etch (LE) on s3,6,9	s1 - 10Ti/70Au s2,4 - 10Pd/70Au s3 - 10Pd/70Al s7 - 5Pd/70Al s5,6,8,9 - 10Pd/70Nb	none	N	Light Etch (LE) on s3 improved adhesion but 300/400nm junction L/O was poor	If doing contacts first, light etch is required to improve adhesion but causes more small junctions to be shorted
10 (U)	Contacts (EBL) Mesa (PL) Encap (ALD) Gate (PL)	LE	10Pd/50Nb	90nm AlOx. Bake 10 min @200 °C after bonpad etch	Y	Cooled down and tested in MX400	Encapsulation reduces doping but introduces hysteresis. Top-gate has a stronger lever arm than back-gate. Cooling down see soft gap but obtained low-res Vsd - Vg and Vsd - B 2D plots
SiC	Contacts (EBL) Anchor Bondpads Mesa (PL)	none	10Ti/70Al	none	N	Cooled down and tested in MX400	Process for GJJs on CVD graphene works for SiC graphene except need extra anchor etch+bondpad metal step

Fig. A.3 GJJ fabrication - Summary of process for each batch and outcomes of each iteration.

A.4 Andreev QPC Devices

The experiments on these devices are discussed in section 5.2 and chapter 6 and involved the epitaxial Al / InAs 2DEG material. The fabrication process was iterated over many times and changed throughout so just the final version of the process is shown here.

Cleaving Chips

The material starts as a 2 inch wafer which is initially divided into quarters which can then be scribed using a diamond tip and cleaved into chips. It is generally good to leave some excess at the edges to account for resist edge beads and damage from picking up the chip with tweezers so for a 10 mm x 10 mm pattern the chip would be scribed at 10.5 mm x 10.5 mm.

The wafers are stored with a protective resist layer on so after cleaving this layer is removed by a few minutes in acetone and then the chip is cleaned thoroughly to ensure a pristine starting surface:

- 2 min in acetone while sonicating[2]
- 2 min in IPA while sonicating
- Blow dry with N_2
- 2 min plasma ash[3]

Alignment Marks

Depositing alignment marks made of gold at the start allows further processes to be aligned to these clearly visible marks ensuring good alignment between different steps.

Resist:

1. Spin[4] PMMA EL9, bake 1 min at 115 °C.
2. Spin PMMA A4.5, bake 3 min at 115 °C.

[2] Generally sonicate using 80 kHz, 30% - 50% power depending on process
[3] Plasma asher is kept at 100% power and ashing time is varied as appropriate.
[4] Unless otherwise stated all resists are spun for 45s at 4000 rpm

EBL: Base dose 550 μC/cm^2, Proximity Effect Correction (PEC) 200nm PMMA on InP, 100% uniform clearing, Write Field (WF) Size 300 μm, 20k dots, beam current I = 2 nA.

Develop: 60s in 1:3 MIBK:IPA, 15s IPA rinse, N_2 dry, plasma ash for 1 min.

Evaporation: Kaufmann milling for 30s (5 min discharge, 1 min warm-up). E-beam evaporation, evaporate 5 nm Ti + 100 nm Au.

Lift-off: ∼2 hours in acetone, inspect under IPA. Sonication might be necessary. N_2 dry.

Mesa Definition

Defining the mesa requires etching away the epitaxial-Al followed by the 2DEG and buffer layer from most of the chip. A negative resist AR-N 7520 11 was used so that only the small mesa regions to be retained need to be exposed. The adhesion promoter AR 300-80 prevents delamination of the resist which could allow etchant to get under into unwanted areas.

Resist:

1. Spin AR 300-80, bake 2 min at 185 °C. Soak 2 min in 1,3-dioxolane, 1 min in acetone, 30s in IPA, N_2 dry.
2. Spin two layers of AR-N 7520 11, bake each layer 1 min at 85 °C.

EBL: Base dose 75 μC/cm^2, PEC 200nm PMMA on InP, WF 300 μm, 20k dots, I = 500 pA.

Develop: 60s in MF321, 60s rinse in Milli-Q (MQ) ultrapure water, N_2 dry. Inspect resist with microscope yellow filter. Ash 2 min. Post-bake 1 min at 115 °C.

Al etch: Transene Al etch Type D, ∼13s at 52 °C, 20s warm MQ rinse, 30s cold MQ rinse, N2 dry.

Mesa Etch:

III-V etch solution				
MQ	Citric Acid	H_3PO_4		H_2O_2
110	22.5	1.5	:	1.5

Prepare the solution using the above ratios, stirring constantly with a magnetic stirrer while mixing and etching. Add the H_2O_2 last when the chips are ready to etch.

Etch for 10 min, moving chips 1/4 of the way around container every 2.5 min, rinse 30s in MQ, N_2 blow dry.

Strip resist: 2 min in dioxolane while sonicating, 2 min acetone, 2 min IPA, N_2 dry. Ash 2 min.

Junction Etch

Resist: Spin PMMA A4.5, bake 3 min at 185 °C.

EBL: Base dose 608 μC/cm^2, PEC 200 nm PMMA on InP, WF 150 μm, 60k dots, I = 500 pA.

Develop: 60s in MIBK/IPA, rinse 20s in IPA, N_2 dry. Ash 1 min. Post bake 2 min at 115 °C.

Al etch: Transene D, ∼10s at 50ºC, 20s warm MQ rinse, 40s cold MQ rinse, N2 dry. (Vigorous swirling in MQ needed to clear away etchant).

Strip resist: 5 min acetone, 2 min IPA, N_2 dry. Ash 1 min.

ALD Gate Dielectric

Resist:

1. Spin PMMA El13, bake 1 min at 115 °C.
2. Spin PMMA A4.5, bake 1 min at 115 °C.

EBL: Base dose 900 μC/cm^2, PEC 400 nm PMMA on InP, WF 150μm, 60k dots, I = 500 pA.

Develop: 60s in MIBK/IPA, rinse 15s in IPA, N2 dry. Ash 1 min

ALD: Deposit 150 cycles HfO_2 at 110 °C. 1800s outgas time. Takes around 12 hours and gives ∼15 nm dielectric.

Lift-off: ∼2 hours in 50 °C acetone, inspection under IPA. Sonication likely to be necessary. N_2 dry. Ash 2 min.

Gates

Resist:

1. Spin PMMA El9, bake 1 min at 115 °C.
2. Spin PMMA A4.5, bake 3 min at 115 °C.

EBL: Base dose 800 μC/cm^2, PEC 400 nm PMMA on InP, WF 150μm, 60k dots, I = 500 pA.

Develop: 60s in MIBK/IPA, rinse 15s in IPA, N2 dry. Ash 1 min.

Evaporation: Evaporate 2 nm Ti + 65 nm Al.

Lift-off: ∼2 hours in 50 °C acetone, inspect under IPA. N_2 dry.

Anneal: Forming gas anneal, 30 min at 150 °C.

Microwave Circuitry

Where applicable, not present in transport only devices.

Resist:

1. Spin AR 300-80, bake 2 min at 185 °C. Soak 2 min in dioxolane, 1 min in acetone, 30s in IPA, N_2 dry.
2. Spin PMMA EL9, bake 1 min at 115 °C.
3. Spin CSAR 13, bake 3 min at 115 °C.

EBL: Bias pattern by +0.8 um then invert using NOT in Beamer. Base dose 350 μC/cm^2, PEC 500nm CSAR on InP. WF 600μm, 20k dots, I = 40 nA. Set feed/scan pitch to 10 to reduce time.

Develop: 30s in o-xylene, 30s in MIBK/IPA. IPA dip, N_2 dry. Sonicate in IPA if any residues remain. Ash 4 min.

Evaporation: Kaufmann milling 30s (3 min discharge, 1 min warm-up). Evaporate 100 nm Al while rotating.

Lift-off: Lift-off in dioxolane, inspect under IPA. Sonicate if necessary. N_2 dry. Ash 4 min.

Contacts

These "contacts" are not bondpads as the term is often used but instead for connecting the gates on top of the mesa to lines on the substrate which go out to the bondpads. Requires a large amount of metal evaporated at a high angle to climb up the mesa.

Resist:

1. Spin PMMA EL13, bake 1 min at 115 °C.
2. Spin PMMA A6, bake 3 min at 115 °C.

EBL: Base dose 826 μC/cm^2, PEC 200nm PMMA on InP, WF 150μm, 60k dots, I = 500 pA.

Develop: 75s in MIBK/IPA, rinse 10s in IPA, N_2 dry. Ash 1 min.

Evaporation: Kaufmann Milling 4min 30s (3 min discharge, 1 min warm up). Evaporate 2 nm Ti + 450nm Al. Angled Al evaporation: 20 nm at 0°, 400 nm at +45°, 30 nm at -45°.

Lift-off: ∼2 hours in acetone, inspect under IPA. N_2 dry.

Appendix B

Simulation Code

Some of the code used in this thesis for modelling systems is shown here.

B.1 Aysmmetric SQUID Critical Current

The Matlab functions and script below were used to generate figure 2.6 and modified slightly to compare to SQUID data in chapter 6. This example uses just one ABS mode in each junction of the SQUID but can be extended to include more, at the expense of adding more tuneable parameters. When comparing to the data just one mode was used and the transmissions found taken as some effective value averaged across all modes present in the real device. Lines that were split to fit into this document are denoted by the '↪' symbol.

squid_current.m

```
function I = squid_current(tau0,tau1,xi,phi)
%calculates the current in an SNS SQUID

%defining constants
e = 1.602176634e-19;
hbar = 1.0545718e-34;
Delta = e*200e-6; %superconducting gap = 200 ueV

I0 = e*Delta/(2*hbar); %prefactor in ABS current equation
```

```
%current in each junction summed together
I = I0*tau0.*sin(xi - phi./2)./(sqrt(1 - tau0*(sin((xi-phi
↪ ./2)./2)).^2)) + ...
    I0*tau1.*sin(xi + phi./2)./(sqrt(1 - tau1*(sin((xi+phi
    ↪ ./2)./2)).^2));

end
```

critical_current.m

```
function [Ic_plus, Ic_minus, xi_plus, xi_minus] =
↪ critical_current(c,phi)
%calculates critical current of an SNS SQUID using the
↪ function squid_current

tau0 = c(1);
tau1 = c(2);

xi = linspace(-pi,pi); %dummy phase parameter

 for i = 1:length(phi)
     I(i,:) = squid_current(tau0,tau1,xi,phi(i));
     [Ic_plus(i), index_plus(i)] = max(I(i,:));
     [Ic_minus(i), index_minus(i)] = min(I(i,:));
 end

 xi_plus = xi(index_plus);
 xi_minus = xi(index_minus);

end
```

asymm_squid_model.m

```
%critical current of an asymmetric SNS SQUID

%defining constants
e = 1.602176634e-19;
hbar = 1.0545718e-34;
```

```
Delta = e*200e-6; %use superconducting gap of 200 ueV

I0 = e*Delta/(2*hbar); %prefactor in ABS current equation

phi = linspace(0,2*pi,201); %phase difference

tau0 = 0.9; %mode transmissions
tau1 = 0.7;

Ic0 = (1 - sqrt(1 - tau0))*2*I0; %SNS junction Ic
Ic1 = (1 - sqrt(1 - tau1))*2*I0;
alpha = (Ic0 - Ic1)./(Ic0 + Ic1); %asymmetry parameter

c0 = [tau0,tau1,Ic0,Ic1];

Ic_SIS = sqrt(Ic0.^2 + Ic1.^2 + 2*Ic0*Ic1*cos(phi)); %
↪ critical current of an SIS SQUID with same junction
↪ critical currents

[Ic_plus, Ic_minus, xi_plus, xi_minus] = critical_current(
↪ c0,phi); %get critical current of SNS SQUID

%plot critical currents, normalised by expected max Ic0+Ic1
figure(1);clf
plot(phi/pi,Ic_plus/(Ic0+Ic1),'linewidth',2,'linestyle','-'
↪ ,'color','r');hold on;
plot(phi/pi,Ic_minus/(Ic0+Ic1),'linewidth',2,'linestyle','-
↪ ','color','b');
plot(phi/pi,Ic_SIS/(Ic0+Ic1),'linewidth',2,'linestyle','--'
↪ ,'color','k');
plot(phi/pi,-Ic_SIS/(Ic0+Ic1),'linewidth',2,'linestyle','--
↪ ','color','k','HandleVisibility','off');

xlabel('\phi / \pi','fontsize',16); ylabel('I_{c} (nA)','
↪ fontsize',16);
legend('I_{c+,SNS}','I_{c-,SNS}','I_{c,SIS}');
```

B.2 RF Reflectometry

In chapter 4, a tunnel junction embedded in a tank circuit was measured by RF reflectometry. The response of this system was modelled using the Matlab RF Toolbox to build up the effective circuit shown in figure 4.8(b) and simulate the reflected power at the circuit resonance, S11R. This was done as a function of junction resistance 'RJJ' and at different values of 'R0', to model an additional series resistance. The result was compared to the response curve obtained experimentally to confirm qualitative agreement and estimate the additional series resistance. Lines that were split to fit into this document are denoted by the '↪' symbol.

TankCircuitModel_S11R.m

```
function S11R = TankCircuitModel_S11R(f_R,RJJ,R0)
%calculates the response of a tank circuit connected to a
↪ resistive
%junction RJJ using RF Toolbox

Lin=620e-9; %inductance
Cin=0.38e-12; %%parasitic capacitance (assuming resonant
↪ frequency ~328 MHz)
N=length(RJJ); %number of steps in R
freqs = linspace(f_R-50e6, f_R+50e6, 101); %array of
↪ frequencies

for i=1:N
    Seg0 = rfckt.seriesrlc('R',R0); % creates a series rlc
    ↪ resistance
    Seg1 = rfckt.seriesrlc('L', Lin); % creates a series
    ↪ rlc component just with inductance
    Seg2 = rfckt.shuntrlc('C', Cin); % creates a shunt rlc
    ↪ component just with capacitance to model parasitic
    Seg3 = rfckt.seriesrlc('R',RJJ(i)); % This is the JJ

    cktBPF = rfckt.cascade('Ckts', {Seg0, Seg1, Seg2, Seg3
    ↪ }); %join all the components together
    analyze(cktBPF, freqs); %solve the system
```

```
    tf = cktBPF.AnalyzedResult.S_Parameters; %extract just
    ↪ the s-paramters
    S11(:,1)=tf(1,1,:); %asign S11 to its own matrix
    S11R(i)=abs(S11(51,1)); %extract S11 on resonance (
    ↪ middle of above freqs matrix)
    S11Mat(:,i)=abs(S11); %Matrix of S11 for future plots
end

end
```

R0_Series.m

```
R0 = 0:10:50; %additional series resistance
RJJ = logspace(4,9,100); %junction resistance
f_R = 328e6; %resonance frequency

for i = 1:length(R0)
    S11R(:,i) = transpose(TankCircuitModel_S11R(f_R,RJJ,R0(
    ↪ i)));
end

semilogx(RJJ,S11R);
legend(cellstr(num2str(R0', 'R0=%-d')));
xlabel('Device Resistance (\Omega)','fontsize',20);
ylabel('S11 (arb. unit)','fontsize',20);
title('S11 on Resonance with device resistance and series
↪ fitting resistance');
set(gca,'fontsize',20);
```

B.3 ABS - Resonator System

The QuTiP (python) code for modelling the ABS-resonator Hamiltonian with dissipation used in chapter 6. It was mostly contained in one file split into cells containing different simulation types and helper functions/scripts. It is used by running the 'definitions' cell at the start followed by other cells. The main scripts calculate the resonator power spectrum as a function of frequency and a swept variable: flux (single and multi mode) or transmission (single mode). These cells are similar to each other but all are shown for completeness.

Note that energies are expressed in frequency units Hz, (so a factor of h has been dropped from the Hamiltonian) and flux is in dimensionless units, normalised by the flux quantum Φ_0. Lines that were split to fit into this document are denoted by the '↪' symbol.

definitions

```
#%% definitions for full Andreev qubit model - run this first
import numpy as np
from qutip import *
import matplotlib.pyplot as plt
settings.has_mkl = False

h = 6.62607015e-34          # Planck's constant
e = 1.602176634e-19           # Electron charge
RQ = h / 4 / e**2    # Resistance quantum
scgap = 60e9         # Twice the junction superconducting gap in Hz
pi = np.pi           # pi

# Andreev energy as a function of phase and transmission tau (flux in
↪  reduced units)
def fandreev(flux, tau):

    phase = flux * 2 * np.pi
    fandreev = scgap * np.sqrt(1 - tau * np.sin (phase / 2)**2)

    return fandreev

# prefactor for the coupling g
def z(M, fcav, Zcav):
```

```
    z = pi * M**2 * (2*pi*fcav)**2 /(Zcav * RQ)

    return z

# coupling g as a function of flux and transmission. Expression from
↪  Janvier Thesis.
def g(M, fcav, Zcav, flux, tau):

    g = np.sqrt(z(M, fcav, Zcav)) * (0.5*fandreev(0.5, tau) / 2) *
    ↪  (scgap / fandreev (flux, tau) - fandreev (flux, tau) / scgap)

    return g

# prefactor before sigma_z in the Hamiltonian
def F(flux, tau):

    phase = flux * 2 * pi
    F = 1 / (np.sqrt(1 - tau) * np.tan (phase / 2))

    return F
```

flux sweep (single mode)

```
#%% Sweeping flux at fixed tau - single mode
N = 4                                   # number of cavity fock states
fc = 6.163e9                            # cavity frequency
Zc = 60                                 # cavity impedance

M = 10e-12                              # mutual inductance, controls g
kappa = 1e6                             # cavity relaxation
gamma = 1000e6                          # qubit relaxation

wlist = np.linspace(6.161e9, 6.164e9, 101)  #frequencies
fluxlist = np.linspace(0.47, 0.53,101)
tau = 0.995

spec = np.zeros((len(fluxlist), len(wlist)))
```

```
i = 0
for flux in fluxlist:
    # cavity operator
    a  = tensor(destroy(N), qeye(2))

    # operators for the Andreev level
    sm = tensor(qeye(N), sigmam())
    sz = tensor(qeye(N), sigmaz())
    sx = tensor(qeye(N), sigmax())

    # ABS - Resonator Hamiltonian
    H = fc * (a.dag() * a + 1/2) + fandreev(flux,tau)/2 * sz +
    ↪  g(M,fc,Zc,flux, tau) * (a.dag() + a) * (F(flux, tau) * sz +
    ↪  sx)

    # collapse operators
    n_th = 0.1 # finite bath temp in terms of excitation number
    c_ops = [np.sqrt(kappa * (1 + n_th)) * a, np.sqrt(kappa * n_th) *
    ↪  a.dag(), np.sqrt(gamma) * sm]

    # calculate resonator power spectrum using 'spectrum' function
    spec[i,:] = spectrum(H, wlist, c_ops, a.dag(), a)
    i = i+1

#plot the spectrum
FreqMesh, ControlMesh = np.meshgrid(wlist, fluxlist);
fig1, ax1 = plt.subplots(2,1, figsize=(6,8))
cs = ax1[0].contourf(ControlMesh,FreqMesh/1e9,1-spec/np.max(spec),50,
↪  cmap='hot');

ax1[0].set_xlabel('Flux ($\Phi/\Phi_0$)')
ax1[0].set_ylabel('S21 Frequency (GHz)')
ax1[0].set_title('S21 Magnitude \n M = %i pH, $\kappa$ = %1.2f MHz,
↪  $\gamma$ = %i MHz, $\\tau$ = %1.3f' %(M/1e-12, kappa/1e6,
↪  gamma/1e6, tau))
```

```
#plot the andreev frequency
fa = fandreev(fluxlist,tau)
ax1[1].plot(fluxlist, fa/1e9)
ax1[1].axhline(fc/1e9,linestyle='--', color='C1',label='$f_c$')
ax1[1].text(fluxlist[-2],fc/1e9 + 0.1,'$f_c$')
ax1[1].set_xlabel('Flux ($\Phi/\Phi_0$)')
ax1[1].set_ylabel('Andreev Transition Frequency (GHz)')
```

flux sweep (multi mode)

```
#%% Sweeping flux at fixed tau - multi mode
N = 4                                   # number of cavity fock states
fc = 6.163e9                            # cavity frequency
Zc = 60                                 # cavity impedance

M = 10e-12                              # mutual inductance, controls g
kappa = 1e6                             # cavity relaxation
gamma = 250e6                           # qubit relaxation

wlist = np.linspace(6.157e9, 6.165e9, 51)   #frequencies
fluxlist = np.linspace(0.45, 0.55,51)
tau1 = 0.996
tau2 = 0.991
tau3 = 0.980

spec = np.zeros((len(fluxlist), len(wlist)))

i = 0
for flux in fluxlist:
    # cavity operator
    a  = tensor(destroy(N), qeye(2), qeye(2), qeye(2))

    # operators for the 1st Andreev level
    sm = tensor(qeye(N), sigmam(), qeye(2), qeye(2))
    sz = tensor(qeye(N), sigmaz(), qeye(2), qeye(2))
    sx = tensor(qeye(N), sigmax(), qeye(2), qeye(2))

    # operators for the 2nd Andreev level
```

```
    sm2 = tensor(qeye(N), qeye(2), sigmam(), qeye(2))
    sz2 = tensor(qeye(N), qeye(2), sigmaz(), qeye(2))
    sx2 = tensor(qeye(N), qeye(2), sigmax(), qeye(2))

    # operators for the 3rd Andreev level
    sm3 = tensor(qeye(N), qeye(2), qeye(2), sigmam())
    sz3 = tensor(qeye(N), qeye(2), qeye(2), sigmaz())
    sx3 = tensor(qeye(N), qeye(2), qeye(2), sigmax())

    # ABS - Resonator Hamiltonian
    H = fc * (a.dag() * a + 1/2) + (fandreev(flux,tau1))/2 * sz +
    ↪  g(M,fc,Zc,flux, tau1) * (a.dag() + a) * (F(flux, tau1) * sz +
    ↪  sx) + (fandreev(flux,tau2))/2 * sz2 + g(M,fc,Zc,flux, tau2) *
    ↪  (a.dag() + a) * (F(flux, tau2) * sz2 + sx2) +
    ↪  (fandreev(flux,tau3))/2 * sz3 + g(M,fc,Zc,flux, tau3) *
    ↪  (a.dag() + a) * (F(flux, tau3) * sz3 + sx3)

    # collapse operators
    n_th = 0.1 # finite bath temp in terms of excitation number
    c_ops = [np.sqrt(kappa * (1 + n_th)) * a, np.sqrt(kappa * n_th) *
    ↪  a.dag(), np.sqrt(gamma) * sm, np.sqrt(gamma) * sm2,
    ↪  np.sqrt(gamma) * sm3]

    # calculate resonator power spectrum using 'spectrum' function
    spec[i,:] = spectrum(H, wlist, c_ops, a.dag(), a)
    i = i+1

#plot the spectrum
FreqMesh, ControlMesh = np.meshgrid(wlist, fluxlist);
fig1, ax1 = plt.subplots(2,1, figsize=(6,8))
cs = ax1[0].contourf(ControlMesh,FreqMesh/1e9,1-spec/np.max(spec),50,
↪  cmap='hot');

ax1[0].set_xlabel('Flux ($\Phi/\Phi_0$)')
ax1[0].set_ylabel('S21 Frequency (GHz)')
```

```
ax1[0].set_title('S21 Magnitude vs Flux (3 mode) \n M = %i pH,
↪  $\kappa$ = %1.2f MHz, $\gamma$ = %i MHz, $\\tau$ = %1.4f'
↪  %(M/1e-12, kappa/1e6, gamma/1e6, tau1))

#plot the andreev frequencies
ax1[1].plot(fluxlist, fandreev(fluxlist,tau1)/1e9)
ax1[1].plot(fluxlist,fandreev(fluxlist,tau2)/1e9)
ax1[1].plot(fluxlist,fandreev(fluxlist,tau3)/1e9)
ax1[1].axhline(fc/1e9,linestyle='--', color='C1',label='$\omega_c$')
ax1[1].text(fluxlist[-2],fc/1e9 + 0.1,'$f_c$')
ax1[1].set_xlabel('Flux ($\Phi/\Phi_0$)')
ax1[1].set_ylabel('Andreev Transition Frequency (GHz)')
```

τ sweep (single mode)

```
#%% Generating random values for randomly varying tau
randpos = np.random.rand(101) - 0.5
randtau = (randpos + abs(min(randpos)))
randtau = randtau / max(randtau)
plt.plot(randtau)

#%% Sweeping tau at fixed flux - single mode
N = 4                                   # number of cavity fock states
fc = 6.163e9                            # cavity frequency
Zc = 60                                 # cavity impedance

M = 10e-12                              # mutual inductance, controls g
kappa = 1e6                             # cavity relaxation
gamma = 1000e6                          # qubit relaxation

wlist = np.linspace(6.161e9, 6.164e9, 101) #frequencies
flux = 0.5
taulist = 0.99 + np.linspace(+0.005,-0.01,101) #for sweeping tau
↪  linearly
#taulist = 0.98 + 0.015*randtau                 #for randomly varying
↪  tau

spec = np.zeros((len(taulist), len(wlist)))
```

```
i = 0
for tau in taulist:
    # cavity operator
    a  = tensor(destroy(N), qeye(2))

    # operators for the Andreev level
    sm = tensor(qeye(N), sigmam())
    sz = tensor(qeye(N),sigmaz())
    sx = tensor(qeye(N),sigmax())

    # ABS - Resonator Hamiltonian
    H = fc * (a.dag() * a + 1/2) + fandreev(flux,tau)/2 * sz +
    ↪  g(M,fc,Zc,flux, tau) * (a.dag() + a) * (F(flux, tau) * sz +
    ↪  sx)

    # collapse operators
    n_th = 0.1 # finite bath temp in terms of excitation number
    c_ops = [np.sqrt(kappa * (1 + n_th)) * a, np.sqrt(kappa * n_th) *
    ↪  a.dag(), np.sqrt(gamma) * sm]

    # calculate resonator power spectrum using 'spectrum' function
    spec[i,:] = spectrum(H, wlist, c_ops, a.dag(), a)
    i = i+1

#plot the spectrum
swept = np.linspace(0,1,len(taulist))
FreqMesh, ControlMesh = np.meshgrid(wlist, swept);
fig1, ax1 = plt.subplots(2,1, figsize=(6,8))

cs = ax1[0].contourf(ControlMesh,FreqMesh/1e9,1-spec/np.max(spec),50,
↪  cmap='hot');
ax1[0].set_xlabel('Swept Paramter')
ax1[0].set_ylabel('S21 Frequency (GHz)')
ax1[0].set_title('S21 Magnitude @ M = %1.2f pH, $\kappa$ = %1.2f MHz,
↪  $\gamma$ = %1.2f MHz' %(M/1e-12, kappa/1e6, gamma/1e6))
```

```
#plot the andreev frequency
fa = fandreev(flux,taulist)
ax1[1].plot(swept, fa/1e9)
ax1[1].axhline(fc/1e9,linestyle='--', color='C1',label='$f_c$')
ax1[1].text(swept[-2],fc/1e9 + 0.1,'$f_c$')
ax1[1].set_xlabel('Swept Paramter')
ax1[1].set_ylabel('Andreev Transition Frequency (GHz)')
```

Some other scripts for analysis, most require running one of the above simulations first:

visualise g

```
#%% g as function of flux and tau
fc = 6e9     #cavity frequency
Zc = 60      #cavity impedance
M = 30e-12   #mutual inductance

taus = np.linspace(0,0.99,100)
fluxes = np.linspace(0,1, 201)

glist = np.zeros((len(taus),len(fluxes)))
i = 0
for tau in taus:
    glist[i,:] = g(M,fc,Zc,fluxes,tau)
    i+=1

FluxMesh,TauMesh = np.meshgrid(fluxes,taus)
fig,ax = plt.subplots()
cs = ax.contourf(FluxMesh,TauMesh,glist/1e6,50,cmap='inferno')
ax.set_ylabel('$\\tau$')
ax.set_xlabel('$\\Phi/\\Phi_0$')
ax.set_title('g @ M = %1.1f pH, $\omega_c$ = %1.3f GHz, Z$_c$ = %i
↪  $\Omega$' %(M/1e-12,fc/1e9,Zc))
cbar = fig.colorbar(cs)
cbar.set_label('g (MHz)')
```

extract f_R, $S21_R$, Q from model spectrum

```
#%% Extract S21_R, f_R, Q (via linewidth) using lorentzian fit
from scipy.optimize import leastsq

def lorentz(p,x):
    return p[0]/(1 + ((x - p[1])/(0.5*p[2]))**2)

def errorfunc(p,x,y):
    return lorentz(p,x)-y

x = wlist
swept = np.linspace(0,1,len(fa)) #generic swept variable in place of
↪  flux or tau

params = np.zeros([len(swept),3])
for i in range(len(swept)):
    y = spec[i,:]/np.max(spec)
    p0=[1,6.163e9,1e6] #amplitude,frequency,linewidth initial params
    params[i,:],cov_x,infodict,mesg,ier =
    ↪  leastsq(errorfunc,p0,args=(x,y),full_output=True)

f_R = params[:,1] #resonance frequency
Qi = abs(params[:,1]/params[:,2]) #internal Q-factor
Q = 1/(1/Qi + 1/20000) #total Q, if Qe is known
S21_R = params[:,0] #amplitude at resonance

fig2,ax2 = plt.subplots(4,1,figsize=[6,10],constrained_layout=True)

ax2[0].contourf(ControlMesh,FreqMesh/1e9,1-spec/np.max(spec),50,cmap=
↪  'hot');
ax2[0].set_xlabel('Swept Paramter')
ax2[0].set_ylabel('S21 Frequency (GHz)')
ax2[0].set_title('S21 Magnitude vs $\\tau$ \n M = %i pH, $\kappa$ =
↪  %1.2f MHz, $\gamma$ = %i MHz, $\\tau$ = %1.4f' %(M/1e-12,
↪  kappa/1e6, gamma/1e6, tau))
```

```
ax2[1].get_yaxis().get_major_formatter().set_useOffset(False)
ax2[1].plot(swept,f_R/1e9)
ax2[1].set_title('Resonance Frequency')
ax2[1].set_xlabel('Swept Paramter')
ax2[1].set_ylabel('f$_R$ (GHz)')

ax2[2].plot(swept,Qi)
ax2[2].set_title('Q-factor')
ax2[2].set_xlabel('Swept Paramter')
ax2[2].set_ylabel('Q-factor')

ax2[3].plot(swept,1-S21_R/max(S21_R))
ax2[3].set_title('Amplitude at Resonance')
ax2[3].set_xlabel('Swept Paramter')
ax2[3].set_ylabel('S21$_R$ (a.u.)')
```

import data and plot with model

```
#%%import data (previously processed in Matlab to extract f_R_data
↪  and Q_data)
num = str(682)
pre = 'C:\\Users\\Vivek\\Google Drive\\PhD\\Analysis\\Andreev
↪  Qubit\\Imported Data\\MG2A-AQH8a\\'
S21_data=np.loadtxt(pre + num + '\\' + num + '_S21.dat')
Frequency_data=np.loadtxt(pre + num + '\\' + num + '_freq.dat')
Gate_data=np.loadtxt(pre + num + '\\' + num + '_gate.dat')
f_R_data = np.loadtxt(pre + num + '\\' + num + '_Qf_res.dat')
#Q_data = np.loadtxt(pre + num + '\\' + num + '_Qi.dat')

#%% plot spectrum of data and model
fig3,ax3 = plt.subplots(2,1,figsize = (6,8))
ax3[0].contourf(ControlMesh,FreqMesh/1e9,1-spec/np.max(spec),50,cmap=
↪  'hot');
ax3[0].set_xlabel('Swept Parameter')
ax3[0].set_ylabel('S21 Frequency (GHz)')

FreqMeshData, ControlMeshData = np.meshgrid(Frequency_data,
↪  Gate_data);
```

```
ax3[1].contourf(ControlMeshData,FreqMeshData,S21_data.T,50,cmap='hot'
↪  );
ax3[1].set_xlabel('QPC Gate (V)')
ax3[1].set_ylabel('S21 Frequency (GHz)')
ax3[1].set_ylim(min(wlist/1e9),max(wlist/1e9))

#%%plot frequency shifts from JCM, model and data together
#calculate JCM dispersive shift = g^2/detuning
g_plot = g(M,fc,Zc,flux,taulist) #swap flux/fluxlist and tau/taulist
↪  as appropriate
fa_plot = fandreev(flux,taulist)
xi = g_plot**2/(fa_plot - fc)

fig4, ax4 = plt.subplots(figsize=[6,6])
ax4.plot(swept,-xi/1e6,':',label='$g^2/\delta$')
ax4.plot(swept, -(fc - f_R)/1e6, '--', label = 'model')
ax4.plot(np.linspace(0,1,len(Gate_data)), -(fc/1e6 - f_R_data/1e-3),
↪  '.', label='data');

ax4.set_title('Frequency Shift\n M = %i pH, $\kappa$ = %1.2f MHz,
↪  $\gamma$ = %i MHz, $\\tau_{max}$ = %1.3f' %(M/1e-12, kappa/1e6,
↪  gamma/1e6, max(taulist)))
ax4.set_xlabel('Swept Paramter')
ax4.set_ylabel('$\Delta$f$_R$ (MHz)')
ax4.legend()
ax4.set_ylim(-0.5,0.5)
```